COMPREHENSIVE MODELING OF SURGE AND SWAB PRESSURES IN ECCENTRIC ANNULI: A MATHEMATICAL AND COMPUTATIONAL APPROACH

A THESIS SUBMITTED TO
THE GRADUATE SCHOOL OF NATURAL AND APPLIED SCIENCES
OF
MIDDLE EAST TECHNICAL UNIVERSITY

BY

ÖNER ERGE

IN PARTIAL FULFILLMENT OF THE REQUIREMENTS
FOR
THE DEGREE OF DOCTOR OF PHILOSOPHY
IN
PETROLEUM AND NATURAL GAS ENGINEERING

SEPTEMBER 2023

Approval of the thesis:

COMPREHENSIVE MODELING OF SURGE AND SWAB PRESSURES IN ECCENTRIC ANNULI: A MATHEMATICAL AND COMPUTATIONAL APPROACH

submitted by **ÖNER ERGE** in partial fulfillment of the requirements for the degree of **Doctor of Philosophy** i**n Petroleum and Natural Gas Engineering, Middle East Technical University** by,

Prof. Dr. Halil Kalıpçılar
Dean, Graduate School of **Natural and Applied Sciences** _____

Asst. Prof. Dr. İsmail Durgut
Head of the Department, **Petroleum and Natural Gas Engineering** _____

Prof. Dr. Serhat Akın
Supervisor, **Petroleum and Natural Gas Engineering, METU** _____

Examining Committee Members:

Assoc. Prof. Dr. Çağlar Sınayuç
Petroleum and Natural Gas Engineering, METU _____

Prof. Dr. Serhat Akın
Petroleum and Natural Gas Engineering, METU _____

Asst. Prof. Dr. İsmail Durgut
Petroleum and Natural Gas Engineering, METU _____

Prof. Dr. Gürşat Altun
Petroleum and Natural Gas Engineering, ITU _____

Prof. Dr. Mehmet Sorgun
Civil Engineering, IKCU _____

Date: 06.09.2023

I hereby declare that all information in this document has been obtained and presented in accordance with academic rules and ethical conduct. I also declare that, as required by these rules and conduct, I have fully cited and referenced all material and results that are not original to this work.

Name Last name : Öner Erge

Signature :

ABSTRACT

COMPREHENSIVE MODELING OF SURGE AND SWAB PRESSURES IN ECCENTRIC ANNULI: A MATHEMATICAL AND COMPUTATIONAL APPROACH

Erge, Öner
Doctor of Philosophy, Petroleum and Natural Gas Engineering
Supervisor: Prof. Dr. Serhat Akın

September 2023, 151 pages

Estimating swab and surge pressures accurately is critical in the drilling industry, particularly in narrow pore and fracture pressure margins. This study presents an improved numerical model for predicting surge and swab pressures in eccentric annuli, incorporating yield pseudoplastic fluids and temperature effects on rheological parameters. The model utilizes a finite difference scheme and a modified eccentric annulus representation, composed of an infinite number of concentric annuli with varying outer radii. Computational fluid dynamics (CFD) analysis is performed to validate the numerical model, which is further verified using experiments, and literature models with differences in the range of 1-15% are found.

Two surrogate models, Artificial Neural Network (ANN) and Random Forest (RF), are developed based on the proposed numerical model to provide accurate and computationally efficient alternatives for real-time applications. The study outlines the derivation and validation of the numerical model, followed by the development and evaluation of the ANN and RF surrogate models. Overall, the proposed approach offers an improved method for predicting swab and surge pressures in eccentric annuli, contributing to safer and more efficient drilling operations.

Keywords: Surge and Swab Pressures, Numerical Modeling, Surrogate Modeling, CFD, Eccentric Annulus

ÖZ

EKSANTRİK ANÜLÜSTE SURGE VE SWAB BASINÇLARININ KAPSAMLI MODELLEMESİ: MATEMATİKSEL VE BİLİŞİMSEL BİR YAKLAŞIM

Erge, Öner
Doktora, Petrol ve Doğal Gaz Mühendisliği
Tez Yöneticisi: Prof. Dr. Serhat Akın

Eylül 2023, 151 sayfa

Sondaj endüstrisinde, özellikle dar gözenek ve çatlatma basınç marjları içeren kuyularda, surge ve swab basınçlarını doğru bir şekilde tahmin etmek kritik öneme sahiptir. Bu çalışma, sıcaklığın reolojik parametreler üzerindeki etkilerini dikkate alarak yield power law akışkanların eksantrik (eş merkezli olmayan) anülüslerde surge ve swab basınçlarını hesaplamak için geliştirilmiş bir sayısal model sunmaktadır. Model, sonlu farklar yöntemi kullanarak dış yarıçapları değişen sonsuz sayıda konsantrik borulardan oluşan modifiye bir eksantrik boru temsili kullanmaktadır. Sayısal modeli doğrulamak için hesaplamalı akışkanlar dinamiği (CFD) analizi, deneyler ve literatürdeki kabul görmüş diğer modeller kullanılmıştır ve 1-15% aralığında farklar bulunmuştur.

Sunulan sayısal modele gerçek zamanlı uygulamalar için doğru ve verimli alternatifler sağlayan iki vekil model, Yapay Sinir Ağı (ANN) ve Rastgele Orman (RF) uygulamaları kullanılarak geliştirilmiştir. Çalışma, sayısal modelin türetilmesi ve doğrulanmasını, ardından ANN ve RF vekil modellerinin geliştirilmesi ve değerlendirilmesini içermektedir. Önerilen yaklaşım, eksantrik anülüslerdeki surge

ve swab basınçlarını tahmin etmek için daha gelişmiş bir yöntem sunarak, daha güvenli ve daha verimli sondaj operasyonlarına katkıda bulunması hedeflenmiştir.

Anahtar Kelimeler: Surge ve Swab Basınçları, Sayısal Modelleme, Vekil Modelleme, CFD, Eksantrik Anülüs

to my beloved family

ACKNOWLEDGMENTS

I would like to express my deepest gratitude to my supervisor Prof. Dr. Serhat Akın for his encourage, patience, support and mentorship throughout this journey. His expertise, encouragement and dedication have been instrumental in shaping the direction and quality of this thesis. Without his guidance and valuable advices, this work would be incomplete.

I am deeply thankful to my family Nursel Erge, Selin Güven Erge, Öney Erge and to the newest member, my love Nil Erge for their love, understanding, and constant encouragement. Their unwavering belief in me has been a constant source of strength and motivation. I feel lucky to have them by my side.

I would also like to extend my heartfelt thanks to my close friends and colleagues, Ahmet Sönmez and Kudret Sakaoğlu, for their support, insightful discussions and encouragement during the ups and downs of this endeavor. Their friendship and vision have made this journey even more fulfilling.

This thesis is dedicated to my family.

TABLE OF CONTENTS

LIST OF TABLES

TABLES

LIST OF FIGURES

FIGURES

LIST OF ABBREVIATIONS

ABBREVIATIONS

AAPE	Absolute Average Percent Error
ANN	Artificial Neural Networks
API	American Petroleum Institute
BHT	Bottom Hole Temperature
CFD	Computational Fluid Dynamics
ECD	Equivalent Circulating Density
HB	Herschel Bulkley
HPHT	High Pressure High Temperature
MAE	Median Absolute Error
MSE	Mean Square Error
NPT	Non Productive Time
PG	Pressure Gradient
RF	Random Forest
RMSE	Root Mean Square Error
RP	Recommended Practice
RPM	Rotation Per Minute
YPL	Yield Power Law

LIST OF SYMBOLS

SYMBOLS WITH UNITS

dp/dl	Pressure Gradient	Pa / m
v_p	Pipe Velocity	m / s
v_z	Velocity in z- Direction	m / s
K	Consistency Index	Pa . s
n	Flow Behavior Index	
r_i	Inner Radius	m
r_o	Outer Radius	m
R_N	Dial Reading at N RPM	^{o}
τ_y	Yield Stress	Pa
μ_p	Plastic Viscosity	Pa
ε	Dimensionless Eccentricity	
τ	Shear Stress	Pa
μ	Viscosity	Pa.s
γ	Shear Rate	s^{-1}

CHAPTER 1

INTRODUCTION

Drilling operations, particularly in deepwater and high-pressure high-temperature (HPHT) environments, often face unique challenges, such as working within narrow operating pressure windows. In these situations, maintaining the equivalent circulating density (ECD) within safe limits is critical to prevent fluid loss, formation damage, or dangerous influxes. Accurate estimation of swab and surge pressures during well construction is essential to ensuring operational safety and efficiency. However, many existing swab and surge models rely on the assumption of a concentric annulus, which does not always accurately represent actual well conditions.

In reality, most wells deviate from vertical, these drilling deviations occur due to factors such as rotational tendencies, inclination, and horizontal drilling, leading to eccentric annular geometries, where the annular space between the drill pipe and the wellbore wall is unevenly distributed. As the drillstring deviates from the center, the wellbore geometry becomes partially or fully eccentric, significantly impacting the fluid flow and pressure losses within the annulus. Accurately accounting for the effects of eccentricity in swab and surge models is essential for optimizing drilling operations and minimizing the risks associated with these deviations.

On the other hand, temperature changes within the wellbore can significantly impact the rheology of drilling fluids and, consequently, pressure losses. As the temperature at the bottom hole differs from the surface temperature, fluid parameters in the Yield Power Law (YPL) model can change, resulting in increased or decreased pressure losses. Incorporating the effects of temperature in surge and swab models is crucial for predicting pressure changes during pipe reciprocation, tripping, and drillstring

movement, which can lead to formation fracturing, loss circulation, or even well control situations if not properly managed.

This study presents an improved mathematical model for analyzing swab and surge pressures in eccentric annuli, incorporating the effects of temperature on yield pseudoplastic fluids. A finite difference numerical scheme proposed for reciprocating tubulars in concentric annulus. The concept of eccentric annulus treated as being composed of an infinite number of concentric annuli with varying outer radii is applied, allowing for the accurate representation of the complex annular geometries that occur in real drilling situations. This geometric transformation has never been utilized for neither YPL fluids, nor surge and swab pressure analysis before.

To validate the proposed model, computational fluid dynamics (CFD) analysis is performed, and the results are compared to experimental results, and models from the literature. In addition, Artificial Neural Network (ANN) and Random Forest (RF) machine learning techniques are used to develop a surrogate model that can provide accurate and computationally efficient predictions of surge and swab pressures in real-time. This approach allows for the development of both numerical and surrogate modeling solutions that can be used in real-time optimization schemes and drilling operations.

The introduction of this comprehensive modeling approach, numerical and surrogate models address the need for an accurate, efficient, and easily implementable solution to predict swab and surge pressures in eccentric annuli. By incorporating the effects of temperature and eccentric annular geometry, the model allows for improved operational safety and optimization of drilling processes, ultimately reducing the risks associated with drilling operations. This study is expected to contribute significantly to the field of drilling engineering by providing a comprehensive, well-validated model that can be used as a practical tool for drillers and engineers in the field.

CHAPTER 2

LITERATURE REVIEW

Most of the earlier studies that present surge and swab models account for concentric annulus. Drillpipe being concentric in the hole is hardly the case especially in deviated and horizontal wells as pipe tend to move downside of the wellbore due to gravitational force. Pipe being eccentric reduces pressure losses due to axial movement of inner pipe and to an extend that should not be overlooked. More recent studies implement flow in eccentric annulus for various Non-Newtonian fluid models with some assumptions and limitations.

The research on surge and swab pressures went back almost a century ago. The early milestone researches in this field of petroleum engineering were conducted by Cannon (1934), Cardwell (1953), Burkhardt (1961), Schuh (1964), Fontenot & Clark (1974), and Lubinski et al. (1977). These studies explored the nature, origin, and magnitude of surge and swab pressures, and developed mathematical models incorporating rheological models of drilling fluids and different annular geometries to calculate tripping speed and pressure drop during axial movement of the drill string.

Cannon (1934) was the first to publish a paper to address swabbing phenomena. They have installed a sub-surface pressure gauge and recorded the measurements to observe the pressure reduction while tripping out. The author did measurements with different conditions and presented the direct relationship among varying drilling fluids viscosity and gel strength, tripping speed and annular clearance with resulting swab pressure.

Cardwell (1953) investigated the nature of surge and swab pressures with their extent, taking into account the influences of viscosity and wellbore geometry. He clarified a common misunderstanding of nature of swab pressure is due to so-called

balled-up bit and bottom hole assembly; stating that pressure reductions occur even with clean bits. His study was the first to include quantitative theory for surge and swab pressure of Newtonian flow during laminar flow.

Burkhardt (1961) published a research paper explaining the theoretical principles and fundamental aspects of surge and swab phenomena. The study highlighted that the annular velocity relies on the rheological model of the drilling fluid, which can be either Bingham Plastic or Newtonian, as well as on factors such as annular geometry, flow type (laminar or turbulent), and tripping speed. He presented easy-to-use field equations to calculate tripping speed and pressure drop due to axial movement of drillstring for Bingham Plastic fluids for laminar and turbulent regime. The author made an analysis of parameters for both closed-end and open-end pipes to point the difference on how they affect the viscous drag related surge pressures.

Schuh (1964) presented an approximate numerical model for surge and swab pressures for Power Law fluids. His study accounted for concentric annuli and for both laminar and turbulent flow. He utilized a computer program to get the output of bottom hole pressure generated by surge, with inputs of plastic viscosity, yield point, gel strength of drilling fluids, wellbore geometry and pipe velocity. His study was groundbreaking in terms of numerical modeling and making use of computers at his time; which was easy to use in field applications.

Fontenot & Clark (1974) adopted an approach similar to Burkhardt (1961) and Schuh (1964) and proposed a new model to calculate bottom hole pressure during surge and swab. They addressed the shortcomings of models proposed by Burkhardt (1961) and Schuh (1964), corrected some mistakes in their equations and consequently developed a model and implemented into a computer program. Their model include Power Law and Bingham Plastic fluid models. The program results were in accord with field measurements.

Another pioneer study in this field was conducted by Lubinski et al. (1977). They were the pioneers in introducing pressure surge calculations based on the principles of transient wave propagation, developing a comprehensive and fully dynamic

unsteady-state model for surge and swab pressures. Their model encompassed the transient motion of the drillstring and accurately accounted for the swab/surge pressure that arises from the reciprocation of the drillstring.

Lal (1983) proposed a dynamic surge and swab model for Power Law fluids considering the unsteady flow caused by the pressure transients due to acoustic speed of drilling fluid. He corrected a few deficits of the dynamic model developed by Lubinski et al. (1977). The author implemented his model into a computer program. The software calculates maximum surge pressure within time variation, and also maximum safe tripping speed considering the maximum safe pressure margin. The input parameters consist of tripping depth, wellbore geometry, mud properties, and pipe speed. The author conducted a sensitivity for various wells in order to show the effects of various parameters on pressure variations. He also compared his proposed dynamic model results with the steady-state model results taken from Burkhardt (1961).

Mitchell (1988) developed a dynamic surge model accounts for laminar flow of Power Law fluid for concentric annuli. The novelty of his model was due to inclusion of temperature and pressure dependent fluid properties (i.e plastic viscosity and yield point) and compressibility of the drilling fluid. His model also considers the elasticity of pipe, formation and cement; such that longitudinal elasticity and viscous forces determine the displaced volume. He pointed out the effect of fluid compressibility on surge pressure gets more noticeable in deep wells. He made a comparative analysis with the proposed model with the field data acquired form Burkhardt (1961), and Fontenot & Clark (1974).

Samuel et al. (2003) presented field data collected from two different wells. They have recorded the downhole pressure variations in five different cases while surge and swab takes place, with pumps on and off, with rotation on and off. Their data set include different drilling fluids running in different annular geometry and tripping speeds from two different wells. Authors compared the results with the transient model developed by Mitchell (1988), which accounts for effects of fluid inertia and

compressibility, wellbore and pipe elasticity and temperature dependent fluid properties. Authors show a good relationship between predicted and measured pressures while reciprocating the pipe.

Krishna et al. (2020) conducted a more recent study focusing on the surge and swab pressures of Yield Power Law (YPL) fluids in concentric annulus. In their research, the authors introduced an analytical solution that incorporates the mud clinging constant into their model. This predictive model combines frictional pressure loss and the mud clinging effect to accurately forecast pressure surge resulting from Couette fluid flow phenomena in the wellbore. The validity of the authors' model was confirmed by comparing it with two existing analytical models and experimental data from published literature. Furthermore, a parametric analysis was performed to investigate the influence of various parameters on the pressure differential resulted by axial movement of inner pipe.

Studies on surge and swab analysis in eccentric annulus is more limited when compared to concentric ones, due to its non-axisymmetric geometry and complexity in solution. Yet, the research began in 1950s with pioneer studies from Tao and Donovan (1955), Heyda (1959), and Vaughn (1965). These studies formed the foundation of the future work in the topic of fluid flow in non-concentric annulus for Newtonian and Non-Newtonian fluids.

Milestone studies on fluid flow in eccentric annulus specific to oil industry were conducted and reported by Iyoho and Azar (1981), Uner et al. (1989), Carrasco-Teja and Frigaard (2010), Haciislamoglu and Langlinais (1990) and Luo and Peden (1990).

Iyoho and Azar (1981) introduced the narrow-slot concept to analytically solve the non-Newtonian fluid flow through eccentric annuli. Normally, analytical integration of non-Newtonian fluid flow is not possible due to nonlinearity of YPL fluid model definition; therefore, such flow has to be modeled using numerical methods; i.e, finite element method (FEM), finite difference method (FDM), boundary element (BEM) or discrete element method (DEM). The researchers developed the applicable

differential equations using the Ostwald de Waele Power Law Model and a non-rectangular slot; so that they could obtain a realistic analysis of local velocity distribution and eventually better prediction of cuttings behavior in an eccentric annulus. Their narrow-slot approach was, then, used by many researchers in the industry to solve non-Newtonian fluid flow in annulus by analytical equations.

Uner et al. (1989) used the narrow slot approximation to represent the annular geometry as a slit of variable height and solved for the volumetric flow rate for eccentric annulus for a certain pressure drop when comparing with a concentric annulus. The authors emphasized that, compared to a concentric annulus, the volumetric flow rate increases significantly when the inner pipe is deflected from the center for the same pressure drop. The increase can be as much as 240%, depending on the values of eccentricity and diameter ratio. They used the same model, narrow slot model, with modified volumetric flow rate equations depicted in Iyoho and Azar (1981). The paper presents a comprehensive analysis of the effects of various parameters, including fluid rheology, eccentricity ratio, and flow rate, on the velocity and pressure fields in the annulus. The results of their analysis demonstrate a high level of agreement with exact values for diameter ratios larger than 0.3.

Carrasco-Teja and Frigaard (2010) investigated the behavior of non-Newtonian fluids in horizontal narrow eccentric annuli, specifically focusing on the effects of the reciprocation of the inner cylinder. Their study aims to provide insights into the displacement process of drilling fluids in complex wellbore geometries while cementing. The authors conducted experimental investigations and comprehensive mathematical model to simulate the flow of non-Newtonian fluids in eccentric annuli. They used a power-law fluid model to represent the rheological behavior of the drilling fluids. The experiments involved varying the eccentricity, the flow rate, and the inner cylinder speed to observe their influence on the flow behavior Their study provides valuable insights into the flow characteristics of non-Newtonian fluids in eccentric annuli, specifically highlighting the effects of the slow motion of the inner cylinder. The findings of their work contribute to a better understanding of

fluid displacements in complex wellbore geometries, which can be beneficial for optimizing drilling operations.

Haciislamoglu and Langlinais (1990) solved the flow of non-Newtonian fluids in eccentric annulus numerically using finite difference technique. Developed model takes into account Yield-Power Law, Bingham Plastic and Power Law models as well as Newtonian fluids. They have obtained the velocity and viscosity profiles in concentric and non-concentric annuli, with varying eccentricities. Authors showed that the alteration of velocity profile in eccentric annulus is substantial and resulting pressure loss changes should not be underestimated. They have provided a correlation to calculate frictional pressure drops for Power Law fluids in eccentric annuli which was simple enough for field use.

Luo and Peden (1990) developed a new method to analyze the laminar flow of non-Newtonian fluids in an eccentric annulus. The method involves representing the eccentric annulus as an infinite number of concentric annuli with varying outer radii. They have originally used the solution of annular flow in concentric annulus, and then construct a geometric transformation to approximate into eccentric annulus. Readers can find more on this concept in the next chapter of this study. Analytical solutions are derived for different flow parameters, including shear stress, shear rate, velocity, and volumetric flow rate/pressure gradient, applicable to both Power Law and Bingham Plastic fluids. The authors found that their method provides more precise approximations for different profiles and accurately predicts the volumetric flow rate/pressure gradient in eccentric annular flow and involves more simple calculation steps.

Research in the literature on surge and swab pressure extends to more studies, such as the models and experiments used in the comparative study presented in Chapter 7 of this thesis. He et al. (2016) and Crespo and Ahmed (2013) presented their model and experimental research regarding surge and swab pressures in concentric annulus, while Tang et al. (2016) and Belimane et al. (2021) presented experimental data and model results for surge and swab pressures in eccentric annulus. Details of their work

are thoroughly described in Chapter 7 before presenting results of each validation. Moreover, a summary table showing details of these authors' works are presented in Table 7.1 for readers' convenience.

Definition and theory of Newtonian and Non-Newtonian fluids' flow behavior and shear stress equations for common fluid models will be given in this chapter to provide a background for the next chapters.

2.1 Rheology Behavior of Newtonian Fluids

Newtonian fluids demonstrate a linear relationship between the applied shear rate and shear stress. This proportionality allows for the definition of apparent viscosity, which represents the ratio of shear stress to shear rate. In the case of Newtonian fluids, the apparent viscosity remains constant and is commonly referred to as dynamic viscosity.

In the context of Newtonian fluids, the behavior can be described as having a constant viscosity regardless of the shear rate applied. This characteristic simplifies the relationship between shear stress and shear rate, allowing for a direct proportionality between the two. The apparent viscosity, also known as dynamic viscosity, remains unchanged throughout the flow, resulting in a linear shear stress equation that accurately represents the behavior of Newtonian fluid as shown in Eq. 2-1.

$$\tau = \mu\gamma \tag{2-1}$$

2.2 Rheology Behavior of Non-Newtonian Fluids

Non-Newtonian fluids exhibit a wide range of flow behaviors, and various models are used to describe their viscosity and shear stress relationships. These fluids often

display viscosity that varies with the applied shear rate or shear stress. A practical graph is displayed in Figure 2.1, which shows the shear stress behavior of different fluid models with varying shear rates.

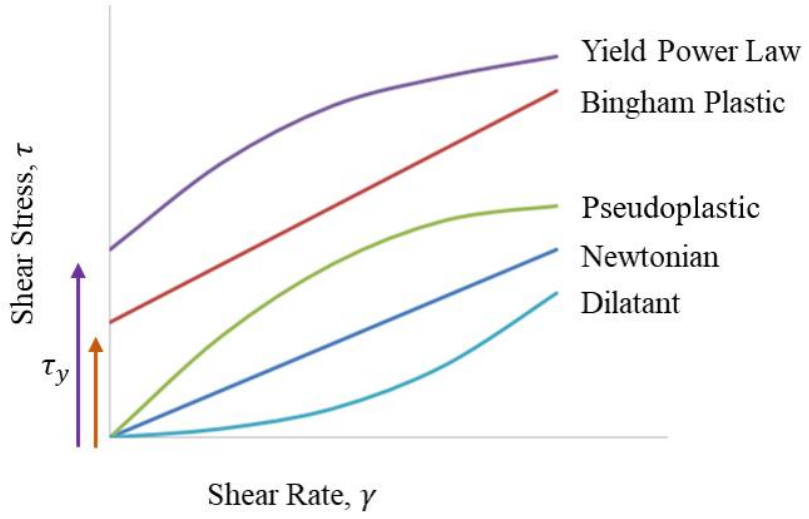

Figure 2.1 Rheology Behavior of Common Fluid Models

One commonly used model is the Power Law model, which relates shear stress to shear rate through a power-law equation. The Power Law model assumes that the viscosity of the fluid varies with the applied shear rate raised to a certain power. This model is particularly useful in describing fluids with shear thinning behavior, where the exponent determines the extent of viscosity change. Many polymer solutions and suspensions can be well-characterized using the Power Law model.

Power Law model equation is shown in Eq. 2-2.

$$\tau = K\gamma^n \tag{2-2}$$

Where; K represents the consistency index, and n is flow behavior index. The non-Newtonian behavior of a fluid is determined by the deviation of the flow behavior index from unity. In the Power Law model, when the value of the flow behavior index, denoted as "n," is less than 1, it indicates the fluid's shear thinning ability. On the other hand, when "n" is equal to 1, it signifies a Newtonian fluid with a constant viscosity. Furthermore, if "n" is greater than 1, it suggests the fluid exhibits dilatant behavior, where the viscosity increases with shear rate. The flow behavior index "n" serves as a key parameter for characterizing the rheological properties and non-Newtonian flow behavior of the fluid in the Power Law model.

When it comes to drilling industry, the shear thinning ability of Power Law makes drilling fluids less viscous as the shear rate increases, which is a fair representation of modern fluids, and makes the model advantageous in drilling operations where higher shear rates are encountered. However, one limitation of the Power Law model is the absence of a yield stress. When characterizing most drilling fluids, it is essential to have a yield stress, which represents the minimum force required to initiate the flow. Therefore, while the Power Law model offers shear-thinning ability, the absence of a yield stress makes it less suitable for accurately representing drilling fluids that require both shear-thinning behavior and a minimum force to initiate flow.

In addition to the Power Law model, the Bingham plastic model is frequently employed to describe the flow behavior of non-Newtonian fluids. Bingham plastics have a yield stress, which represents the minimum stress required to initiate the flow. Once the yield stress is surpassed, the fluid behaves in a linear manner with shear stress directly proportional to shear rate, similar to Newtonian fluids. This model is often applied in the study of some mud flows, pastes, and other materials that exhibit an initial resistance to flow.

Bingham Plastic model is defined by (Bingham, 1922):

$$\tau = \tau_y + \mu_p \gamma \qquad (2\text{-}3)$$

Bingham Plastic model necessitates two parameters to describe a flow: τ_y represents the yield point or the force in order to initiate the flow; and μ_p is the plastic viscosity, that signifies the constant of proportionality between shear stress and shear rate. When the threshold force for flow initiation, i.e., $\tau_y = 0$, the model simplifies into the Newtonian model, as demonstrated in Eq. 2-1.

By accurately capturing the yield stress and subsequent linear behavior, the Bingham Plastic model helps us predict the flow characteristics of such fluids. This behavior, however, may lead to inaccurate results in drilling operations, particularly in deep wells. In drilling operations, the pressure loss within the pipe increases significantly as the well depth increases. However, due to the linear nature of the Bingham plastic model, it may overestimate the pressure losses, resulting in excessively high hydraulics calculations. This discrepancy arises from the inability of the model to accurately capture the complex flow behavior and varying rheological properties of drilling fluids at different shear rates encountered in deep wells. Therefore, alternative models to the Bingham plastic model are often required to more accurately predict pressure losses in drilling industry.

Another important non-Newtonian fluid model is the Yield Power Law model, which combines aspects of both Bingham plastic and Power Law models. The Yield Power Law model introduces a yield stress, below which the fluid does not flow, similar to the Bingham plastic model. However, once the yield stress is exceeded, the flow behavior is described by the Power Law equation. This model is suitable for fluids that exhibit both a yield stress and shear-thinning behavior. It is often applied in the analysis of muds, slurries, and certain food products. This combination of characteristics in the Yield Power Law model makes it a valuable tool for accurately describing and predicting the behavior of drilling fluids, enabling improved calculations of pressure losses and more efficient drilling operations.

Yield Power Law model, often referred to as Herschel-Bulkley or yield pseudoplastic model requires three parameters (Herschel and Bulkley, 1926):

$$\tau = \tau_y + K\gamma^n \quad (2\text{-}4)$$

The YPL model encompasses three key parameters: the yield stress parameter, τ_y, similar to Bingham Plastic model, representing the initiation threshold for flow; the consistency index, K, and flow behavior index, n, as in Power Law model. By adjusting these parameters, YPL model can represent Newtonian fluids, Bingham Plastic and Power Law fluids. Specifically, setting $n = 1$, $K = \mu$, and $\tau_y = 0$ renders it a Newtonian fluid. $\tau_y = 0$ indicates a Power Law fluid; and $K = \mu_p$, and $n = 1$ characterize a Bingham Plastic fluid.

Understanding the flow behavior of non-Newtonian fluids and employing appropriate models, such as the Power Law, Bingham Plastic, and Yield Power Law models, is crucial in various industries and scientific disciplines; including well construction. These models allow for the characterization and prediction of complex fluid behavior, accounting for viscosity changes, yield stress, and shear rate dependence. By utilizing these models, one can effectively analyze and optimize processes involving non-Newtonian fluids, improving the design and efficiency of a wide range of applications, including one of the most important parts of well construction process; rheology and hydraulics analysis of well drilling.

CHAPTER 3

STATEMENT OF THE PROBLEM

3.1 Statement of the Problem

Drilling operations involve pulling or slacking the drillstring, which can cause significant pressure changes at the wellbore. These pressure changes may disturb the desired pressure balance at the bottomhole or other open hole sections, leading to hazardous situations such as kicks or lost circulation. Hence, precise estimation of surge and swab pressures is of utmost importance to optimize tripping operations and maintain a safe operating range within the mud window, ensuring an interval between the pore and fracture pressures. Several existing models estimate swab and surge pressures in concentric annuli, but limited work has been done for eccentric annuli, especially with yield power law (YPL) fluids, which better represent the behavior of modern drilling fluids. Furthermore, the effects of temperature on fluid parameters have not been thoroughly investigated in the existing models, which could result in inaccurate predictions.

Considering the eccentricity of annuli in real drilling scenarios and the effects of temperature on fluid parameters, there is a need for a more comprehensive model that can accurately predict pressure losses and account for these factors. Moreover, complex physics-based models require substantial computational resources and cannot be used as a digital twin for parameter optimization and real-time operations. In such situations, the surrogate models that are usually computationally fast statistical methods that correlate the input and output relationship are more appropriate. However, there is a lack of research on surrogate models for swab and surge pressures in eccentric annuli, particularly those using machine learning techniques.

3.2 Objectives and Approach

The main objectives of this study are to:

1. Develop a mathematical model that predicts swab and surge pressures of YPL fluids in eccentric annuli.
2. Include the effects of temperature on the fluid parameters in the mathematical model to improve the accuracy of pressure predictions.
3. Conduct Computational Fluid Dynamics (CFD) analysis and validate the proposed mathematical model using experimental data and other literature models.
4. Develop surrogate models for swab and surge pressures in eccentric annuli using two machine learning methods, Artificial Neural Network (ANN) and Random Forest (RF) and compare these models with the proposed mathematical model and existing models.

By addressing these objectives, this study aims to provide a reliable and accurate method for predicting swab and surge pressures in eccentric annuli, ultimately contributing to safer and more efficient drilling operations. The development and validation of these models will help engineers in the field optimize drilling parameters in real-time, preventing hazardous situations and improving overall operational efficiency.

CHAPTER 4

MODELING OF SURGE AND SWAB PRESSURES IN ECCENTRIC ANNULI

4.1 Development of Numerical Model

Luo and Peden (1990) developed a method for simulating the flow of Newtonian and non-Newtonian fluids in eccentric annuli by dividing the geometry into multiple concentric annuli with varying outer radii around the inner pipe. This method allows for the capture of the effect of eccentricity while also being easy to implement and computationally efficient. This geometrical approximation is presented in Figure 4.1.

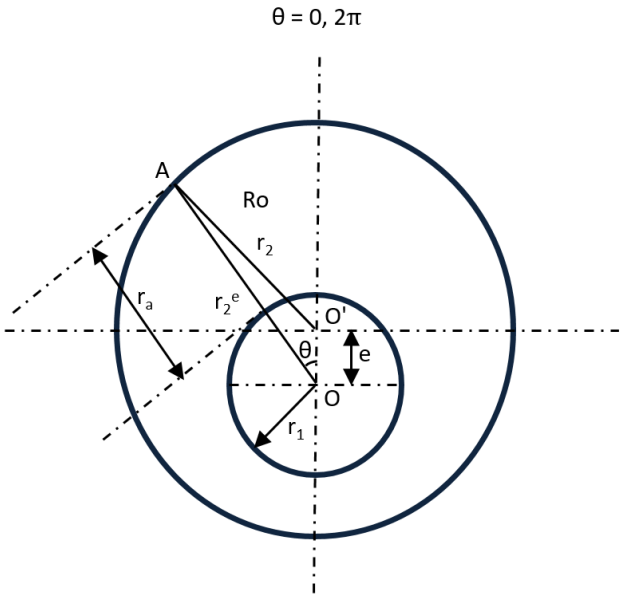

Figure 4.1 Geometric Approximation of Eccentric Annuli

In Figure 4.1, point O and O' are the centers of the inner pipe and outer pipe, respectively, A is an arbitrary point on the outer pipe. An equation is derived by applying the cosine rule to the OAO' triangle. The formula that describes the new

radius of each concentric annulus that makes up the eccentric annulus, as measured from the center of the inner pipe, is given in Eq.4-1 below:

$$r_2^e = ecos(\theta) + \sqrt{r_2^2 - [esin(\theta)]^2} \tag{4-1}$$

Where e is eccentricity, r_1 and r_2 are the radii of the inner and outer pipe, respectively, r_2^e is the radius of the eccentric annulus and r_a is the annular gap that can be estimated as $r_a = r_2^e - r_1$. It can be observed that for $e = 0$, r_2^e and r_2 are equal and the method reduces of a concentric annulus. The characteristic angle, θ enables the division of the eccentric annulus into several concentric annular slices, which can then be combined to form the eccentric annulus. The value of θ can be estimated by:

$$\theta = \frac{2\pi}{N} \tag{4-2}$$

Where N+1 (for the programming languages that the index starts from 1) is the number of concentric annuli with varying r_2^e values that represents the eccentric annulus. In general, a large value of N is desirable to achieve a more accurate approximation of an eccentric annulus. This approximation replaces the r_2 with r_2^e value for each new θ iteration that ranges from 0 to 2π. A new iteration of θ can be estimated by:

$$\theta(\mathrm{i}) = \frac{2\pi}{N}(\mathrm{i} - 1) \tag{4-3}$$

Correspondingly, each radius of the annular slice can be calculated by:

$$r_2^e = ecos\big(\theta(\mathrm{i})\big) + \sqrt{r_2^2 - \big[esin\big(\theta(\mathrm{i})\big)\big]^2} \tag{4-4}$$

Navier-Stokes equations are simplified and numerically solved for the swab and surge pressure in a concentric annulus for Yield Power Law (YPL) fluids as given below (Erge, 2016 & Erge et al., 2018). This numerical solution is more accurate than the slot approximation, which can result in up to 15% error (Erge et al., 2016).

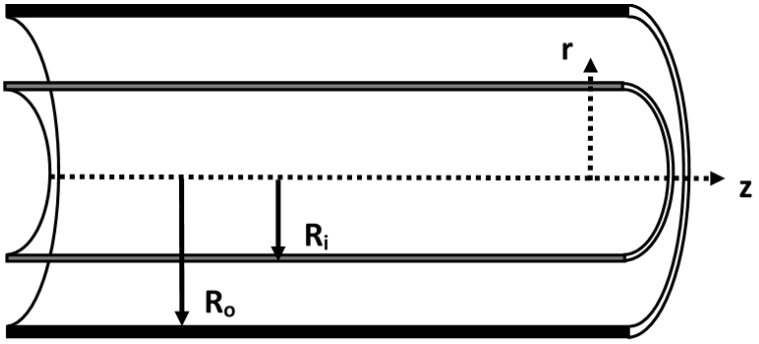

Figure 4.2 Cross-Section of Annulus

The conservation of mass is satisfied through the equation of continuity, which governs the mass balance for a given volume; i.e, difference between mass in and out. Equation of continuity for cylindrical coordinates is given in Eq. 4-5 below (Bird et al., 2007):

$$\left(\frac{\partial \rho}{\partial t}+\frac{1}{r}\frac{\partial(\rho r v_r)}{\partial r}+\frac{1}{r}\frac{\partial(\rho v_\theta)}{\partial \theta}+\frac{\partial(\rho v_z)}{\partial z}\right)=0 \qquad (4\text{-}5)$$

Assumptions such as steady state flow, flow in only axial direction and fully developed flow are made so that mass conservation is satisfied. Also, fluid is assumed to be incompressible and have constant mass density.

The equation of motion in cylindrical coordinates in z- direction is given in Eq. 4-6 below (Bird et al., 2007):

$$\rho\left(\frac{\partial v_z}{\partial t}+v_r\frac{\partial v_z}{\partial r}+\frac{v_\theta}{r}\frac{\partial v_z}{\partial \theta}+v_z\frac{\partial v_z}{\partial z}\right) = -\frac{\partial p}{\partial z}-\left[\frac{1}{r}\frac{\partial}{\partial r}(r\tau_{rz})+\frac{1}{r}\frac{\partial}{\partial \theta}\tau_{\theta z}+\frac{\partial}{\partial z}\tau_{zz}\right]+\quad \rho g_z \tag{4-6}$$

The stress tensors for cylindrical coordinates are substituted and integrated into equation of motion. Considering the annulus in Figure 4.2 and assumptions such as steady state, axisymmetric, fully developed laminar flow in only axial direction with an incompressible fluid and closed ended pipe where there is no slip at the wall, simplified Navier-Stokes equation becomes:

$$\frac{\partial p}{\partial z}=\left[\frac{\partial}{\partial r}\left(\mu\frac{\partial(v_z)}{\partial r}\right)\right]+\left[\frac{1}{r}\mu\frac{\partial(v_z)}{\partial r}\right] \tag{4-7}$$

Discretizing this equation using finite difference numerical method and applying further simplifications would give:

$$\frac{\partial p}{\partial z}2\Delta r^2=\left(\left({\mu_{i+1}}^k+{\mu_i}^k+{\mu_i}^k\frac{\Delta r}{r}\right)({v_{i+1}}^{k+1})-({\mu_{i+1}}^k+2{\mu_i}^k+{\mu_{i-1}}^k)({v_i}^{k+1})+\left({\mu_i}^k+{\mu_{i-1}}^k-{\mu_i}^k\frac{\Delta r}{r}\right)({v_{i-1}}^{k+1})\right) \tag{4-8}$$

Boundary conditions of surge and swab phenomena dictates that $v_z = 0$ at $r = R_o$ and $v_z = v_p$ at $r = R_i$.

Proposed numerical model features dynamic shear stress profile in the flow direction along the annulus. The varying shear rate within the annulus plays a crucial role in understanding the flow behavior of non-Newtonian fluids. Unlike Newtonian fluids, which exhibit a constant viscosity regardless of the shear rate, non-Newtonian fluids experience viscosity changes as the shear rate varies. In eccentric annuli, the fluid moves at different velocities and encounters different flow conditions across the annular gap. As a result, the fluid experiences varying shear rates along different radial locations within the annulus. This variation in shear rate leads to different levels of shearing forces or shear stresses acting on the fluid. Consequently, the fluid's viscosity, referred to as apparent viscosity in this context, also varies spatially due to the sensitivity of the fluid's rheological properties to the applied shear stress.

The impact of varying shear rate on shear stress and viscosity is crucial in accurately predicting the flow behavior of non-Newtonian fluids in eccentric annuli. The variations in shear stress affect the magnitude and distribution of forces within the annular gap. Higher shear rates result in increased shear stress, which can lead to higher frictional pressure losses. Conversely, lower shear rates correspond to reduced shear stress and may result in localized regions of lower frictional resistance. The changes in shear stress and resulting viscosity gradients influence the overall flow patterns, pressure distributions, and surge and swab pressures experienced in the annulus. Therefore, accurately capturing the relationship between varying shear rate, shear stress, and viscosity is essential for obtaining reliable and realistic predictions in yield power law fluid flow analyses in eccentric annuli.

In order to integrate this phenomenon, some supportive equations need to be defined; such as, shear rate, shear stress in YPL model, and it is needed to replace viscosity terms in Eq. 4-8 with μ_{app}, an apparent viscosity. Apparent viscosity should not be confused with a single viscosity term; as it may be denoted to represent a single viscosity term for Newtonian fluids in some of the literature by researchers. In this

context, apparent viscosity is a function of shear rate, i.e, it is changing with respect to changes in the shear rate along the annulus; which is thoroughly explained earlier in this chapter.

$$\gamma = \frac{\partial v_r}{\partial z} \tag{4-9}$$

$$\tau = \tau_0 + K\gamma^n \tag{4-10}$$

$$\mu_{app} = \frac{\tau}{\gamma} \tag{4-11}$$

$$\mu_{app} = \frac{\tau_0}{\gamma} + K\gamma^{n-1} \tag{4-12}$$

This numerical solution is extended to incorporate the effect of eccentricity using Luo and Peden (1990)'s approach. The workflow is presented in Figure 4.3.

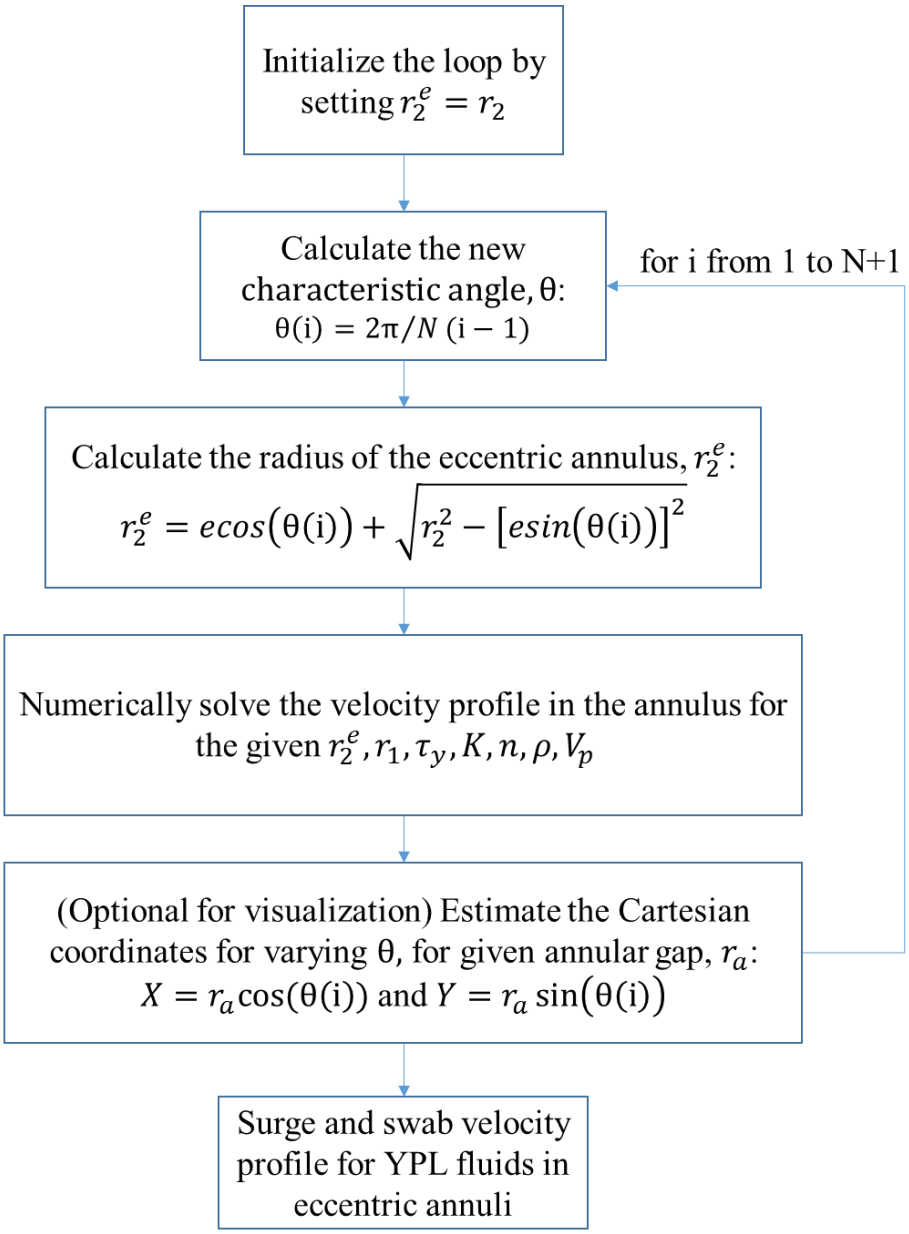

Figure 4.3 Flowchart for the Calculation of Surge and Swab Velocity Profiles for YPL Fluids in Eccentric Annuli

The numerical scheme involves calculating a new velocity profile at each characteristic angle θ(i) that ranges from 0 to 2π. A radius for each θ(i) is calculated and used as an input to solve the velocity profile for a concentric annulus. In this step, equations from Eq.4-7 to Eq.4-12 are used. These concentric annulus velocity

profiles with varying outer radii are then concatenated to construct an eccentric velocity profile. Additionally, the Cartesian coordinates corresponding to each annular slice and the velocity profile that is used in visualizing the 3D swab and surge eccentric annulus velocity profiles can be calculated. Several examples are presented in Figure 4.4.

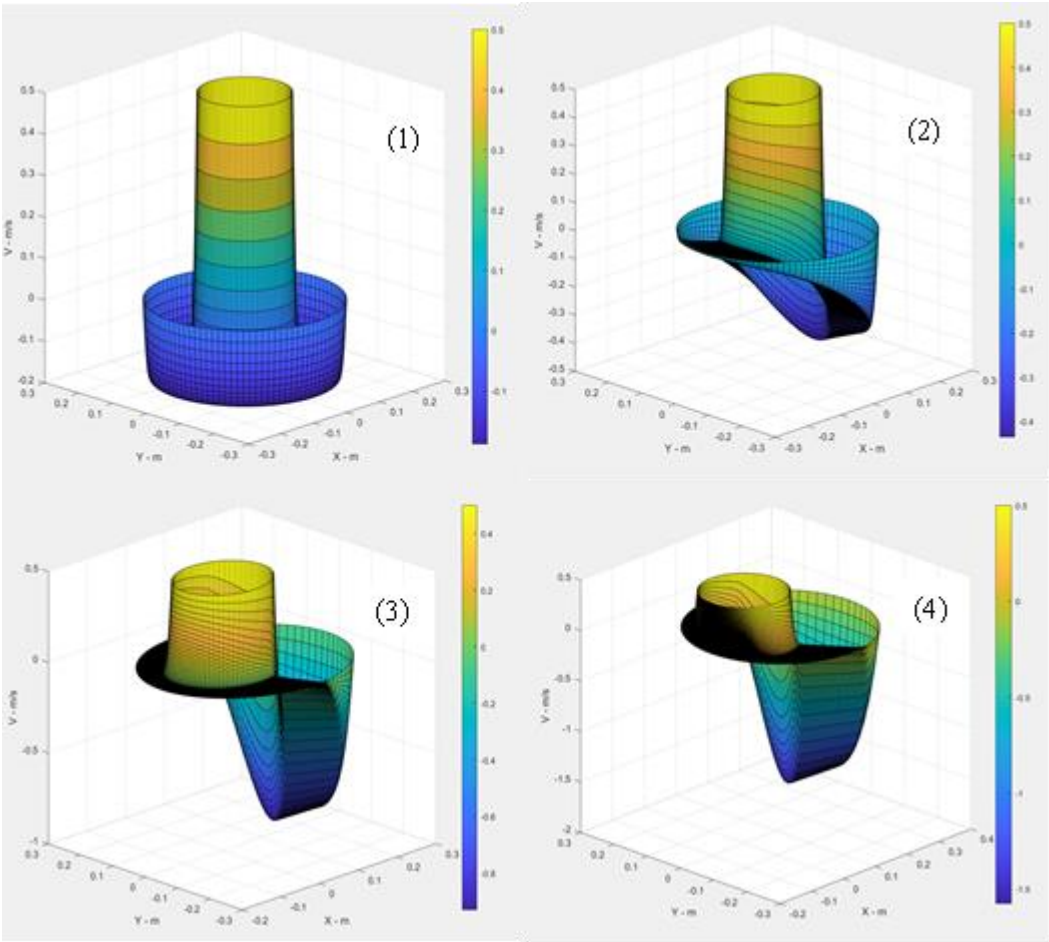

Figure 4.4 Example Velocity Profiles Constructed with the Proposed Method for Varying Degrees of Eccentiricity

Figure 4.4 shows four different velocity profiles while surge occurs with various dimensionless eccentricity values: 0 (concentric), 0.1, 0.5 and 0.99 (fully eccentric).

Subfigures in Figure 4.4 have the following dimensionless eccentricities (ε) and resultant pressure losses (dp/dl). (1): $\varepsilon = 0, dp/dl = 214.5\ Pa/m$; (2): $\varepsilon = 0.1, dp/dl = 211.1\ Pa/m$; (3): $\varepsilon = 0.5, dp/dl = 163.2\ Pa/m$; (4): $\varepsilon = 0.99, dp/dl = 126.4\ Pa/m$. The diameters, fluid properties and pipe velocity are kept the same in all 4 analyses as: $r_2 = 0.2159\ m, r_1 = 0.1016\ m, \tau_y = 8\ Pa, K = 0.3\ Pa \cdot s^n, n = 0.7, \rho = 1000\ kg/m^3, V_p = 0.5\ m/s$.

A dimensionless eccentricity is defined to simplify and enable comparisons:

$$\varepsilon = \frac{e}{r_o - r_i} \tag{4-11}$$

To prevent numerical convergence issues as the inner pipe approaches the other pipe, the fully eccentric annulus is approximately modeled with a dimensionless eccentricity of 0.99. These results demonstrate that increasing eccentricity leads to a decrease in pressure losses. When comparing a concentric and fully eccentric annulus, the increase in eccentricity caused a 40.9% reduction in pressure losses. Additionally, as the eccentricity increases and the inner pipe gets closer to the outer pipe, the velocity in the narrow annular gap decreases significantly, while it increases in the wider gap. These outcomes are consistent with previous research findings (Haciislamoglu and Laglianis, 1990, and Tang et al., 2016).

Another example of surge and swab pressure losses in different eccentricities shown in Figure 4.5 below. Increasing eccentricity from 0.3 to 0.9 yield in a reduction of surge and swab pressures 30% for the given inputs. Figure on the left (L) and on the right (R) have the following dimensionless eccentricities (ε) and resultant pressure losses (dp/dl). (L): $\varepsilon = 0.3, dp/dl = 96.2\ Pa/m$; (R): $\varepsilon = 0.9, dp/dl = 68.5\ Pa/m$. The diameters, fluid properties and pipe velocity are kept the same in both analyses as: $r_2 = 0.197\ m, r_1 = 0.1\ m, \tau_y = 2\ Pa, K = 0.5\ Pa \cdot s^n, n = 0.5, \rho = 1000\ kg/m^3, V_p = 0.5\ m/s$.

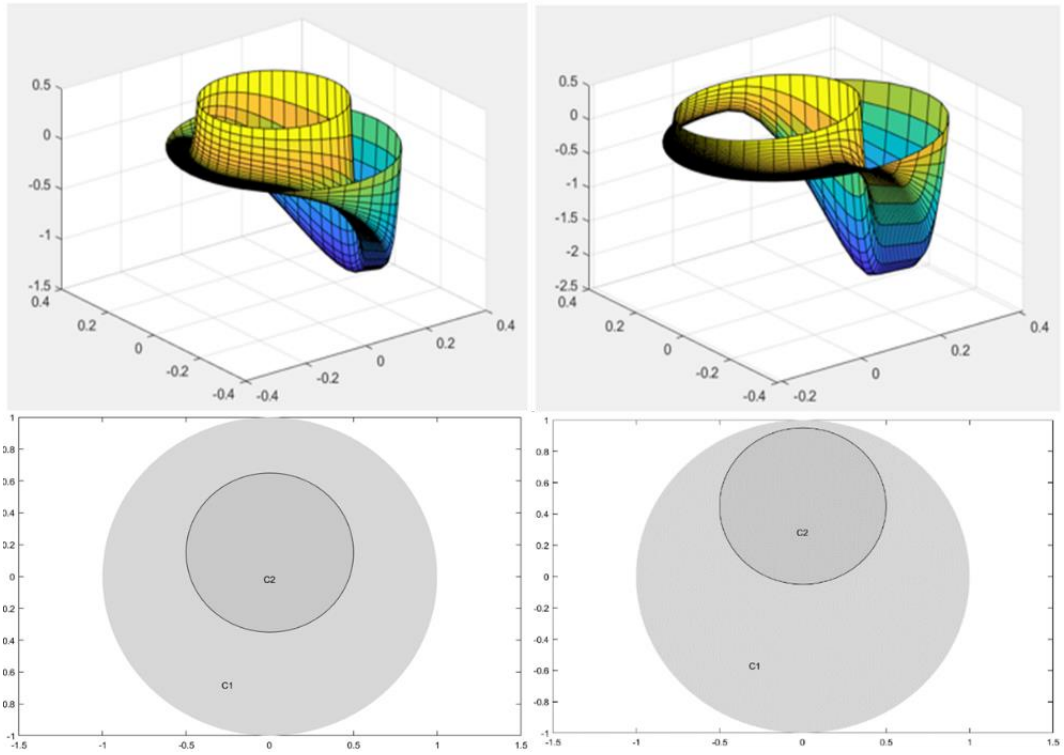

Figure 4.5 Example Velocity Profiles and Top-Views of Annuli Constructed with the Proposed Method for Varying Degrees of Eccentiricity

While it may be a common practice to use mean velocity term in concentric annuli, it would be better to use a profile instead of a single value, since it changes substantially in azimuthal direction due to non-axisymmetrical nature of flow area. For example, the velocity in the narrow section of annulus gets reduced as eccentricity is increased. This is due to the increased resistance to flow in narrow parts. At the same time, fluid flows more through the wide section as illustrated in Figure 4.4 and Figure 4.5.

Higher velocity would result in higher shear rate, which leads to lower viscosity near the walls for both concentric and eccentric annuli. Conversely, lower velocities cause low shear rates and thus higher viscosities in the middle of wide section and in the narrow section of eccentric annulus. Considering the shear thinning nature of YPL fluids; this is an expected behavior. This can be observed from Figure 4.6; where

viscosity profiles for concentric annulus are shown in (1) and in (2); and viscosity profiles for eccentric annulus with $\varepsilon = 0.8$ are shown in (3) and in (4) from top and side views. The viscosity contours are similar to that were presented in Haciislamoglu and Langlinais (1990); and supports the idea of decrease in viscosity due to high shear rate regions in eccentric annuli.

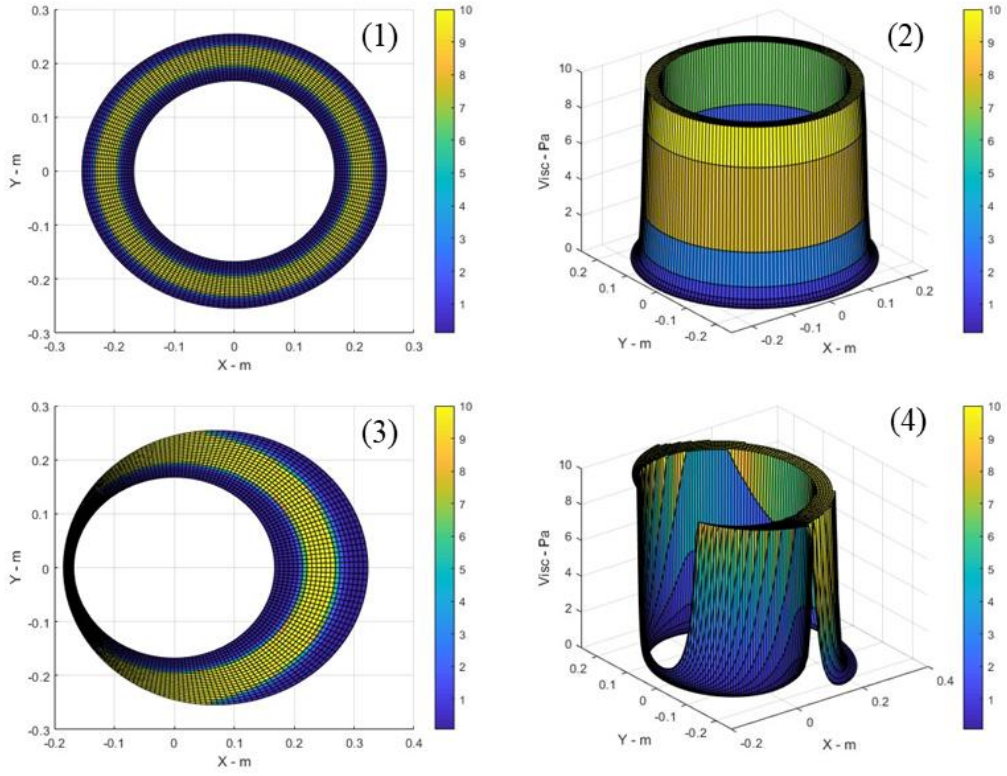

Figure 4.6 Example Viscosity Profiles Constructed with the Proposed Model for Concentric Annulus and Eccentric Annulus

Both velocity and viscosity profiles in eccentric annuli are of critical importance and have huge impact for resulting pressure gradient while reciprocating the inner pipe with YPL fluids. Proposed model is accounting for the dynamic feature of both profiles as detailed theory is given previously in this chapter.

Using the aforementioned information, the velocity profile can be computed based on the specified pressure loss and pipe velocity. To determine the pressure loss for a given pipe velocity, mass conservation and the root finding method via the fzero() function in MATLAB are employed (Forsythe, 1977). The principle of mass conservation states that the volume displaced by the inner pipe's motion must be equal to the volume change in the annulus, assuming constant density. This balance is implemented using the fzero() function, which subtracts the product of the annular cross-sectional area and the mean output velocity from the volume displaced by the inner pipe's motion. The root finding method using the fzero() function is a combination of several methods, such as secant, bisection, and inverse quadratic interpolation, that can be used to find the equilibrium pressure loss value by iteratively altering it.

Complete MATLAB codes are explicitly given in Appendix C, so that other researchers can replicate or build upon this work in their related studies easily.

4.2 Sensitivity Analysis

The parametric study conducted in this thesis aims to investigate the sensitivity of surge and swab pressures in eccentric annuli for yield power law (YPL) fluids to various key parameters. Understanding the influence of different parameters on surge and swab pressures is vital for optimizing drilling practices and enhancing operational safety and efficiency.

In this section, a comprehensive analysis is presented, focusing on the impact of key parameters including YPL fluid parameters; i.e., flow behavior index, yield stress, consistency index, and diameter ratio, pipe velocity, and eccentricity. These parameters are systematically varied, and their effects on surge and swab pressures are evaluated. The objective is to provide valuable insights into the relationships between these parameters and surge and swab pressures, shedding light on the underlying physics and enabling the identification of key factors that significantly

affect pressure profiles. This knowledge can be used to inform drilling engineers and operators in making informed decisions regarding parameter selection, optimizing drilling operations, and preventing & mitigating potential challenges associated with surge and swab pressures while tripping.

Analysis will be conducted in two parts; in the first part input values are shuffled from a database of inputs; i.e., input values change for each analysis and presented similar to a parametric study. In the second part, the variables are selected from a fixed database of inputs; i.e., values of inputs stay the same among all of the analysis unless their effect is being investigated. Figures from Figure 4.7 to Figure 4.12 belong to first part; while figures from Figure 4.13 to Figure 4.17 represent the second part. All of the inputs and outputs of this parametric study are explicitly given in the Appendix A of the thesis; so that other researchers can make comparison more easily.

While selecting the input parameters for this study, several actual field conditions are taken into account. The mainframe for inputs are constructed using 5 different eccentricity values; i.e., from fully concentric, $\varepsilon = 0$, to fully eccentric, $\varepsilon = 0.99$, with increments of 0.25. All of the aforementioned parameters that affects surge and swab pressure were investigated separately in 5 different eccentricity values. By doing so, it is possible to reflect all possible scenarios regarding pipe being offcenter while tripping in actual field conditions.

Diameters used in the sensitivity analysis are selected using actual field conditions; such as 7-in pipe (casing) running in a 8 ½-in hole, or running a 6 ¼-in drill collar into 12 ¼-in hole. Moreover, laboratory scale diameters are also used such as ½-in and 2/3-in pipe into 1-in hole. Tripping speeds are chosen using same criteria. YPL fluid parameters, i.e., yield stress, flow behavior index and consistency index are also picked to reflect actual water based and oil based drilling fluids' rheology. A similar study for input parameters is conducted while constructing the surrogate models, and detailed information is given in Chapter 8 of this thesis.

The results of the first part of sensitivity analysis are presented in Figures between Figure 4.7 to Figure 4.12. Figures correspond to effects of consistency index, yield stress, flow behavior, pipe velocity, yield stress with different geometry and effect of diameter ratio with varying eccentricity values on surge and swab pressures for YPL fluids, respectively. All of the input and outputs are presented in Tables from Table A.1 to Table A.6 in Appendix A.

Figure 4.7 shows the effect of consistency index on surge and swab pressures of YPL fluids with varying eccentricity while running a 6-in pipe into 17 ½-in hole. As it can be interpreted from graph, increasing consistency index also increases the resulting surge and swab pressures. However, as pipe gets more off-center, i.e., with increasing eccentricity, pressure losses decrease significantly. All inputs for this study are listed in Table 4.1 below:

Table 4.1 Input Parameters for Sensitivity Analysis Shown in Figure 4.7

$V_p, m/s$	n	$K, Pa.s^n$	τ_y, Pa	R_o, m	R_i, m	R_i/R_o	ε
1.2	0.3	0.3	9.5	0.22225	0.0762	0.34	0
		0.6					0.25
		0.9					0.50
		1.2					0.75
		1.5					0.99

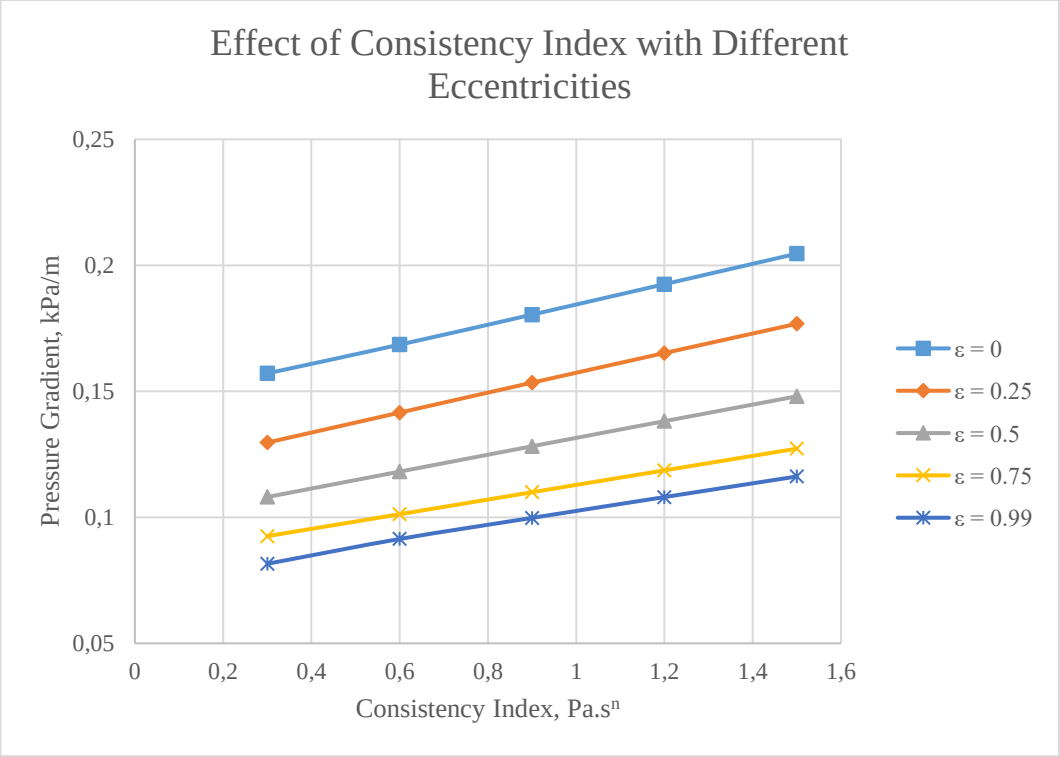

Figure 4.7 Effect of Consistency Index on Surge and Swab Pressures of YPL Fluids with Varying Eccentricities

In Figure 4.8 the effect of yield stress on surge and swab pressures of YPL fluids with varying eccentricity while running a 4 ½-in pipe into 6-in hole is shown. This wellbore geometry, coupled with tripping speeds and other fluid properties are a common example that could be encountered in actual drilling conditions. The graph shows an increase in the surge and swab pressure with increasing yield stress. This is an intuitive result considering the definition of yield stress, the force to initiate flow. On the other hand, it is also expected to observe the inverse proportionality between resulting pressure with eccentricity; a 32% reduction in pressure losses are noted when comparing fully concentric to fully eccentric with this particular inputs. Table 4.2 lists the input parameters for this study.

Table 4.2 Input Parameters for Sensitivity Analysis Shown in Figure 4.8

$V_p, m/s$	n	$K, Pa.s^n$	τ_y, Pa	R_o, m	R_i, m	R_i/R_o	ε
0.6	0.9	1.2	0.5 3.5 6.5 9.5 12.5	0.0762	0.05715	0.75	0 0.25 0.50 0.75 0.99

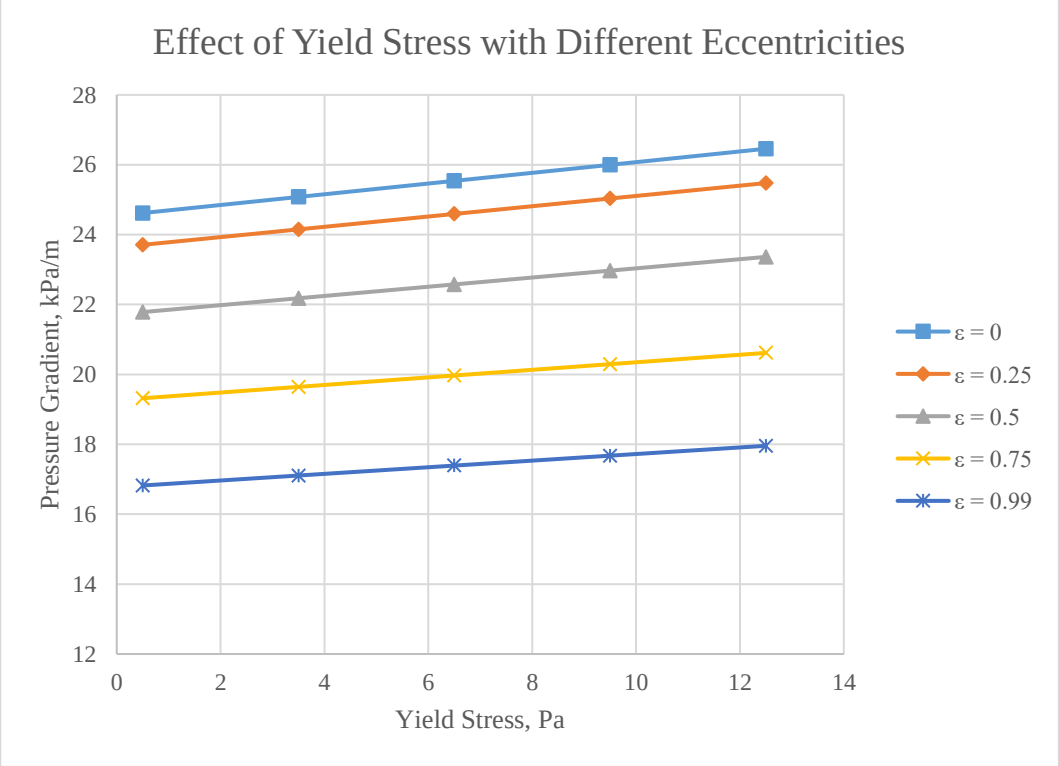

Figure 4.8 Effect of Yield Stress on Surge and Swab Pressures of YPL Fluids with Varying Eccentricities

The effect of flow behavior index on surge and swab pressures of YPL fluids with varying eccentricity while running a 1-in pipe into 2-in hole is shown in Figure 4.9. It can be easily seen that the exponential nature of flow behavior index that is shown in YPL model equation Eq. 2-4 in Chapter 2 causes the exponential increase in

pressures. However, it is important to note that comparison between fully concentric to fully eccentric yields a pressure loss reduction of 28% in fluids with high flow behavior index, i.e., $n = 0.9$, and a pressure loss reduction of 45% in fluids with low flow behavior index, i.e., $n = 0.3$ using this dataset. Inputs for this sensitivity analysis are listed in Table 4.3.

Table 4.3 Input Parameters for Sensitivity Analysis Shown in Figure 4.9

$V_p, m/s$	n	$K, Pa.s^n$	τ_y, Pa	R_o, m	R_i, m	R_i/R_o	ε
1.2	0.3	0.3	6.5	0.0254	0.0127	0.50	0
	0.45						0.25
	0.60						0.50
	0.75						0.75
	0.90						0.99

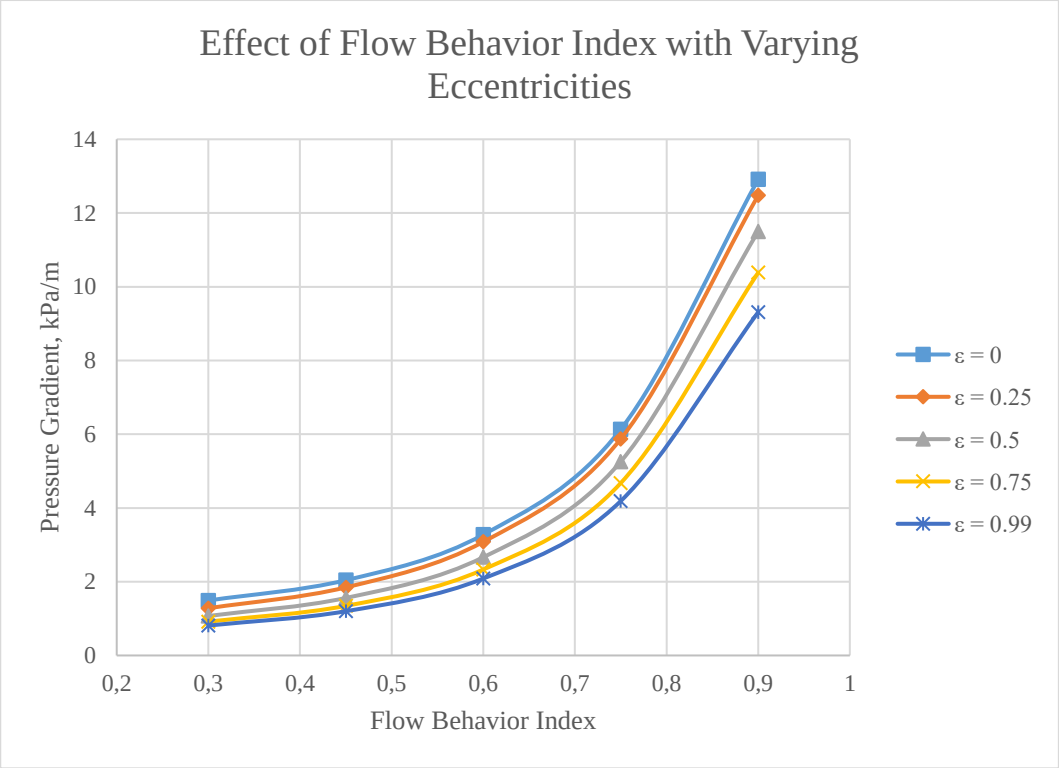

Figure 4.9 Effect of Flow Behavior Index on Surge and Swab Pressures of YPL Fluids with Varying Eccentricities

Figure 4.10 shows the effect of tripping speed on surge and swab pressures of YPL fluids with varying eccentricity in a geometric representation of a laboratory scale experiment; running a 1 1/3-in pipe in a 2-in hole. As expected, pipe velocity is directly proportional with the surge and swab pressure losses. Additionally, pipe being offcenter reduces the pressures losses up to 40% using this particular input dataset. All inputs for this study are listed in Table 4.4 below:

Table 4.4 Input Parameters for Sensitivity Analysis Shown in Figure 4.10

$V_p, m/s$	n	$K, Pa.s^n$	τ_y, Pa	R_o, m	R_i, m	R_i/R_o	ε
0.3							0
0.6							0.25
0.9	0.3	1.5	3.5	0.0254	0.0167	0.66	0.50
1.2							0.75
1.5							0.99

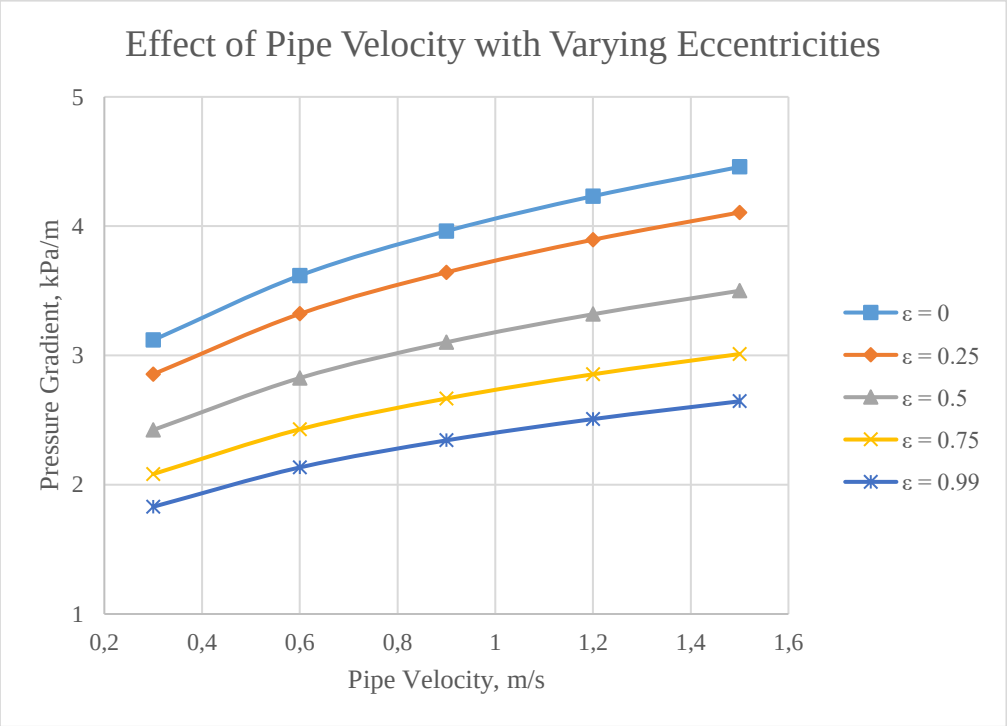

Figure 4.10 Effect of Pipe Velocity on Surge and Swab Pressures of YPL Fluids with Varying Eccentricities

The effect of yield stress is investigated a second time using different geometry and input dataset. Figure 4.11 illustrates this effect using a drilling fluid with smaller consistency index and flow behavior index than the one shown in Figure 4.8. The wellbore geometry represents a common scenario such that running a 6 ¼-in pipe

into a 12 ¼-in hole. Similar relationship between yield stress and pressure losses is expected and obviously seen in the above figure. In line with previous sensitivity analyses, increasing the eccentricity decreases the pressure loss gradient up to 40% and up to 46% while running the drilling fluids with $\tau_y = 0.5\ Pa$ and $\tau_y = 12.5\ Pa$, respectively. The inputs for this study is given in Table 4.5.

Table 4.5 Input Parameters for Sensitivity Analysis Shown in Figure 4.11

$V_p, m/s$	n	$K, Pa.s^n$	τ_y, Pa	R_o, m	R_i, m	R_i/R_o	ε
0.9	0.3	0.9	0.5 3.5 6.5 9.5 12.5	0.15557	0.07937	0.51	0 0.25 0.50 0.75 0.99

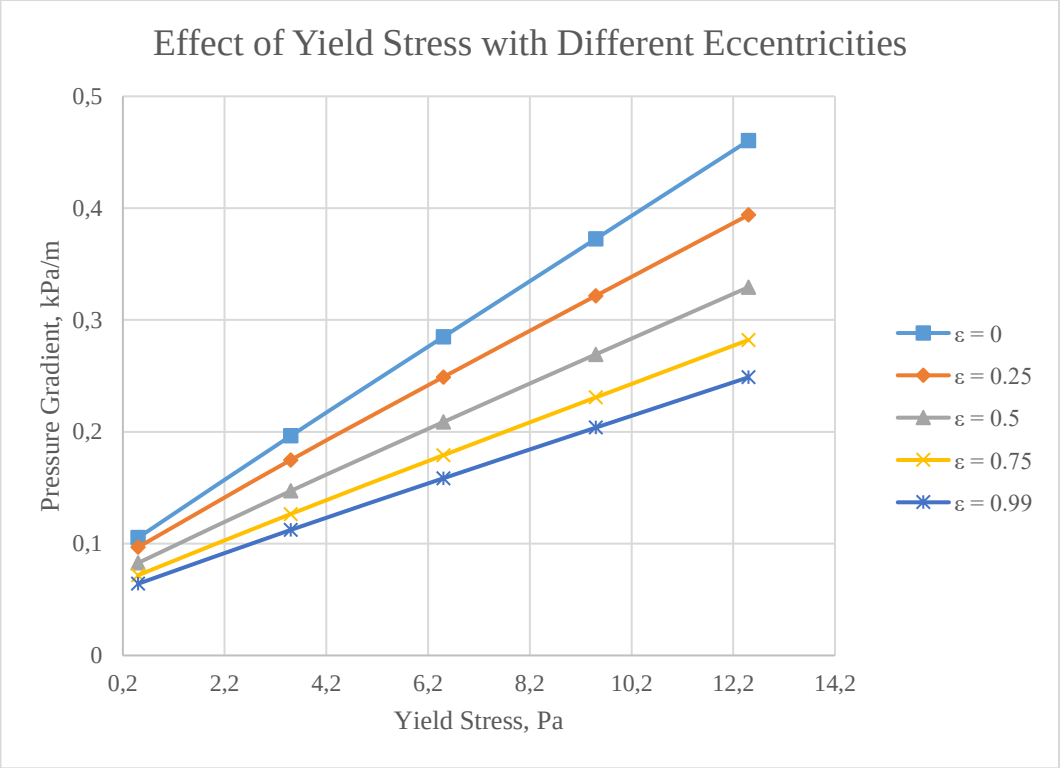

Figure 4.11 Effect of Yield Stress on Surge and Swab Pressures of YPL Fluids with Varying Eccentricities

Last sensitivity analysis is conducted to present the effect of diameter ratio on surge and swab pressures with varying eccentricity. When constructing the wellbore geometry, in this case, a 8 ½-in hole is picked; with varying inner pipes to correspond to a diameter ratio with a relatively large annular gap of 0.35 to smaller annular clearance of 0.82. It is seen that smaller annular gap contributes to higher pressure losses while tripping exponentially. Moreover, as observed in previous sensitivity analyses, eccentricity has an inverse proportionality with surge and swab pressure losses; up to 45% in this particular example. Table 4.6 lists the input parameters for this study.

Table 4.6 Input Parameters for Sensitivity Analysis Shown in Figure 4.12

$V_p, m/s$	n	$K, Pa.s^n$	τ_y, Pa	R_o, m	R_i, m	R_i/R_o	ε
0.3	0.3	0.6	9.5	0.2159	0.0762	0.35	0
				0.2159	0.1016	0.47	0.25
				0.2159	0.127	0.59	0.50
				0.2159	0.1524	0.71	0.75
				0.2159	0.1778	0.82	0.99

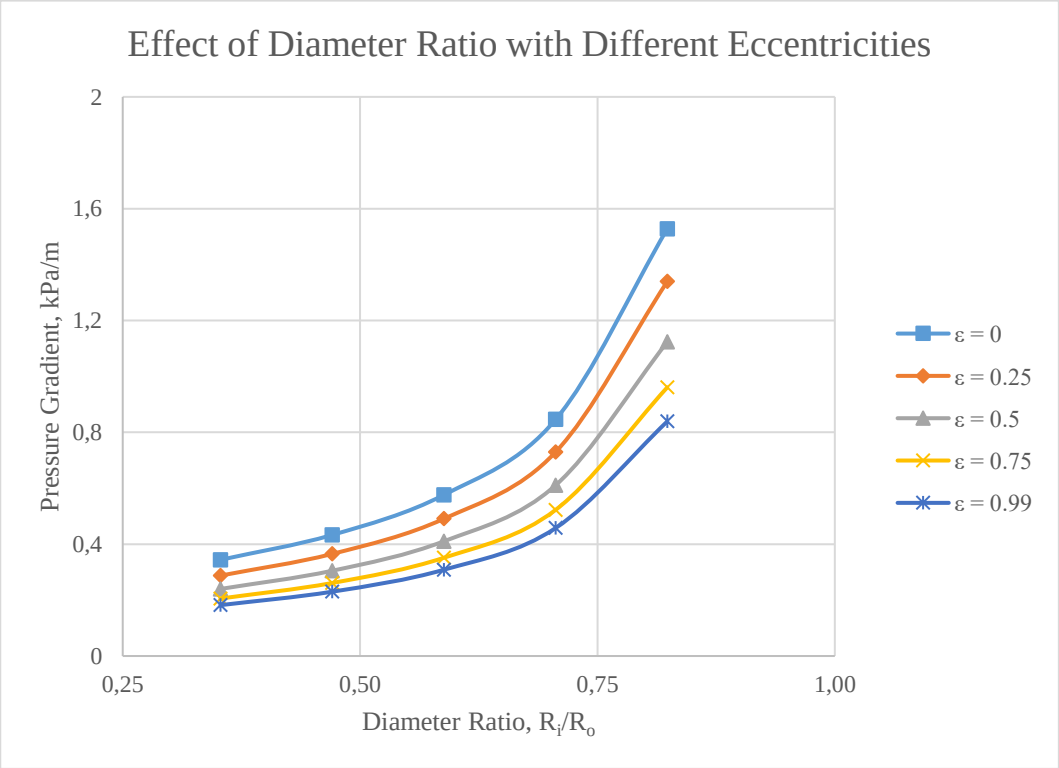

Figure 4.12 Effect of Diameter Ratio on Surge and Swab Pressures of YPL Fluids with Varying Eccentricities

Now, in the second part of the sensitivity analysis, input values are selected from a fixed pool of database which is shown in Table 4.7. While showing the effect of one input parameter with changing eccentricity on resulting surge and swab pressures, all other input values were kept constant. Figures from Figure 4.13 to Figure 4.17 represent the effect of diameter ratio, yield stress, pipe velocity, flow behavior index and consistency index on surge and swab pressure gradients, respectively.

Table 4.7 Input Parameters for Sensitivity Analysis Shown between Figure 4.13 to Figure 4.17

$V_p, m/s$	n	$K, Pa.s^n$	τ_y, Pa	R_o, m	R_i, m	R_i/R_o	ε
0.3	0.3	0.6	9.5	0.10795	0.0762	0.71	0 0.25 0.50 0.75 0.99

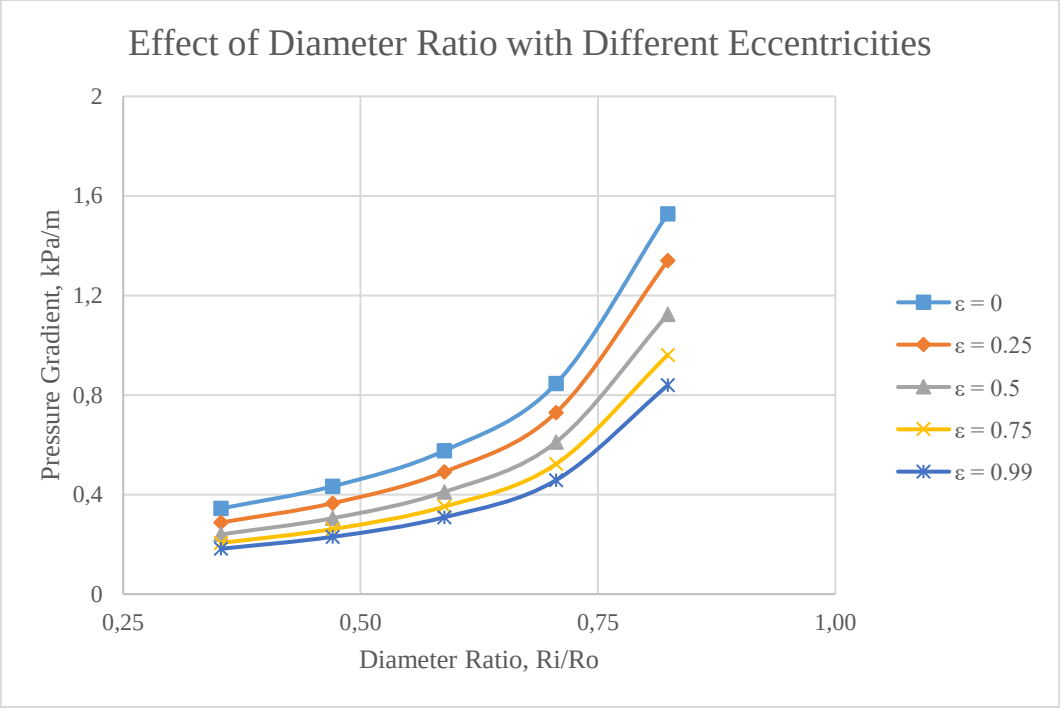

Figure 4.13 Effect of Diameter Ratio on Surge and Swab Pressures of YPL Fluids with Varying Eccentricities-II

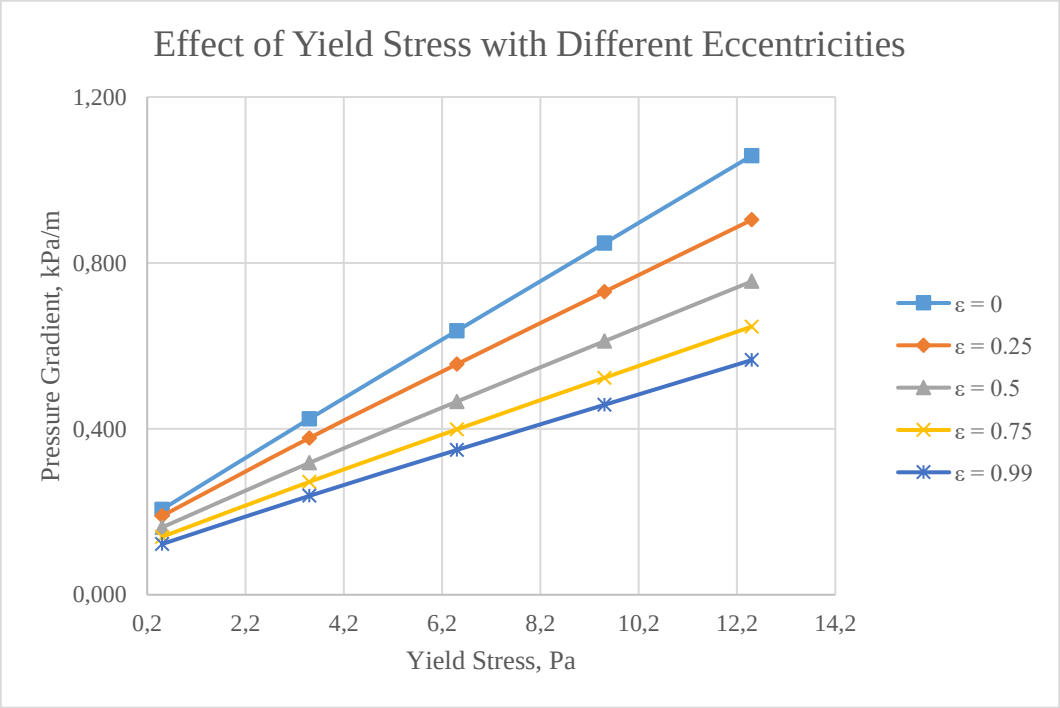

Figure 4.14 Effect of Yield Stress on Surge and Swab Pressures of YPL Fluids with Varying Eccentricities-II

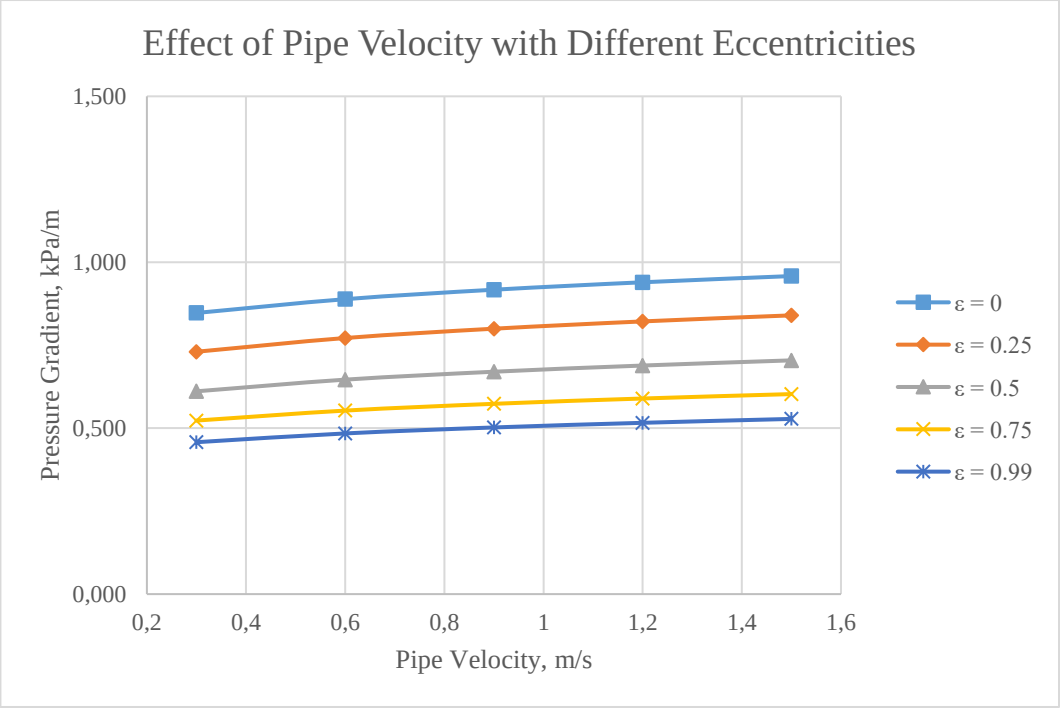

Figure 4.15 Effect of Pipe Velocity on Surge and Swab Pressures of YPL Fluids with Varying Eccentricities-II

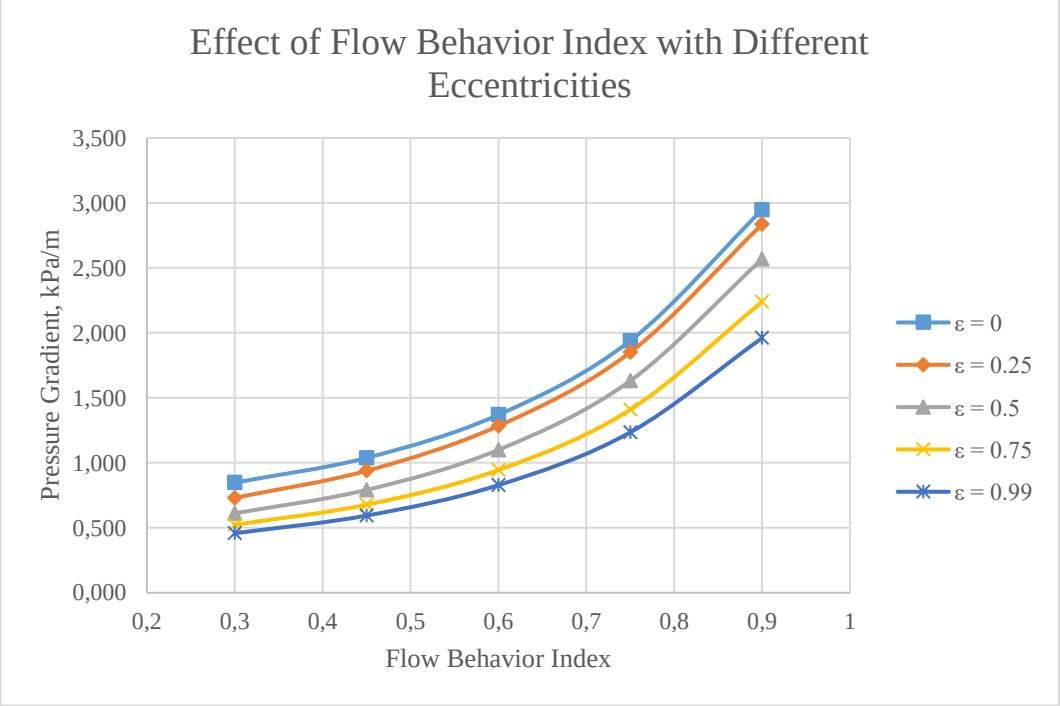

Figure 4.16 Effect of Flow Behavior Index on Surge and Swab Pressures of YPL Fluids with Varying Eccentricities-II

Figure 4.17 Effect of Consistency Index on Surge and Swab Pressures of YPL Fluids with Varying Eccentricities-II

The parametric study provides valuable insights into the sensitivity of surge and swab pressures to various parameters in the YPL fluid model. The results highlight the direct proportional relationship between surge and swab pressures and parameters such as flow behavior index, yield stress, consistency index, diameter ratio, and pipe velocity. This implies that an increase in these parameters corresponds to an increase in surge and swab pressures.

Furthermore, the study reveals that the effects of diameter ratio and flow behavior index on surge and swab pressures are more pronounced due to their exponential nature. This relationship can be seen in Eq. 2-4, Eq. 4-8. This indicates that even small changes in these parameters can significantly impact the resulting pressure profiles. On the other hand, the study shows an inverse relationship between eccentricity and surge and swab pressures. Comparing a concentric case to a fully

eccentric one, it is observed that surge and swab pressures decrease significantly in the eccentric configuration.

CHAPTER 5

EFFECT OF TEMPERATURE ON RHEOLOGICAL PARAMETERS AND SURGE AND SWAB PRESSURE LOSSES

5.1 Calculation of Non-Newtonian Fluid Models' Rheological Parameters

The whole concept of drilling hydraulics focuses on calculating and optimizing pressure losses through different fluid paths, annuli, elbows, obstacles and nozzles. The equations for calculating pressure losses heavily depend on the drilling fluids' rheological model and the model paramaters. A thorough explanation and background about rheological models and behavior of drilling fluids is given in Chapter 2 of this thesis.

The fluid models' parameters come from corresponding model's own shear stress equations. Below equations belong to the three most common Non-Newtonian fluid models; Power Law, Bingham Plastic and Yield Power Law, respectively:

$$\tau = K\gamma^{n} \tag{5-1}$$

$$\tau = \tau_{y} + \mu_{p}\gamma \tag{5-2}$$

$$\tau = \tau_{y} + K\gamma^{n} \tag{5-3}$$

It is a common practice to employ empirical equations for determining the model parameters. The raw data to feed these empirical equations originates from testing the drilling fluid using a viscometer. Both laboratory and field work in the oil and

gas industry extensively rely on the utilization of 6-speed or 8-speed rotational viscometers for this purpose. Rotational viscometers provide shear stress, dial readings, of the fluid at several pre-determined shear rates. Empirical equations use these dial readings to calculate flow behavior index, n, consistency index, k, yield stress, τ_y and the other related parameters of each model.

The most widely used and accepted empirical equations are given in the relevant one in American Petroleum Institute Recommended Practices series. The most recent version of API RP 13D Rheology and Hydraulics of Oil-Well Drilling Fluids uses the below equations to calculate aforementioned fluid model parameters for Yield Power Law fluids (API, 2017):

$$\tau_y = 2R_3 - R_6 \tag{5-4}$$

$$n = 3.32 \log_{10}\left(\frac{R_{600} - \tau_y}{R_{300} - \tau_y}\right) \tag{5-5}$$

$$k = \frac{\left(R_{300} - \tau_y\right)}{511^n} \tag{5-6}$$

Where R_N represents the dial reading from rotational viscometer while at N rpm.

This study feautres a novel and superior way to calculate the fluid's rheological parameters. Instead of using empirical equations, shear rate and shear stress data from viscometer dial readings are utilized with regards to every fluid model's own equation. By doing that, regression analysis was performed and coded in MATLAB to provide fluid model parameters. A graphical user interface, GUI, was constructed to serve as a user friendly platform.

In-house developed software has 10 inputs for dial readings for a set of 10 pre-determined shear rates; which are; R_{600}, R_{300}, R_{200}, R_{100}, R_{60}, R_{30}, R_{20}, R_{10}, R_6, and R_3. While it is possible to enter all 10 dial readings to calculate the fluid model parameters, one can enter only 3 dial readings to initiate the calculation. However, 6 dial readings, which are R_{600}, R_{300}, R_{200}, R_{100}, R_6, and R_3, are considered as practical minimum; since 6-speed rotational viscometers commonly feature this particular configuration. Increasing the number of input dial readings obviously would lead to more accurate results.

The program draws a chart of shear rate versus shear stress with the data inputted by the user; with x axis being shear rate in 1/sec unit, and y axis being shear stress in Pa unit. It is possible to change the units by modifying the unit conversions embedded in the program. The default unit conversion from viscometer reading to shear stress units is selected as 1^o reading = 1.065 lb/100ft^2 = 0.51 Pa; as this ratio belongs to one of the most common rotational viscometer configuration of R1-B1 (rotor-bob combination) used in the industry. Similarly, 1 rpm = 1.7023 1/sec unit conversion and Shear Rate = 1.7023 x N formula are used considering the same configuration with F1 torsion spring constant.

Homepage of the GUI is shown in Figure 5.1.

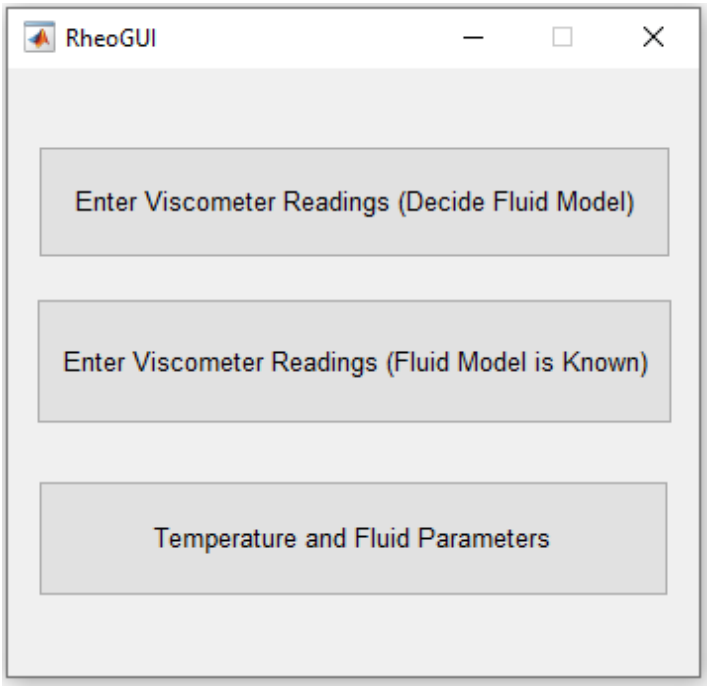

Figure 5.1 Homepage of the GUI Developed to Calculate Fluid Model Parameters

As seen from the figure, the software requests user to enter viscometer readings in two separate options. First one makes the user enter viscometer readings, and the program utilizes a least squares regression of viscometer readings for best-fitted fluid model and selects the one with the highest R^2 while utilizing every fluid model's own equation. Several examples of "Decide Fluid Model" option with input and output screenshots are given in figures from Figure 5.2 to Figure 5.5.

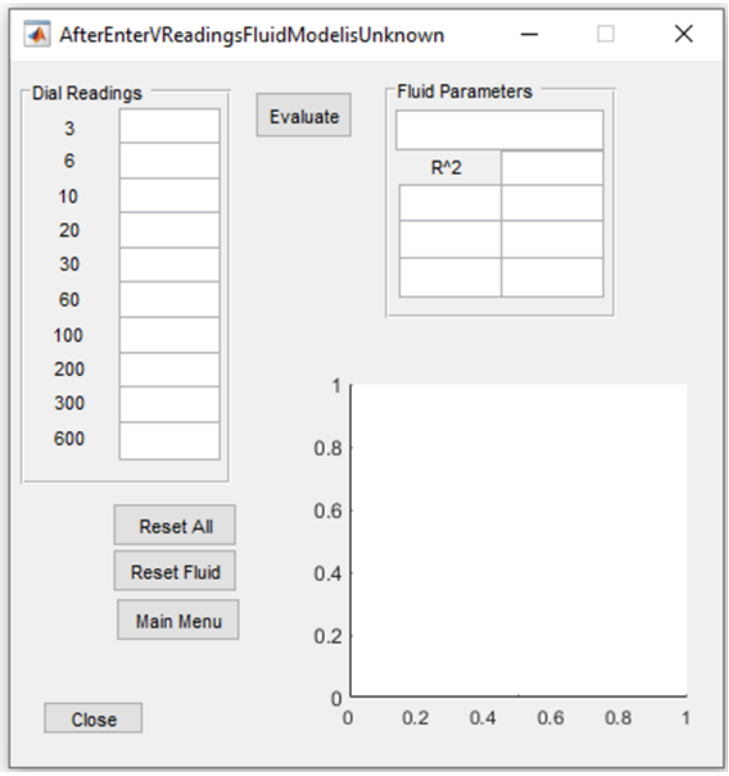

Figure 5.2 “Decide Fluid Model” Option Inputs

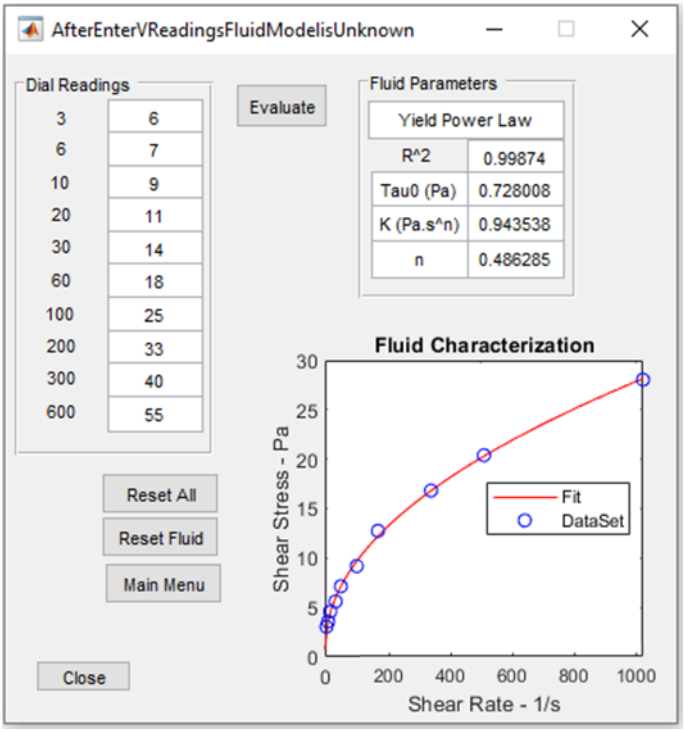

Figure 5.3 “Decide Fluid Model” Option Output with Yield Power Law Fluid

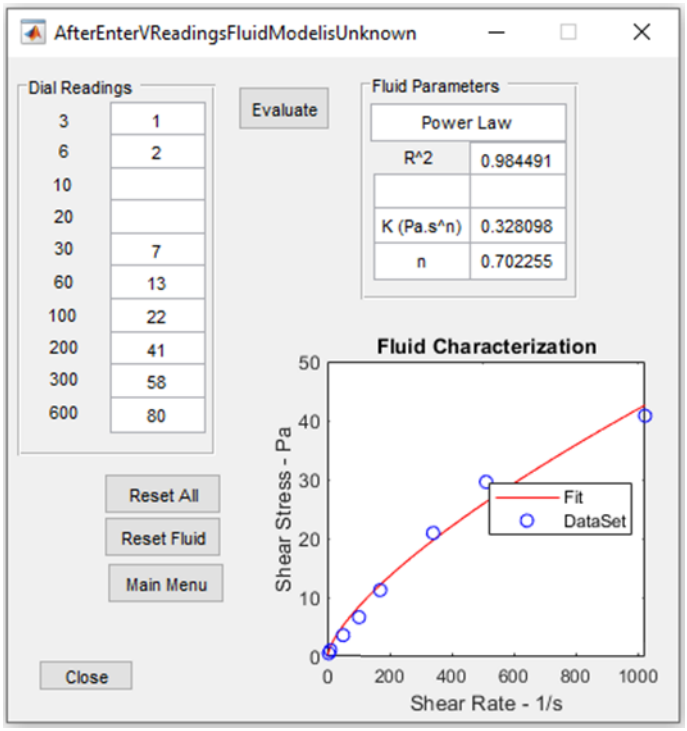

Figure 5.4 “Decide Fluid Model” Option Output with Power Law Fluid

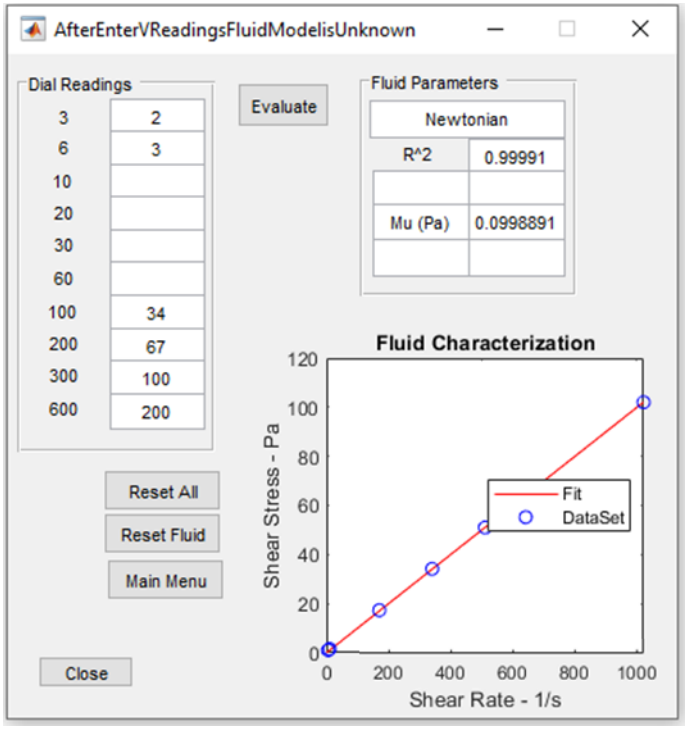

Figure 5.5 “Decide Fluid Model” Option Output with Newtonian Fluid

The second option in Figure 5.1 is also self explanatory; i.e, user selects the fluid model after inputting dial readings, then the program will output the rheological parameters of the selected fluid model. The coefficient of determination, R^2 value, is also calculated and presented to show the fitness of the model with the inputted dial readings with regards to corresponding shear rates. Following figures from Figure 5.6 to 5.10 show the outputs after selecting different models.

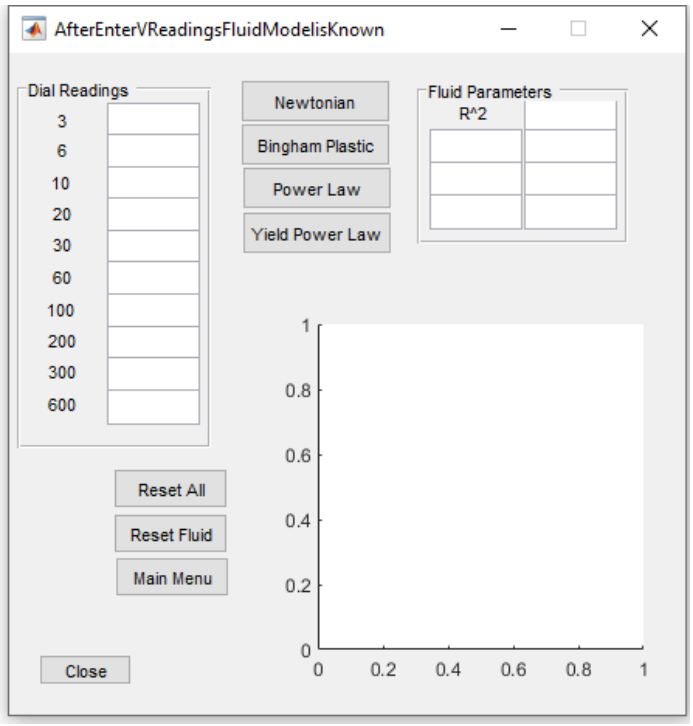

Figure 5.6 “Fluid Model is Known” Option Inputs

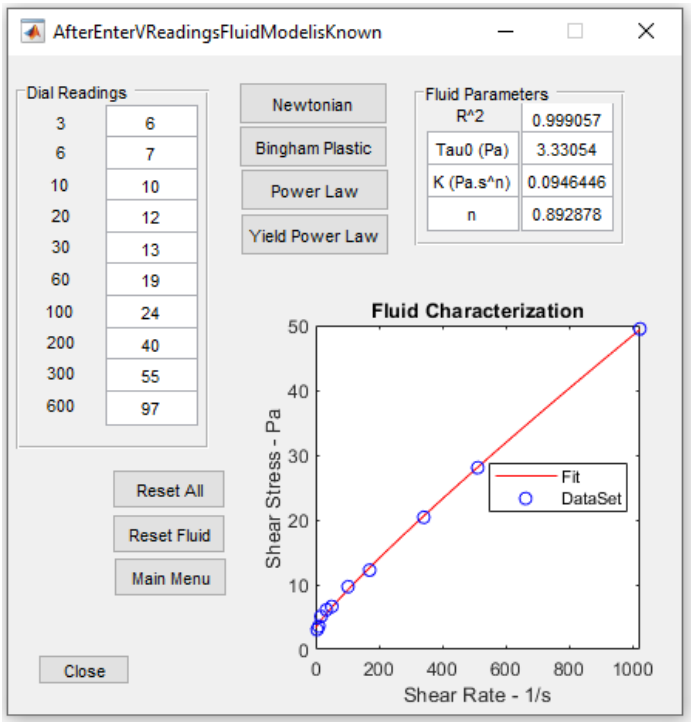

Figure 5.7 “Fluid Model is Known” Option Output with Yield Power Law Fluid

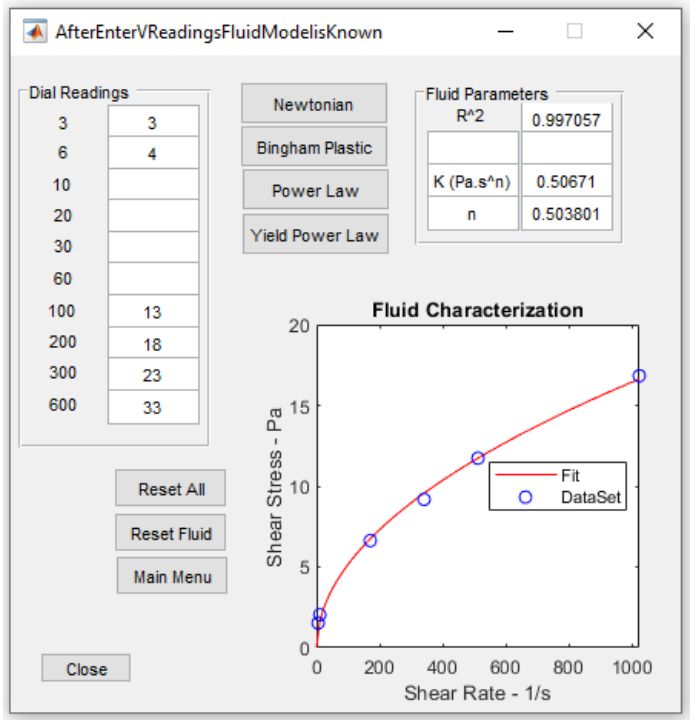

Figure 5.8 “Fluid Model is Known” Option Output with Power Law Fluid

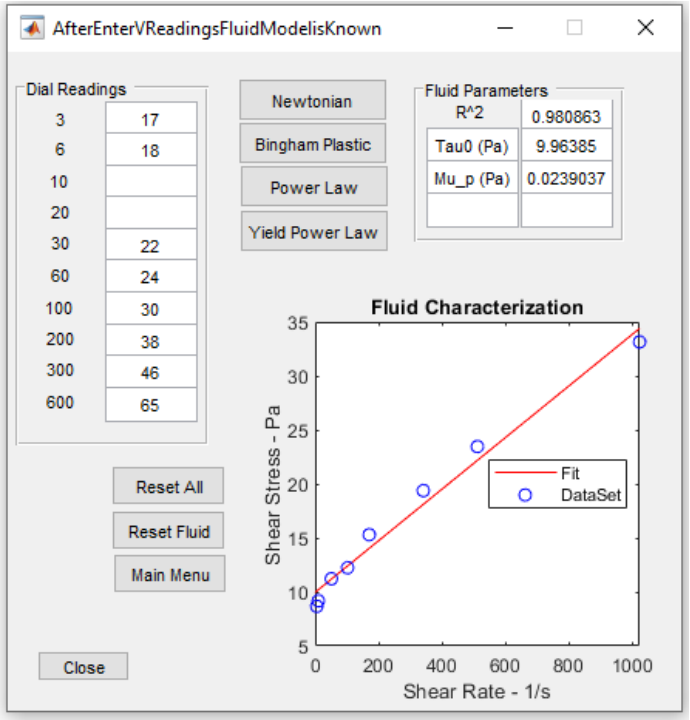

Figure 5.9 “Fluid Model is Known” Option Output with Bingham Plastic Fluid

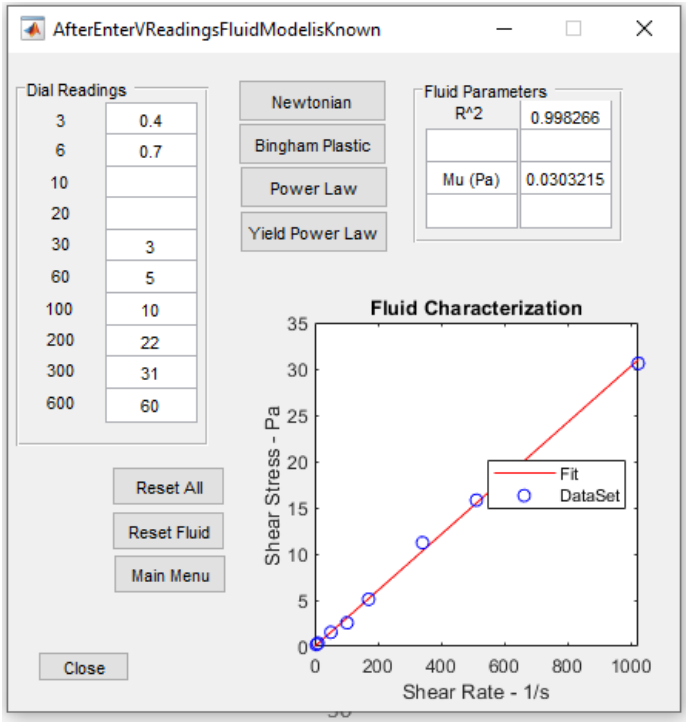

Figure 5.10 “Fluid Model is Known” Option Output with Newtonian Fluid

Plotting data set in the shear rate versus shear stress chart while an automatically-drawn curve fit which originates from the fluid models' own equation facilitates an R^2 value to illustrate fitness of the model to original rotational viscometer readings. By doing so, this study enables a more statistically correct and precise method to calculate fluid parameters when comparing with employing empirical equations.

A comparative study was conducted between the rheological model parameters resulted from regression analysis and from empirical equations taken from API RP 13D, Rheology and Hydraulics of Oil-Well Drilling Fluids (API, 2017). Four different water based drilling fluids that are used in different sections of an oil well were tested for their rheology in a 6-speed rotational viscometer. The fluid parameters for Yield Power Law model were calculated using two different methods, proposed method(PM) and API's empirical equations(API) and presented in Table 5.1.

Table 5.1 A Comparison of Rheological Parameters Estimated by Proposed Method (PM) and API's Empirical Equations (API)

	Fluid 1		**Fluid 2**		**Fluid 3**		**Fluid 4**	
R_{600}	42		50		64		84	
R_{300}	28		35		44		52	
R_{200}	20		28		35		37	
R_{100}	12		20		27		23	
R_6	4		7		12		6	
R_3	3		6		11		5	
PM / API	**PM**	**API**	**PM**	**API**	**PM**	**API**	**PM**	**API**
τ_y, Pa	1.038	0.94	1.86	2.35	4.52	4.7	1.739	1.88
$K, Pa.s^n$	0.124	0.253	0.383	0.367	0.272	0.272	0.171	0.228
n	0.727	0.621	0.585	0.584	0.658	0.667	0.782	0.736

Another advantage of this program is that it allows users to calculate the drilling fluids' rheological parameters more easily when only data available is the viscometer

readings. In most laboratory work results, and some of the experimental and/or model results from the journal papers in the literature that includes drilling fluid rheology only presents the dial readings; i.e, the rheological fluid parameters are absent. Therefore, it allows users to calculate and compare their work in such cases.

5.2 Effect of Temperature on Rheology and Surge and Swab Pressures

It is well known that temperature has significant effect on fluid rheology, which consequently affects the pressure loss and equivalent circulating density (ECD) (Bartlett (1967), and Rommetveit and Bjørkevoll (1997)). This effect may be in favor of direct proportionality, i.e, increasing the temperature may increase the rheology of fluid, or may be the exact opposite; inverse proportionality. This depends on the fluid type and nature of the drilling fluid used (Ettehadi and Altun, 2018 & Altun et al., 2014).

In order to account for this effect in the surge and swab model, a data-driven approach is used. The third option in Figure 5.1, “Temperature and Fluid Parameters” allows users to input several rheological parameters at different temperatures and enter the temperature at point of interest. A second-degree polynomial function is fitted individually to each rheological model constants and the new rheological parameters are estimated for this temperature at point of interest. Figure 5.11 shows the input screenshot, while Figure 5.12 and Figure 5.13 show example outputs corresponding an interpolation and extrapolation examples, respectively. It should be noted that all the input data are considered to calculate interpolations and extrapolations.

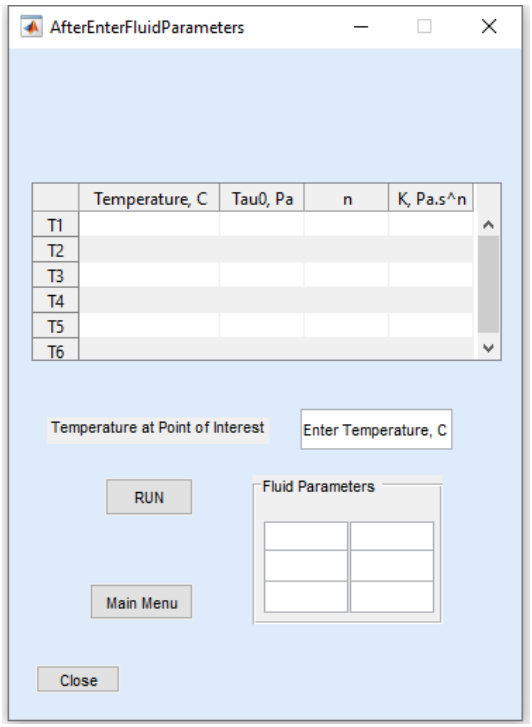

Figure 5.11 “Temperature and Fluid Parameters” Option Inputs

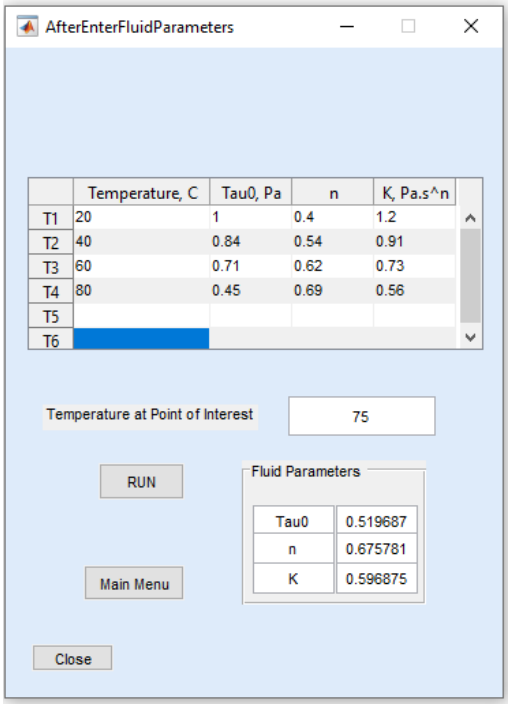

Figure 5.12 “Temperature and Fluid Parameters” Option Example Output-1 (Interpolation)

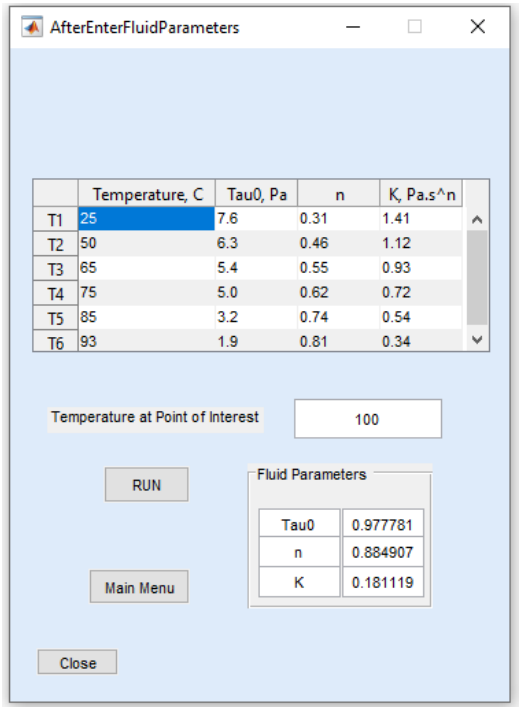

Figure 5.13 “Temperature and Fluid Parameters” Option Example Output-2 (Extrapolation)

An example case study was conducted that involved obtaining viscometer measurements of a single drilling fluid at 4 different temperatures (25°C, 49°C, 75°C, and 93°C). The regression analysis was performed using 3 of these temperature values (25°C, 49°C, and 93°C) and the last temperature (75°C) was used to evaluate the accuracy of the estimation. The results are presented in Table 5.2. Based on the statistical metrics reported, it appears that the data-driven model used in this study is able to estimate the rheological parameters with reasonable accuracy. The root mean square error (RMSE) value of 0.146 indicates that the model's predictions are, on average, within 0.146 units of the actual values. Additionally, the high R2 value of 0.97 suggests that a large proportion of the variance in the data is explained by the model, indicating a good fit.

Table 5.2 Rheological Characterization of a Drilling Fluid under 4 Different Temperatures (25°C, 49°C, 75°C, and 93°C); Measurements (M) vs Estimation (E)

	25°C (M)	49°C (M)	93°C (M)	75°C (M)	75°C (E)
R_{600}	70	64	49	60	-
R_{300}	54	44	33	45	-
R_{200}	43	35	25	28	-
R_{100}	29	25	17	19	-
R_6	9	6	4	5	-
R_3	8	5	3	4	-
τ_y, Pa	0.88	0.719	0.57	0.86	0.61
$K, Pa.s^n$	1.18	0.64	0.32	0.34	0.34
n	0.48	0.56	0.62	0.64	0.60

In order to reveal the effect of temperature a case study, which involves two cases for running an 8-in drill collar in a 12.25-in hole within same tripping speed, eccentricity, and with same drilling fluid but for different wellbore temperatures (Table 5.3) is presented. Increasing the dynamic wellbore temperature from 25°C to

100°C almost halved the pressure difference resulting from the axial movement of the inner pipe.

It should be noted that the severity of pressure loss with varying temperature depends on the drilling fluid used in the well; i.e, characteristic and nature of drilling fluid, which emerges from its behavior of the fluid used in the well under different temperatures. Yet again, using the same fluid and drilling parameters shown in the aforementioned example, the pressure gradient while tripping with 1 m/s for 25°C is the same while tripping with 3 m/s for 100°C. That alone shows that isothermal models developed for oil and gas wells should not be used in geothermal wells. There is a need to incorporate temperature effects into hydraulics simulations to reduce non productive time (NPT) in geothermal wells.

Table 5.3 Case Study-I for Temperature Effect on Surge and Swab Pressures

	25°C	**49°C**	**100°C**
τ_y, Pa	0.875	0.719	0.562
$K, Pa.s^n$	1.183	0.64	0.345
n	0.481	0.56	0.62
$V_p, m/s$	1.0	1.0	1.0
ε	0.7	0.7	0.7
R_i, m	0.2032	0.2032	0.2032
R_o, m	0.31115	0.31115	0.31115
R_i/R_o	0.65	0.65	0.65
$\frac{dp}{dl}, \frac{kPa}{m}$	**0.156**	**0.119**	**0.0836**

In order to highlight the changes in pressures with variation in temperature, a second case study, namely case study-II, is conducted. In this case study, two hypothetical wells, one of which is an oil well and the other is a geothermal well, with final depths of 3000 meter are selected. Well depths are divided into grids of 400 meters to capture the temperature distribution along the wellbore. The dynamic bottom hole

temperatures for each grid are inputted to account for the varying thermal conditions encountered during drilling and / or tripping.

It is known that high temperature is somewhat considered as contamination to drilling fluids in geothermal wells and has severe effects on rheology (Erge et al, 2020). The relationship between temperature and rheology mainly depends on the additives used in the formulation. An increase in the temperature may inherently trigger a decrease in the rheology; however, some additives may cause a contrary behavior, i.e., lead to a direct proportionality (Erge et al., 2022).

To quantify the rheological behavior of the drilling fluid at different temperatures, a set of 6-speed viscometer dial readings was collected. These dial readings served as inputs for determining the yield stress, flow behavior index, and consistency index for the YPL fluid model utilizing the tool developed for this purpose. Incorporating the rheological parameters, the proposed numerical model was utilized to calculate surge and swab pressure gradients for each grid in both hypothetical wells.

Table 5.4 shows the stationary parameters for case study-II; the wellbore geometry, eccentricity and the pipe velocity inputs. These inputs are selected since they have strong potential to reflect actual field conditions, such as running a 6.5-in drill collar ($R_i = 0.08255\ m$) into an 8.5-in hole ($R_o = 0.10795\ m$) with a velocity of $V_p = 0.5\ m/s$ in a highly eccentric condition with $\varepsilon = 0.8$.

Table 5.5 and Table 5.6 show the dynamic bottom hole temperatures, rheological parameters of drilling fluids, and resulting surge and swab pressure gradients for oil well and geothermal well, respectively. The results shown in tables align with previous case study.

Table 5.4 Inputs for Both Hypothetical Wells used in Case Study-II

$V_p, m/s$	R_o, m	R_i, m	R_i/R_o	ε
0.5	0.10795	0.08255	0.76	0.8

Table 5.5 Case Study-II Inputs and Outputs for Each Grid in Oil Well

$Depth, m$	$Dynamic\ BHT\ Oil\ Well, ℃$	τ_y, Pa	n	$K, Pa.s^n$	$\frac{dp}{dl}, \frac{kPa}{m}$
0	25	3.737	0.669	0.381	1.171
400	30	3.730	0.684	0.340	1.141
800	40	3.690	0.696	0.297	1.079
1200	50	3.590	0.713	0.253	1.018
1600	60	3.416	0.741	0.192	0.917
2000	70	3.226	0.754	0.157	0.820
2400	80	3.045	0.796	0.109	0.732
2800	90	2.824	0.828	0.080	0.651
3000	95	2.641	0.900	0.046	0.571

Table 5.6 Case Study-II Inputs and Outputs for Each Grid in Geothermal Well

$Depth, m$	$Dynamic\ BHT\ Geoth.Well, ℃$	τ_y, Pa	n	$K, Pa.s^n$	$\frac{dp}{dl}, \frac{kPa}{m}$
0	25	3.737	0.669	0.381	1.171
400	31	3.730	0.678	0.349	1.136
800	43	3.725	0.752	0.184	0.950
1200	59	3.416	0.741	0.192	0.917
1600	75	3.224	0.832	0.090	0.744
2000	91	2.711	0.852	0.067	0.621
2400	107	2.283	0.848	0.056	0.511
2800	123	1.828	0.829	0.055	0.441
3000	131	1.662	0.823	0.053	0.406

To further illustrate the effect of temperature on surge and swab pressures; case study-II was integrated into a pressure chart; which is commonly used in commercial

drilling hydraulics softwares (Aspen Sysdrill, 2023 & PVI Software, 2023). The pressure chart shows the pore pressure and fracture pressure variations with same grids for both of the hypothetical wells. It also has drilling fluid density, i.e., mud weight, and surge and swab pressure gradients with unit conversions taken from case study-II. Table 5.7 lists the pore pressure gradient, fracture pressure gradient and the drilling fluid density for each 400 m of the wells. It also shows the surge and swab pressure gradients for both geothermal and oil wells. Surge and swab pressure gradients are calculated with addition and subtraction of dp/dl to mud weight, respectively.

Drilling fluid density used in this case study is selected as 1.20 SG, while the pore pressure and fracture pressure gradients varies with minimum of 1.02 SG to maximum of 1.38 SG, respectively. Mud weight is assumed to be stay constant at 1.20 SG value in every depth of the well, i.e, density variation due to temperature is neglected. As discussed in the early chapters of this thesis, it is of vital importance to stay in mud window while tripping to avoid hazards such as an influx from hole or inducing a downhole loss. Therefore, in this example, ECD should remain between the pore and fracture pressure gradients listed in Table 5.7 during tripping while maintaining the maximum velocity possible.

Table 5.7 Pressure Gradient Input and Outputs for Both Hypothetical Wells

				Geothermal Well		Oil Well	
$Depth, m$	$Pore\ P.G., SG$	$Fracture\ P.G., SG$	MW, SG	$Surge\ P.G., SG$	$Swab\ P.G., SG$	$Surge\ P.G., SG$	$Swab\ P.G., SG$
0	1.02	1.38	1.20	1.32	1.08	1.32	1.08
400	1.02	1.38	1.20	1.32	1.08	1.32	1.08
800	1.08	1.31	1.20	1.30	1.10	1.31	1.09
1200	1.08	1.31	1.20	1.29	1.11	1.30	1.10
1600	1.08	1.32	1.20	1.28	1.12	1.29	1.11
2000	1.13	1.36	1.20	1.26	1.14	1.28	1.12
2400	1.13	1.37	1.20	1.25	1.15	1.28	1.13
2800	1.13	1.32	1.20	1.25	1.16	1.27	1.13
3000	1.08	1.32	1.20	1.24	1.16	1.26	1.14

Figure 5.14 and Figure 5.15 represent the pressure gradient charts using the data in Table 5.7 for the geothermal well and oil well, respectively.

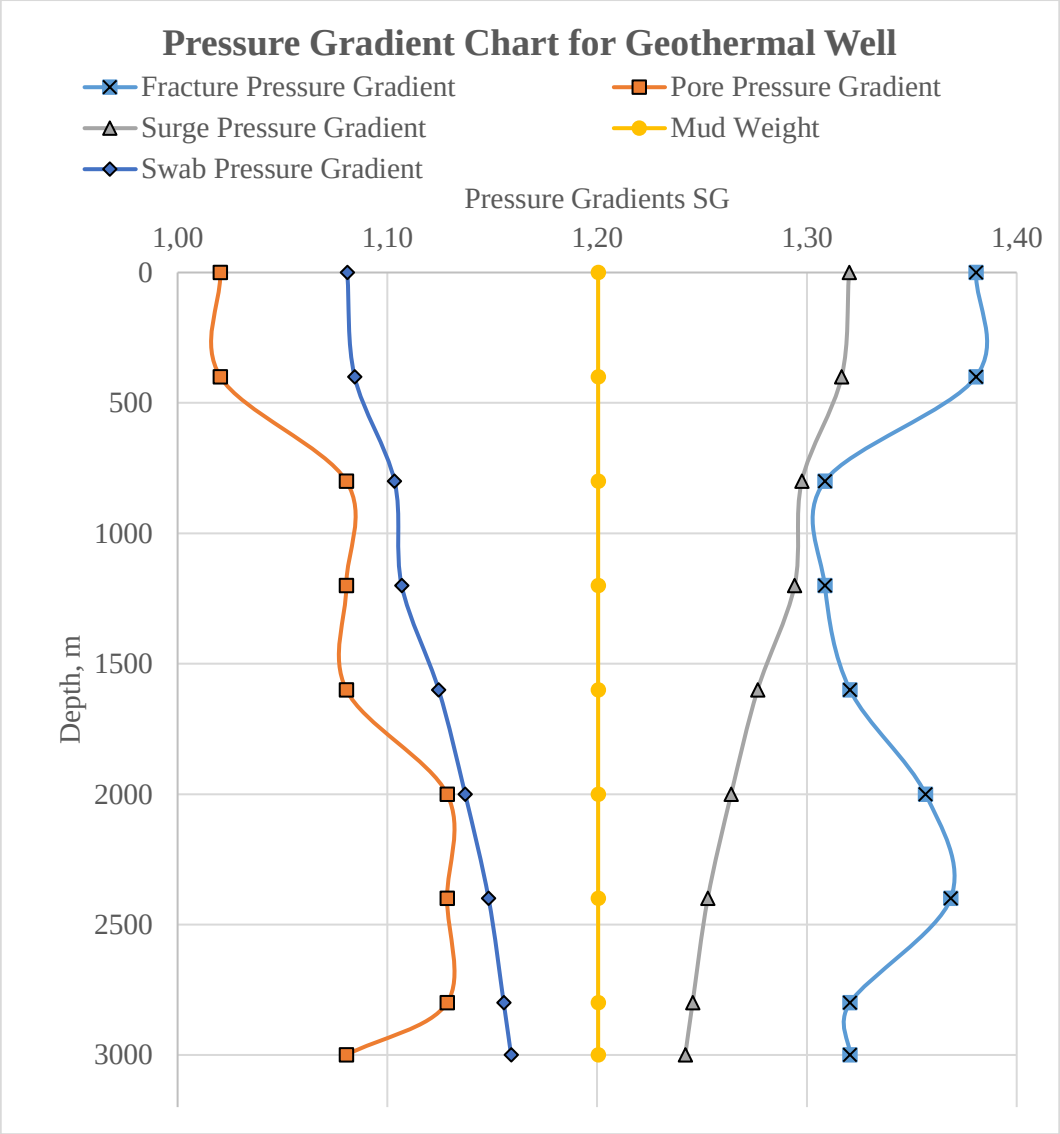

Figure 5.14 Pressure Gradient Chart for Geothermal Well in Case Study-II

As shown in Figure 5.14, a round trip in the 8.5-in hole section of the geothermal well with constant tripping velocity of $V_p = 0.5\ m/s$ while using a 1.20 SG drilling fluid and other input parameters listed in previous tables yield a satisfactory results in terms of ECD being kept in the desired interval.

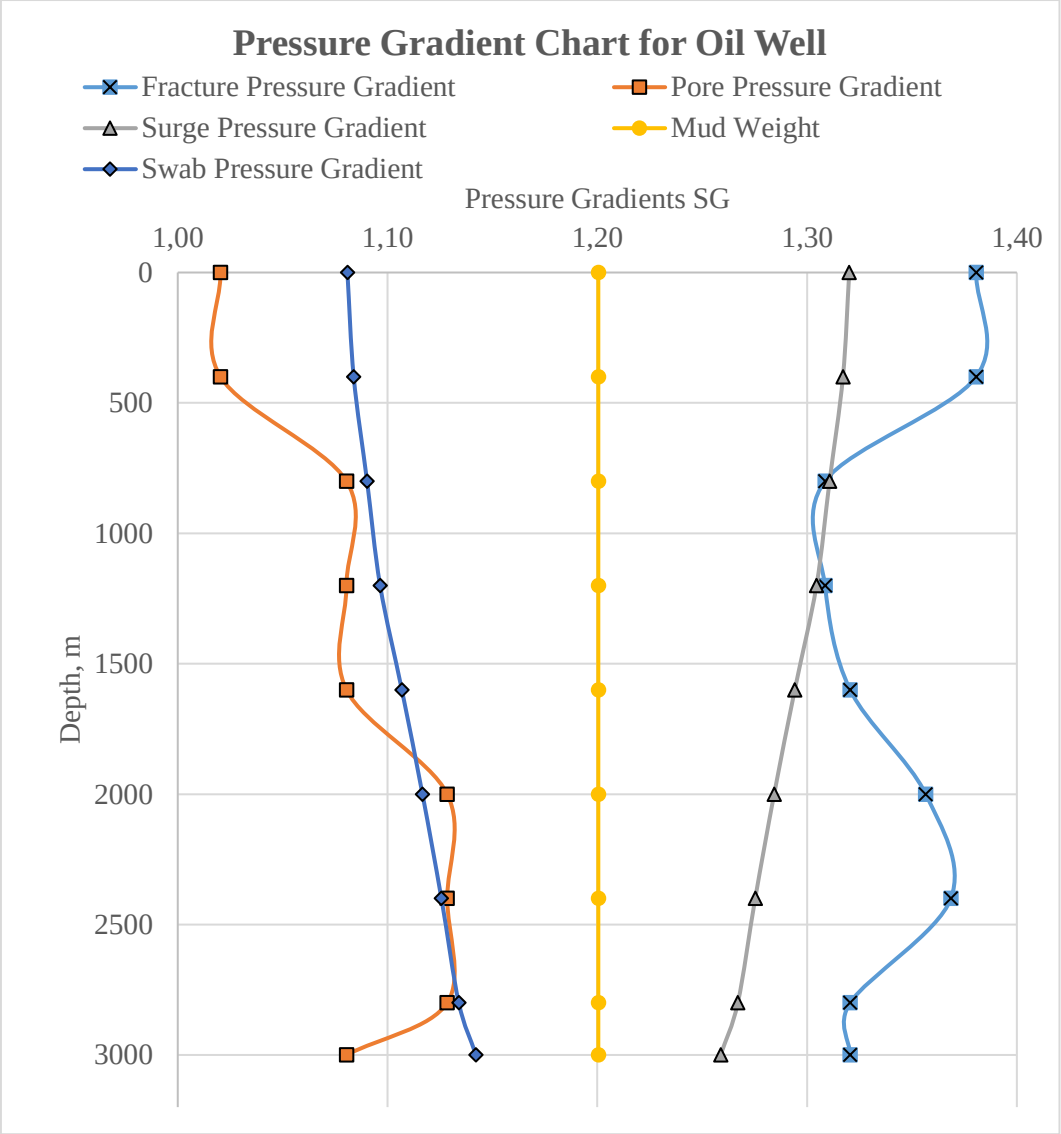

Figure 5.15 Pressure Gradient Chart for Oil Well in Case Study-II

Figure 5.15 inherets a similar scenario with Figure 5.14; however, it shows the pressure gradient chart for oil well instead of geothermal well. A comparison of two cases reveals that, despite using identical drilling fluid density, rheology, pore and fracture pressures, tripping speed, eccentricity and wellbore geometry, there are certain intervals in Figure 5.15 that deviate from the expected working pressure window. The only distinguishing factor between the two cases is the temperature

profile in the wells. As seen in Figure 5.15, same tripping speed would cause surge pressure to exceed the fracture pressure at around 800 meters. Similarly, pulling out of hole would cause a reduction in ECD below the working limit of pore pressure gradient from 1800 meters to 2800 meters.

The results of the case study highlighted the significant influence of temperature on the rheological properties of the drilling fluid and subsequently on surge and swab pressures. In the geothermal well, where temperatures were higher compared to the oil and gas wells, the rheology of the fluid was lower, resulting in lower surge and swab pressure gradients. This observation aligns with the expected behavior, as higher temperatures typically lead to decreased apparent viscosity and yield stress of the drilling fluid.

The findings from this case study emphasize the importance of considering temperature effects when evaluating surge and swab pressures in drilling operations. By accounting for temperature variations and their impact on fluid rheology, drilling engineers and operators can better anticipate and manage pressure-related issues during drilling and tripping. This knowledge is particularly valuable in geothermal drilling, where higher temperatures are encountered, as it allows for higher tripping speeds than oil wells. Overall, the case study demonstrates the significance of incorporating temperature considerations into drilling fluid models and highlights the practical implications for optimizing drilling practices in different thermal environments.

CHAPTER 6

CFD ANALYSIS AND VALIDATION OF THE PROPOSED MODEL

6.1 Computational Fluid Dynamics Setup and Comparative Study

Computational Fluid Dynamics (CFD) involves using computer resources to simulate flow problems, including fluid flow, mass transfer, and heat transfer. The recent advances in computer science and engineering have led to solution of more complex problems such as non-Newtonian fluid flows in complicated geometries using CFD approach (Sorgun, 2011). In this study, ANSYS Fluent 2020 R2, was used to simulate the flow in eccentric annuli when the inner pipe (drill pipe) is reciprocated, while outer pipe (borehole wall) remains stationary (ANSYS Inc., 2020).

In order to validate the developed model, a hypothetical test case where circular tubes with different dimensionless eccentricities, $\varepsilon = 0$, $\varepsilon = 0.3$, $\varepsilon = 0.5$, $\varepsilon = 0.7$ are drawn in geometry section with dimensions of; R_o = 0.0254 m (1-inch), R_i = 0.016764 m (0.66-inch) and elongated for 3 meters long are used. While selecting the length of fluid body, several different scenarios were tested. Similar to the grid independency study, which is presented later in this chapter, different lengths were used in the analysis for testing purpose and resulting pressure and velocity values were investigated. Starting from the shortest length of 20 cm, fluid body length systematically increased up to 5 meter while looking into the resulting pressure gradient chart and velocity contours, similar to the one presented in Figure 6.2. Results show that fluid bodies with less than 70 cm have fluctuations in pressures at inlet and outlets. This may be an indication of insufficient number of elements to reach the fully developed flow due to reciprocation of inner pipe. Similarly, velocity contours did not reflect the whole annulus well as in Figure 6.2. With fluid bodies longer than 70 cm, same analyses indicate that fully developed flow is reached.

Knowing that 3 meters long body will increase the computational time while meshing and calculating the solution, nonetheless, 3 meters body is settled since time difference is tolerable and used in the main analysis. The inner pipe moves in the z-direction with a velocity of V_p = 0.001 m/s, while outer pipe is stationary. A hexahedral meshed fine grid is generated to ensure that node and element numbers exceed 4 million each. The grid numbers are optimized to ensure an accurate representation of the physics of the flow and to minimize computational time; which is called grid independence analysis and will be presented later in this chapter. Figure 6.1 shows the geometry and mesh construction in XY plane and in isometric view for dimensionless eccentricity of 0.7.

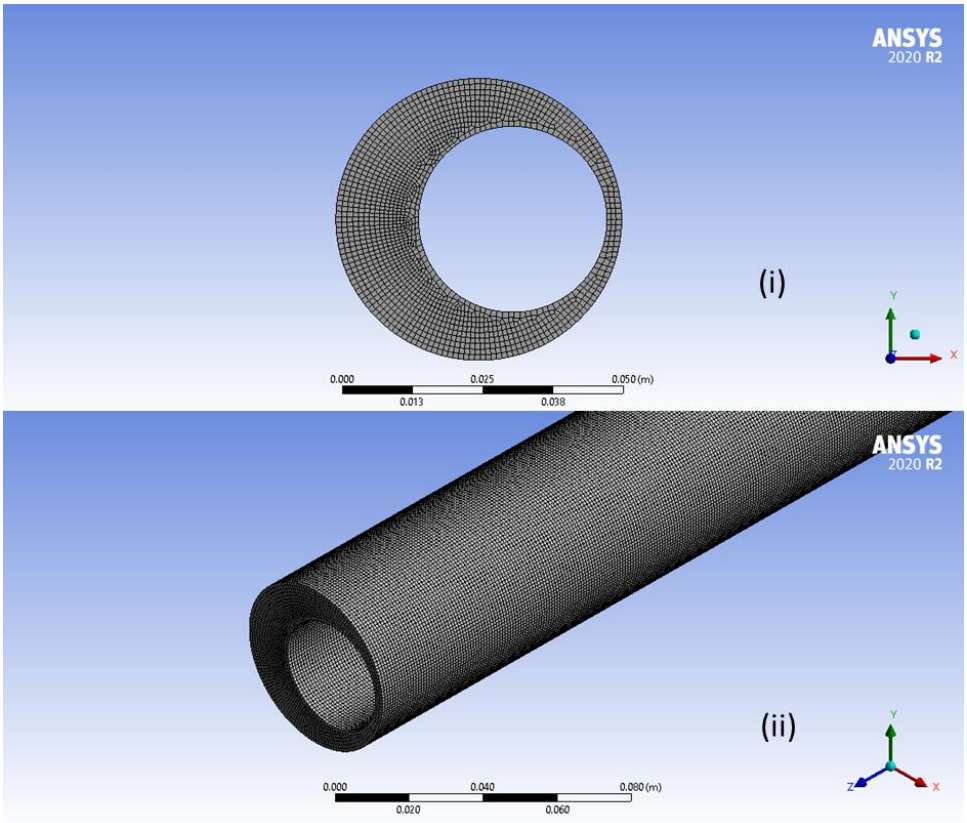

Figure 6.1 CFD Mesh with ε = 0.7 - (i) Cross-Sectional View, (ii) Isometric View

In the set-up section, the flow is characterized as viscous laminar with single phase liquid with relevant boundary conditions to simulate the surge and swab concept. The inner pipe is selected to move only in z direction with an absolute velocity; while outer pipe is selected as stationary.

A "pressure-based" solver that employs the momentum equation to calculate the velocity profile is used, while a pressure correction equation, which is derived by combining mass and momentum equations, is utilized to determine the pressure profile. The computations involved discretizing the governing momentum and mass conservation equations using finite volume method, where the flow domain was divided into a finite number of control volumes. These individual cells served as the basis for numerically integrating the governing flow equations, ultimately transforming them into a set of algebraic equations.

The Semi-Implicit Method for Pressure Linked Equations, “SIMPLE”, algorithm was used as the solution algorithm where the governing equations are solved sequentially. This algorithm is a commonly used numerical method to solve Navier-Stokes equations (Mangani and Bianchini, 2007). The momentum equation and mass conservation error are minimized to a maximum convergence of 0.0001%. Convergence was reached in all cases before 50th iteration. In both ANSYS Fluent and numerical model simulations, the velocity profiles are generated for the given pressure loss values. The same pressure loss value is inputted to both models and the velocity profiles are compared. Figure 6.2 compares velocity profile in ANSYS for $\varepsilon = 0.7$ and velocity profile for the same run from MATLAB, respectively.

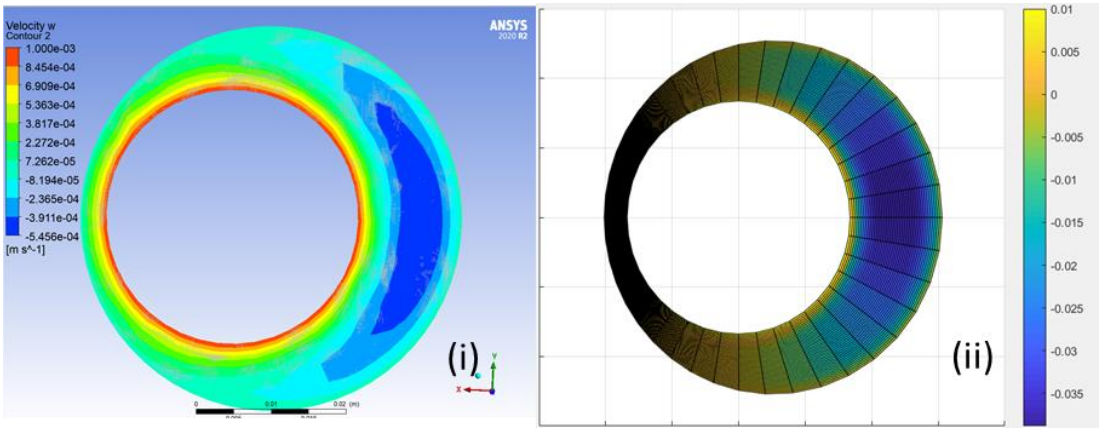

Figure 6.2 Velocity Contours ε = 0.7 and the Same Geometric and Fluid Properties (i) ANSYS Fluent, (ii) Proposed Numerical Model

Velocity profile in the annulus while surge and swab takes place obtained from ANSYS Fluent and the proposed numerical model are also compared for various eccentricities. For this comparison, two different fluids are used; water is used as a Newtonian fluid, and two different Power Law fluids are used for non-Newtonian fluid; where Power Law-1 fluid has consistency index, K, of 1.5 Pa.s and Power Law-2 fluid has K of 2.5 Pa.s and both fluids have flow behavior index, n, of 0.8.

The resultant velocity profiles are illustrated in Figure 6.3, 6.4, 6.5, and 6.6 for Newtonian fluid; where Figure 6.7 and 6.8 shows the comparison for Power Law fluids.

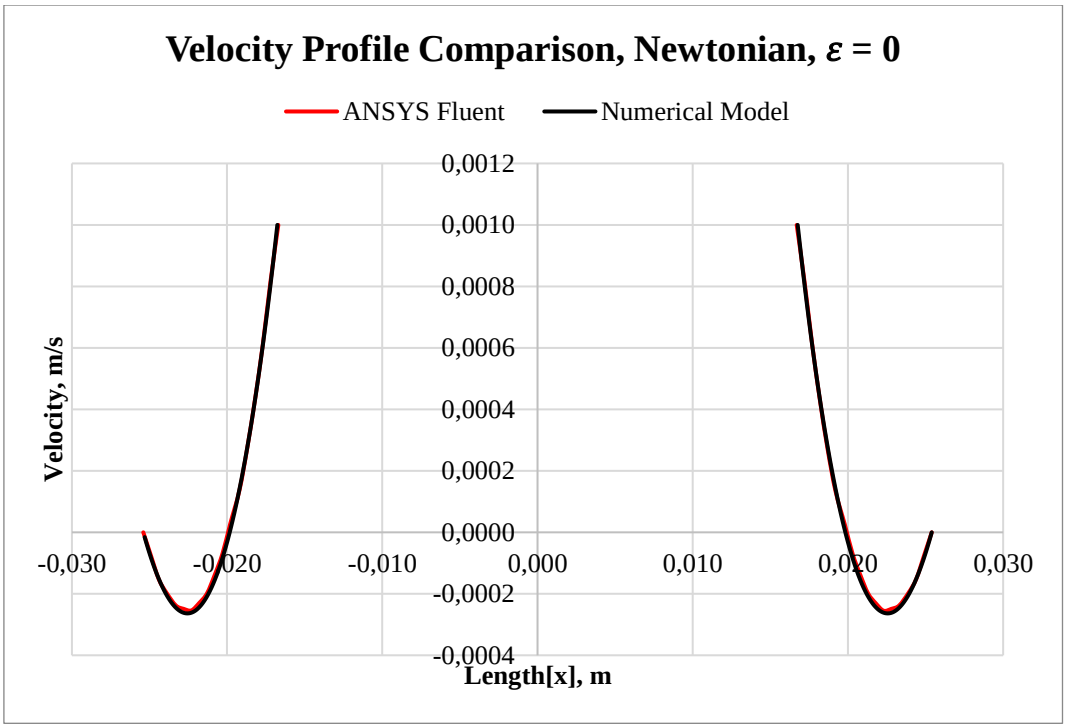

Figure 6.3 Velocity Profile Comparison between ANSYS Fluent and Numerical Model for Newtonian Fluid, ε = 0

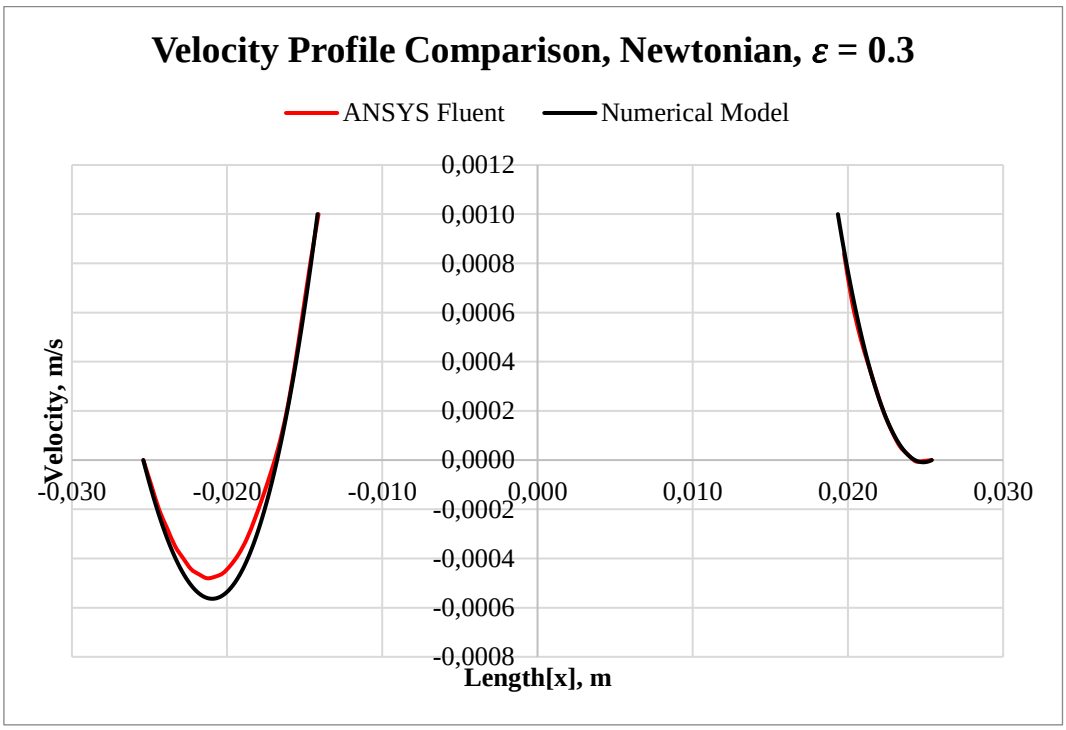

Figure 6.4 Velocity Profile Comparison between ANSYS Fluent and Numerical Model for Newtonian Fluid, ε = 0.3

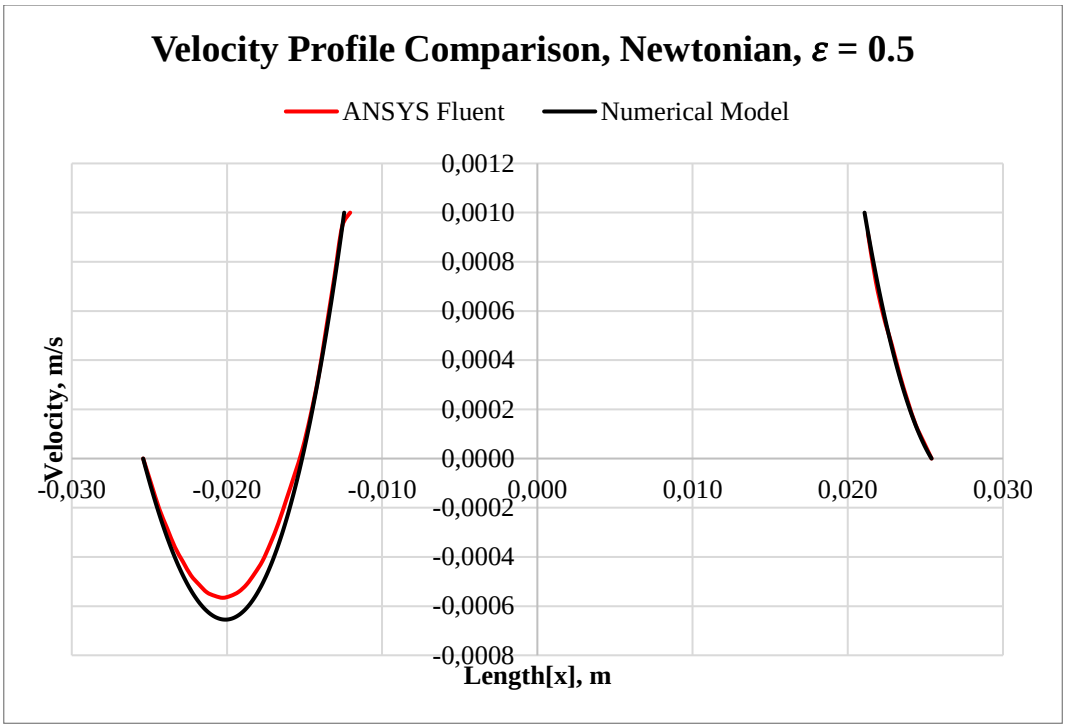

Figure 6.5 Velocity Profile Comparison between ANSYS Fluent and Numerical Model for Newtonian Fluid, ε = 0.5

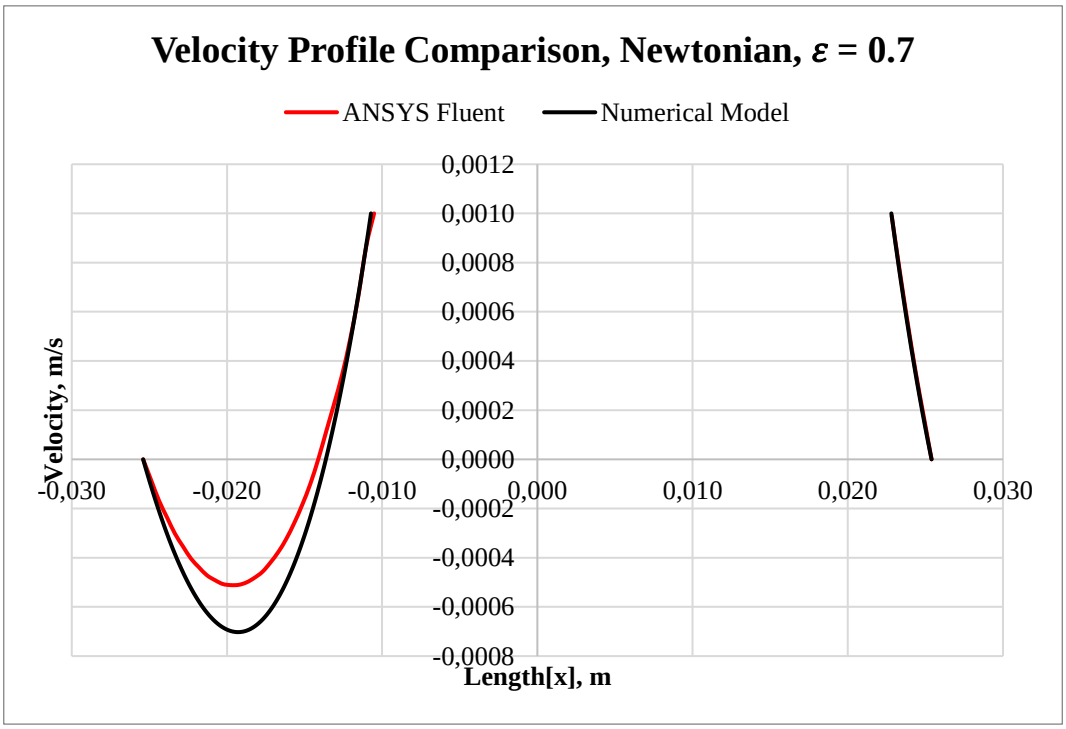

Figure 6.6 Velocity Profile Comparison between ANSYS Fluent and Numerical Model for Newtonian Fluid, ε = 0.7

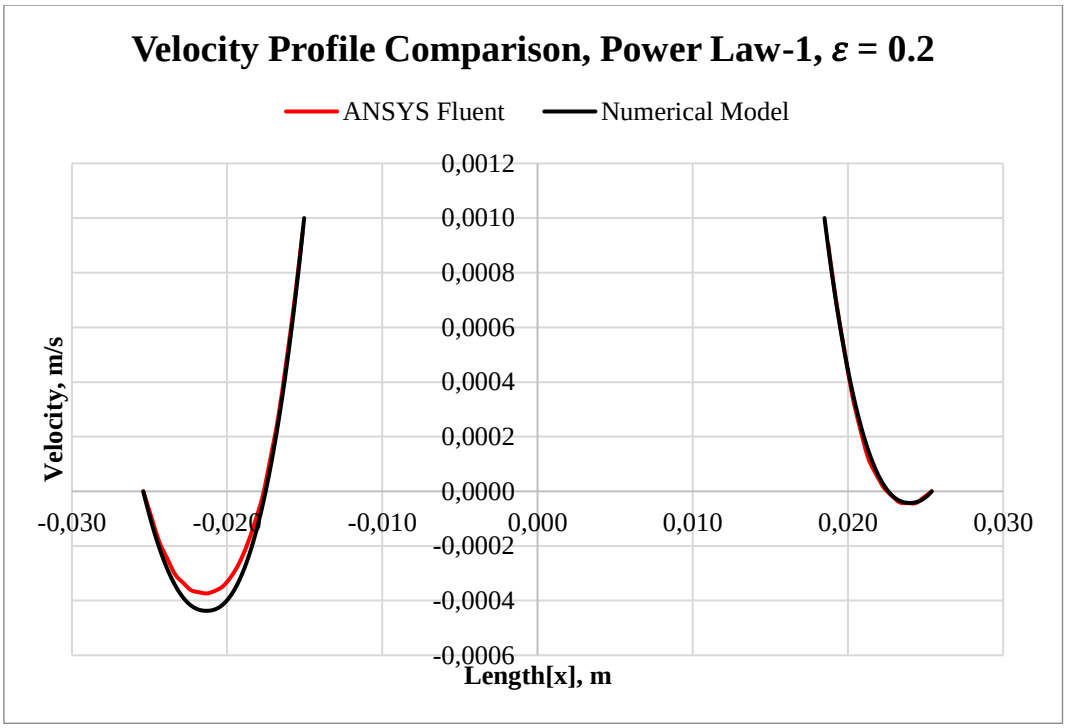

Figure 6.7 Velocity Profile Comparison between ANSYS Fluent and Numerical Model for Power Law Fluid-1, ε = 0.2

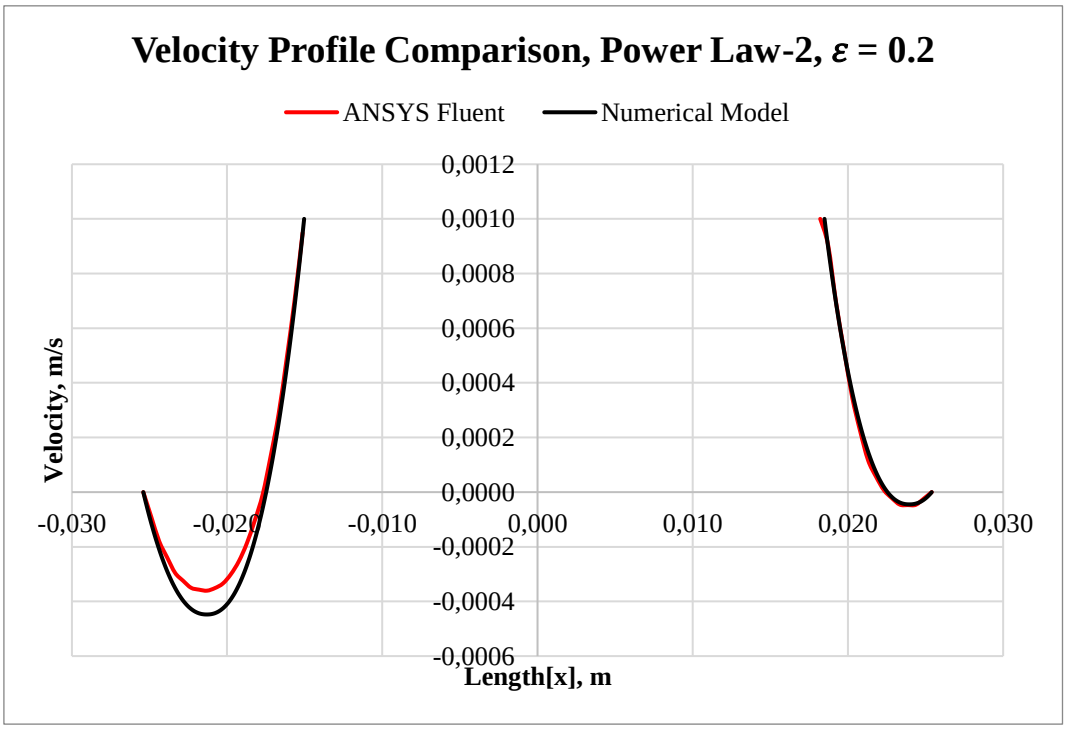

Figure 6.8 Velocity Profile Comparison between ANSYS Fluent and Numerical Model for Power Law Fluid-2, ε = 0.2

The results shown in previous figures from Figure 6.3 to Figure 6.8 for various eccentricities from concentric, $\varepsilon = 0$, to highly eccentric, $\varepsilon = 0.7$, validate the proposed numerical model in terms of physics. The comparison of velocity profiles shows a fair match between ANSYS Fluent and the proposed numerical model results. The left-hand side of the figure represents the larger annular gap where there is ~15% difference in terms of the peak velocity between the Fluent and the proposed numerical model results. This is an acceptable difference especially considering it is in terms of the velocity profile and only in a single cross section.

On the other hand, surge and swab pressure gradients resulting from ANSYS and MATLAB are compared and presented in Table 6.1. In the table, the pressure gradients of analyses presented from Figure 6.3 to Figure 6.8 are compared and average percent errors (APE); which are calculated using Eq. 6-2, are listed. As seen from table, pressure gradient results from ANSYS and MATLAB are similar and differences are below 10%, which shows a good agreement.

Table 6.1 Pressure Gradient Comparison Between ANSYS and MATLAB for Analyses Shown from Figure 6.3 to Figure 6.8

Fluid Type	$K, Pa.s^n$	n	ε	$\frac{dp}{dl}, Pa/m$ ANSYS	$\frac{dp}{dl}, Pa/m$ MATLAB	APE Between ANSYS and MATLAB
Newtonian	0.001	1.0	0	0.0680	0.0661	2.828
Newtonian	0.001	1.0	0.3	0.0605	0.0579	4.447
Newtonian	0.001	1.0	0.5	0.0497	0.0465	6.877
Newtonian	0.001	1.0	0.7	0.0403	0.0367	9.696
Power Law	1.5	0.8	0.2	125.774	118.549	6.095
Power Law	2.5	0.8	0.2	210.649	196.126	7.405

The overall difference, regarding the average velocity profile or pressure loss, is relatively small. From this analysis it is safe to conclude that the proposed numerical model performs well in capturing the physics with the given assumptions.

6.2 Grid Independence Analysis

Grid independence analysis is a good practice in CFD simulations to ensure that the solution is not affected by changes in grid size; as well as ensures the reliability and accuracy of the results (Sayindla et al., 2019). The purpose of the grid independence study is to determine the optimal grid resolution that provides consistent results without significant changes as the grid gets refined or coarsened. During the grid independence analysis, typically, the mesh sizes vary systematically while keeping other simulation settings constant. It is desirable to use the minimum number of grid elements to reduce simulation time while maintaining accuracy.

In this study, 8 different element and node sizes are employed, and the obtained velocity profiles are compared to the results from the proposed numerical model. Power Law fluid is used in this study; with flow behavior index, n = 0.8 and consistency index, K = 1.5 Pa.s; while tripping velocity is selected as V_p = 0.001 m/s. Similar setup was used as the main analysis; eccentricity is $\varepsilon = 0.2$, and radii of outer and inner cylinders are 0.0254 m and 0.016764 m, respectively, while fluid body was extruded for 3 m long in z-axis.

Mesh #1 has the fewest elements, indicating the coarsest grid, and Mesh #8 has the greatest number of elements, meaning the finest grid; while the number of elements increased from Mesh #1 to Mesh #8. Element (E) and Node (N) sizes of the different Mesh #'s are presented in Table 6.1. First raw shows the Element number; while last raw of the table represents the Node number of different Mesh #'s. Starting point for element number is around 60 thousand in Mesh #1; while maximum number of elements are in Mesh #8 with 8 million elements. Similarly, it is intended to increase node number systematically, starting from 88 thousand, up to a maximum of 8.6 million nodes.

Table 6.2 Number of Elements (E) and Nodes (N) Used in Grid Independence Study

Mesh#1	**Mesh#2**	**Mesh#3**	**Mesh#4**	**Mesh#5**	**Mesh#6**	**Mesh#7**	**Mesh#8**
E:63,580	152,541	498,817	1,128,604	2,322,784	4,027,342	4,765,280	8,080,240
N:88,382	193,612	600,184	1,298,745	2,594,144	4,424,948	5,203,006	8,695,432

Surge and swab simulations are run separately in ANSYS Fluent and resultant velocity profiles are compared with the data obtained from numerical model. Equations 6-1 and 6-2 are used to calculate Absolute Average Percent Errors (AAPE); which is used as the main parameter to indicate accuracy.

$$Error_{Absolute} = \left| \frac{v_{CFD} - v_{Numerical}}{v_{Numerical}} \; x \; 100 \right| \tag{6-1}$$

$$Absolute\ Average\ Percent\ Error = \frac{1}{n}\left(\sum_{i=1}^{n} \left(Error_{Absolute,i} \right) \right) \tag{6-2}$$

Figures between Figure 6.9 to Figure 6.16 show the velocity profile comparisons between proposed numerical model and velocities obtained from ANSYS Fluent with various mesh sizes; Mesh #1 up to Mesh #8, respectively.

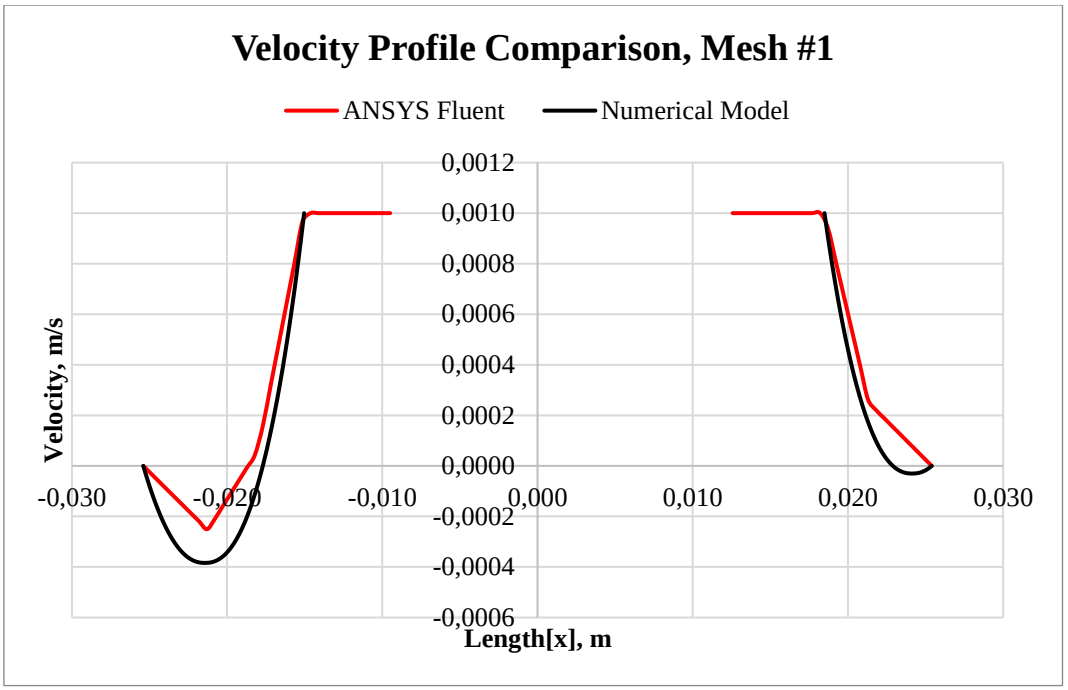

Figure 6.9 Grid Independence Analysis, Velocity Profile Comparison between Numerical Model and ANSYS Fluent for Mesh #1

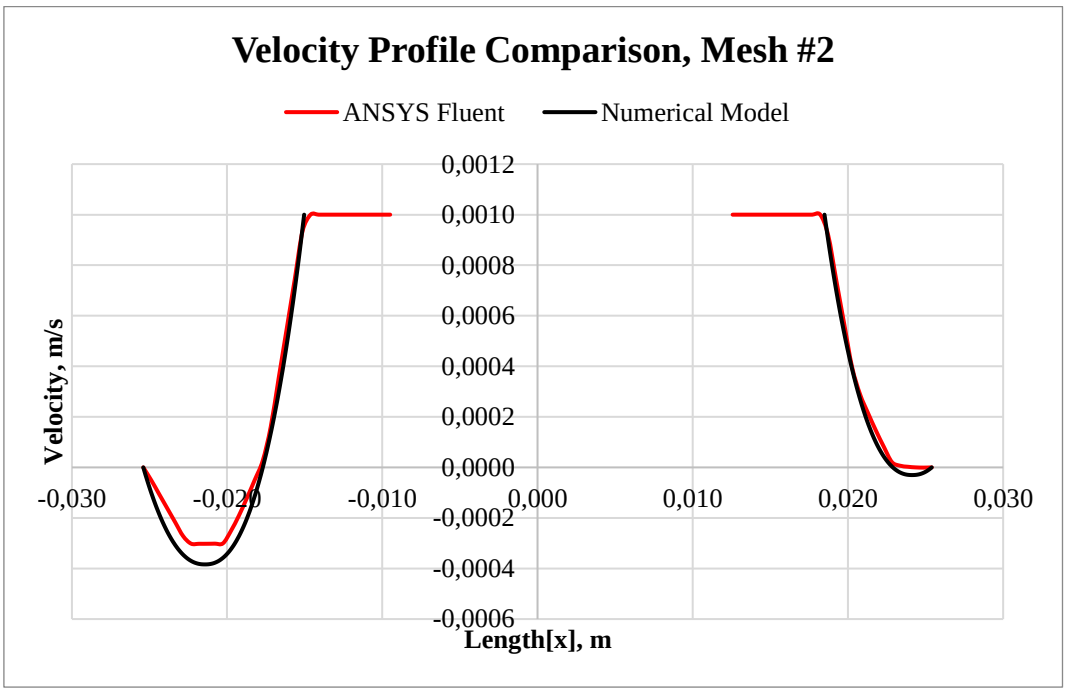

Figure 6.10 Grid Independence Analysis, Velocity Profile Comparison between Numerical Model and ANSYS Fluent for Mesh #2

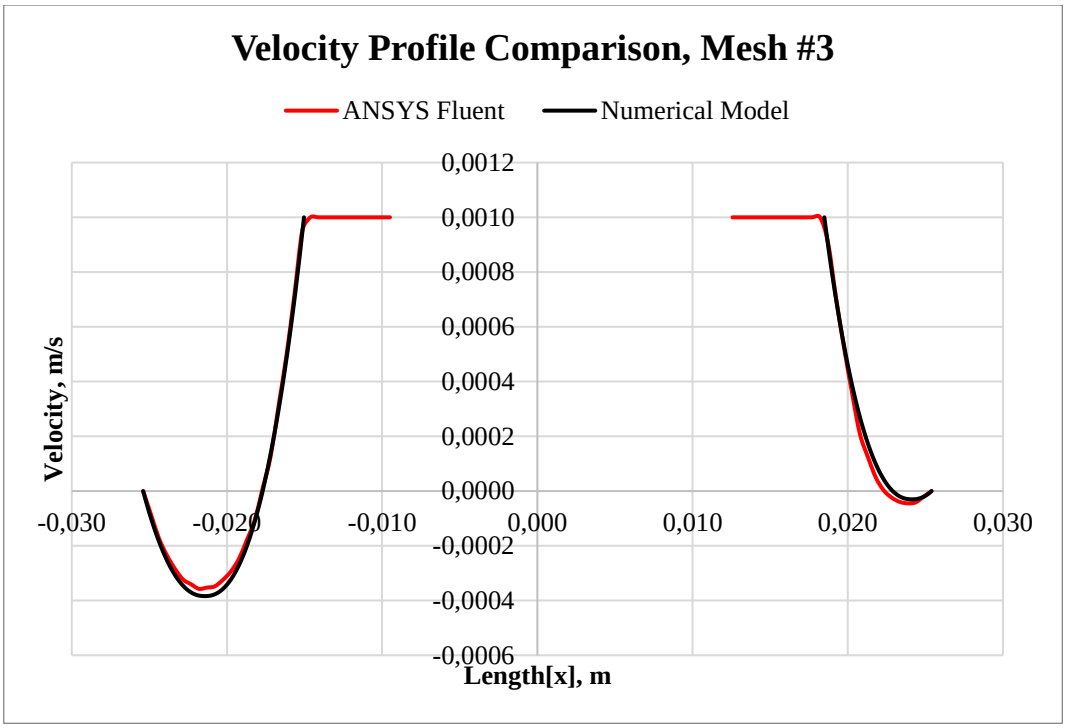

Figure 6.11 Grid Independence Analysis, Velocity Profile Comparison between Numerical Model and ANSYS Fluent for Mesh #3

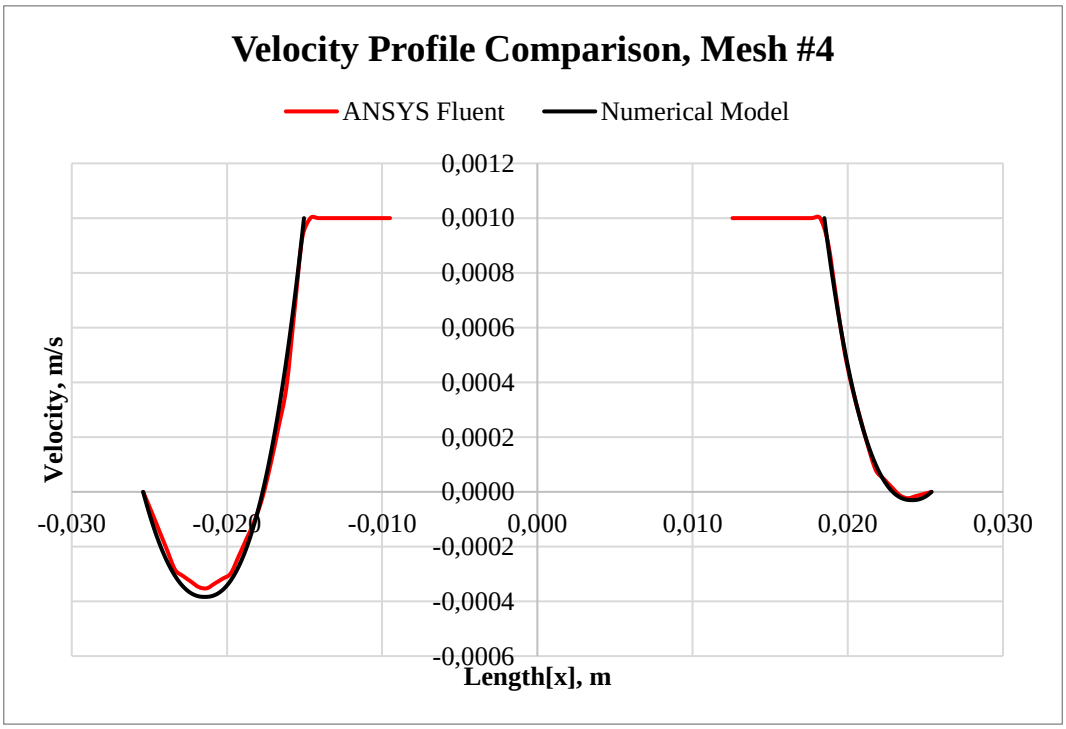

Figure 6.12 Grid Independence Analysis, Velocity Profile Comparison between Numerical Model and ANSYS Fluent for Mesh #4

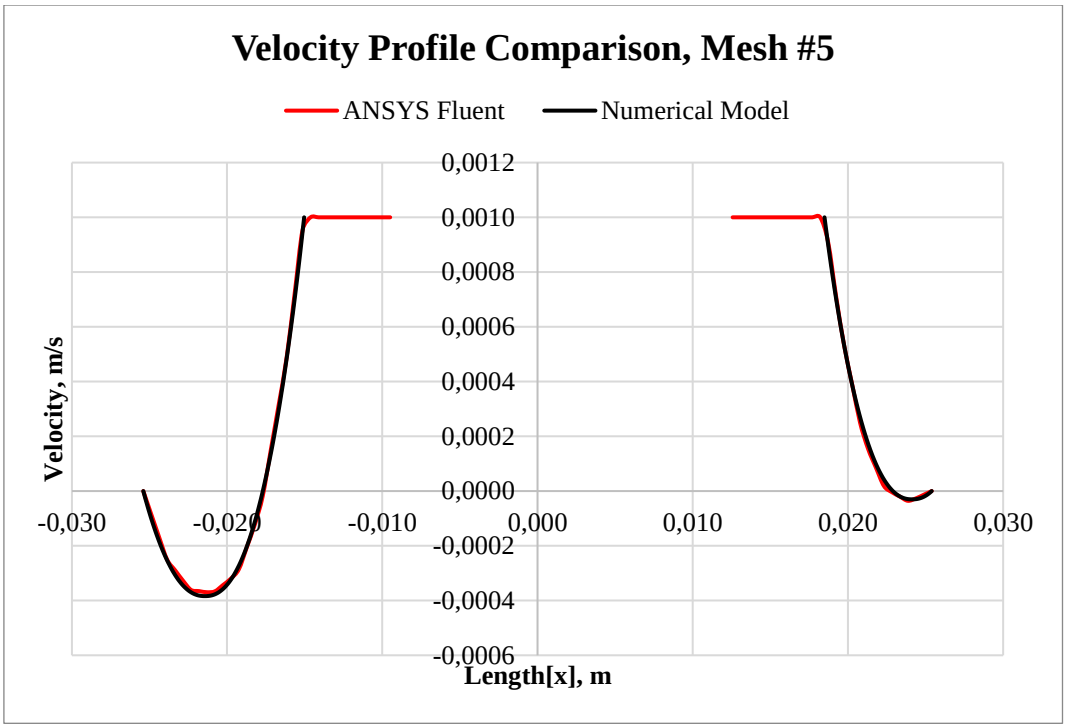

Figure 6.13 Grid Independence Analysis, Velocity Profile Comparison between Numerical Model and ANSYS Fluent for Mesh #5

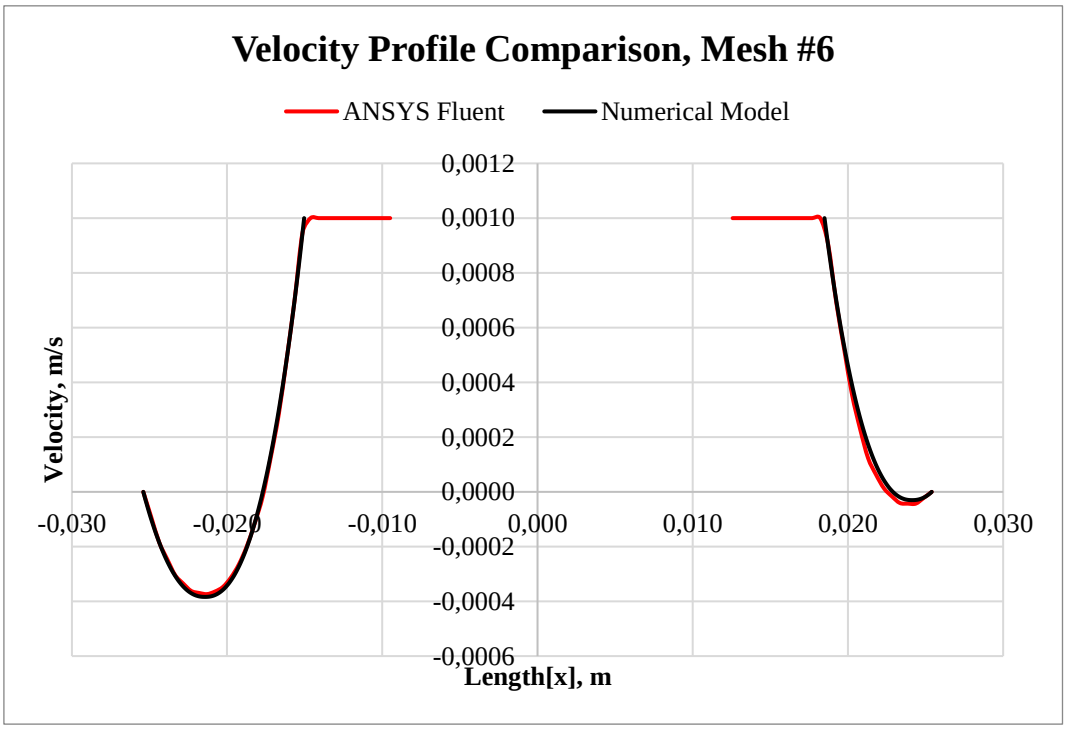

Figure 6.14 Grid Independence Analysis, Velocity Profile Comparison between Numerical Model and ANSYS Fluent for Mesh #6

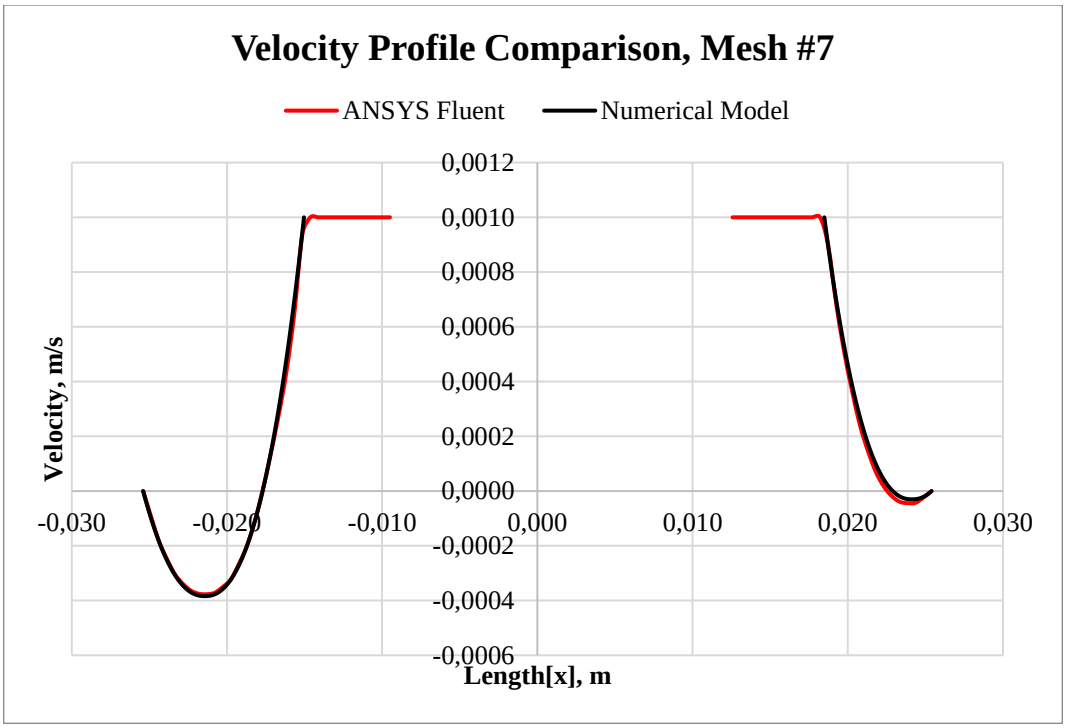

Figure 6.15 Grid Independence Analysis, Velocity Profile Comparison between Numerical Model and ANSYS Fluent for Mesh #7

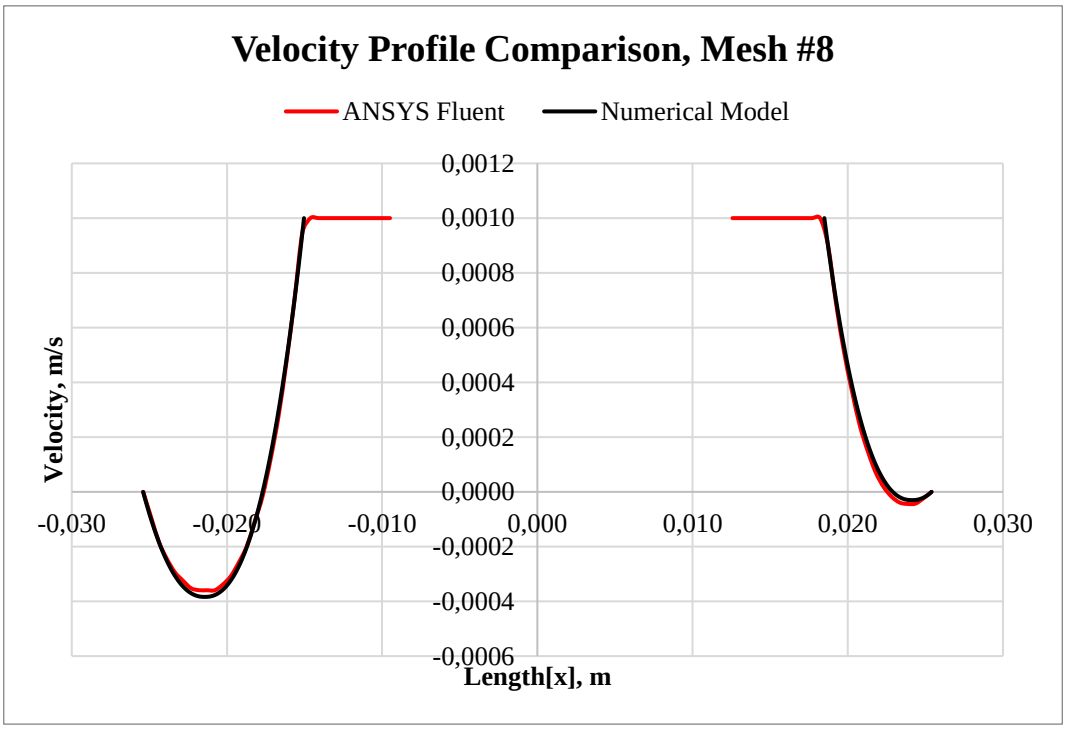

Figure 6.16 Grid Independence Analysis, Velocity Profile Comparison between Numerical Model and ANSYS Fluent for Mesh #8

Table 6.3 presents summary and error results of the grid independence analysis. Node number, element number, element size, maximum size, defeature size and curvature minimum size for each Mesh #'s are listed with their corresponding average absolute percent errors.

Table 6.3 Grid Independence Analysis Results: Statistical Metrics and Errors

	Node #	Element #	Element Size, m	Max Size, m	Defeature Size, m	Curvature MinSize, m	AAPE
Mesh#1	88,382	63,580	4.0E-03	8.0E-03	2.0E-05	4.0E-05	299.31
Mesh#2	193,612	152,541	3.0E-03	6.0E-03	1.5E-05	3.0E-05	56.56
Mesh#3	600,184	498,817	2.0E-03	4.0E-03	1.0E-05	2.0E-05	48.08
Mesh#4	1,298,745	1,128,604	1.5E-03	3.0E-03	7.5E-06	1.5E-05	31.39
Mesh#5	2,594,144	2,322,784	1.2E-03	2.4E-03	6.0E-06	1.2E-05	17.89
Mesh#6	**4,424,948**	**4,027,342**	**1.0E-03**	**2.0E-03**	**5.0E-06**	**1.0E-05**	**15.44**
Mesh#7	5,203,006	4,765,280	9.5E-04	1.9E-03	4.7E-06	9.5E-06	19.29
Mesh#8	8,695,432	8,080,240	8.0E-04	1.6E-03	4.0E-06	8.0E-06	17.64

Table 6.3 and figures from Figure 6.9 to Figure 6.16 show that increasing the element and node number increases the accuracy of the CFD analysis. For example, Mesh #1 has AAPE of 299%, while Mesh #8 has AAPE of 17%. Mesh #6 which has around 4 million node and elements would result in a fairly low AAPE; around 15%; which could be regarded as acceptable. It is important to note the error originates to the velocity in a cross section, and that surge and swab pressure difference that would result with that error would be much lower than 15% as can be seen from sensitivity analysis. On the other hand, a coarser mesh than that would yield erroneous velocities, hence pressure losses. Similarly, finer mesh size than Mesh #6 has similar AAPEs; however, it requires much more time to finish computation. Therefore, Mesh #6 is chosen as the optimum grid size for this particular flow simulation. Overall, it is safe to say that confidence is established in the simulation results by conducting grid independence study.

CHAPTER 7

COMPARISONS WITH EXPERIMENTAL DATA AND EXISTING MODELS

Proposed numerical model is further validated with experimental data and other existing models from literature for eccentric annulus. Since proposed model reduces to concentric annulus when the input of eccentricity is zero; $\varepsilon = 0$; validation of proposed model is presented in two sections; validations with concentric annulus and eccentric annulus. Details of the studies that are used in the comparative analysis are given in Table 7.1 below:

Table 7.1 List of Studies Used in Comparative Analysis

Researchers	Annulus Type	Solution Type	Comments
He et al. (2016)	Concentric	Numerical Model & Regression Analysis	Presented result as pressure gradient. Validated via models in Burkhardt (1961) and in Crespo et al. (2012).
Crespo and Ahmed (2013)	Concentric	Narrow Slot Approximation & Regression Analysis	Validated via experimental study they have conducted and models in Bourgoyne et al. (1966) and in Schuh (1964).
Tang et al. (2016)	Fully Eccentric	Numerical Model	Validated via experimental study and CFD analysis they have conducted.
Belimane et al. (2021)	Eccentric	Numerical Model using Curvilinear Coordinates	Validated via CFD analysis, experimental study in Tang et al. (2016) and models from Haciislamoglu and Langlinais (1990), and Tang et al. (2016).
Haciislamoglu and Laglinais (1990)	Eccentric	Numerical Model using Bipolar Coordinates	Presented velocity and viscosity profiles and developed a correlation to account for pressure losses of PL fluids in eccentric annulus.

7.1 Comparison and Validation for Concentric Annulus

In this chapter, two different models and an experimental study and a comparative study are presented.

Crespo and Ahmed (2013) conducted an investigation on steady-state laminar flow analysis of surge and swab pressures in concentric annuli using the narrow-slot approximation for Yield Power Law fluids. They also conducted laboratory experiments to study the effects of drilling fluid properties, tripping speed, and annular geometry on surge and swab pressures, comparing both Newtonian and non-Newtonian fluids. To validate their model, the authors compared their findings with experimental data and existing models from the works of Bourgoyne et al. (1991) and Schuh (1964) in the literature. The results demonstrated that the authors' correlation aligns well with the experimental study and existing models.

Figure 7.1 presents the surge and swab pressure gradient comparison with proposed numerical study and the experimental study carried out in a concentric annulus with two different yield power law fluids for surge and swab analysis while varying pipe velocity as presented in Crespo and Ahmed (2013). Input parameters for this study are given in Table 7.2.

Table 7.2 Input Parameters for Experimental Study Conducted in Crespo and Ahmed (2013)

	n	$K, Pa.s^n$	τ_y, Pa	R_o, m	R_i, m	ε
Fluid-1 0.67% XG	0.50	0.553	7.8	0.0254	0.016764	0
Fluid-2 0.44% XG	0.52	0.359	3.44	0.0254	0.016764	0

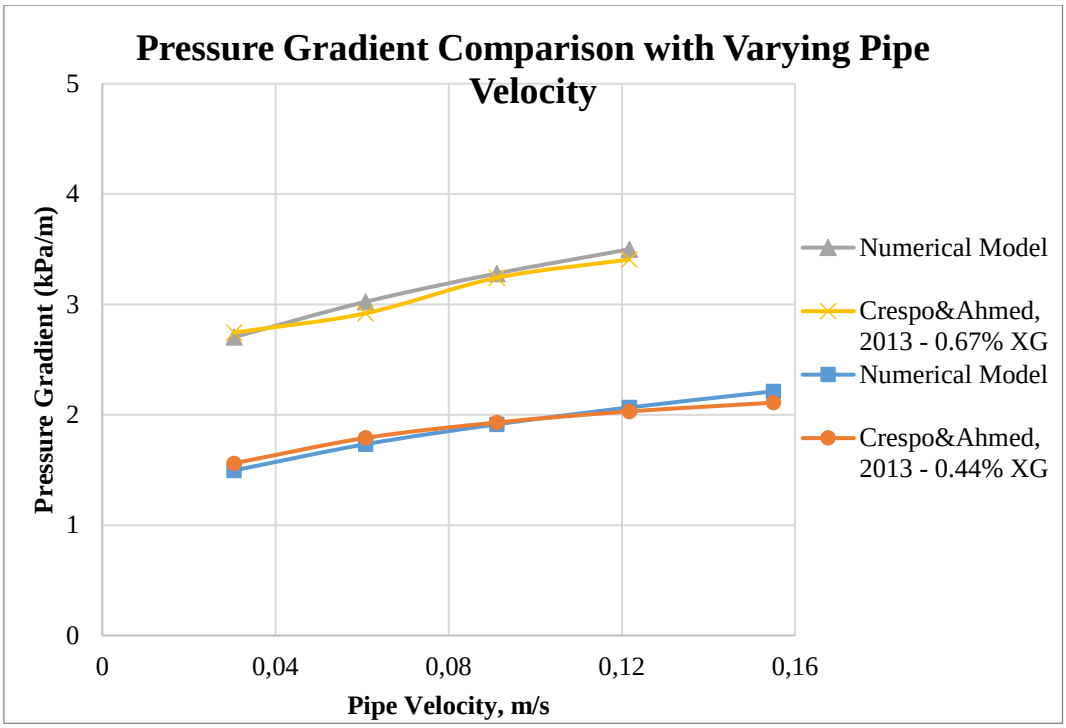

Figure 7.1 Surge and Swab Pressure Gradient Comparison – Experimental Study with Two Different YPL Fluids in Concentric Annulus for Varying Pipe Velocity

Comparison of proposed model with another study conducted by the same authors is presented in Figure 7.2 and 7.3. In Figure 7.2, the results of mathematical model conducted by Crespo and Ahmed (2013) with different yield stress YPL fluids and by varying pipe velocity are compared with the proposed numerical model. In Figure 7.3, their model results with different pipe velocity cases by varying diameter ratios are presented and compared with the proposed numerical model.

The inputs of these two cases are listed in Table 7.3.

Table 7.3 Input Parameters for Mathematical Model Conducted in Crespo and Ahmed (2013)

	$V_p, m/s$	n	$K, Pa.s^n$	τ_y, Pa	R_o, m	R_i, m	ε
Fig. 7.2	-	0.5	0.6	-	0.136	0.068	0
Fig. 7.3	-	0.5	0.6	9	-	-	0

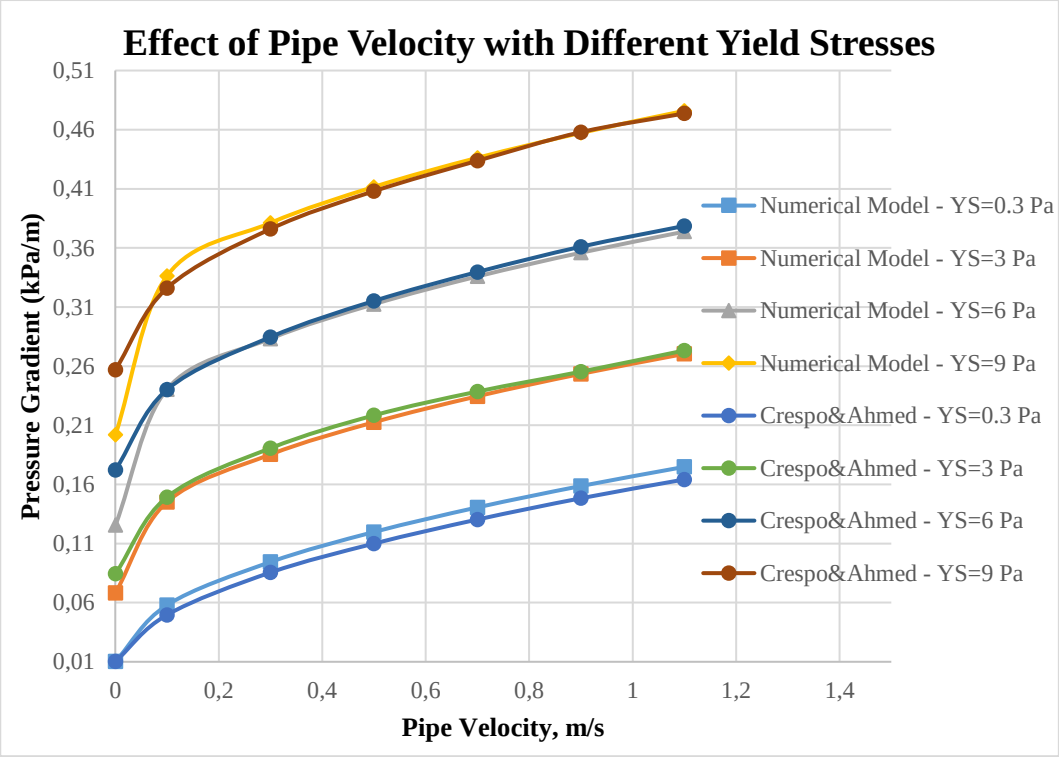

Figure 7.2 Surge and Swab Pressure Gradient Comparison – Model Results with Different Yield Stress YPL Fluids in Concentric Annulus for Varying Pipe Velocity

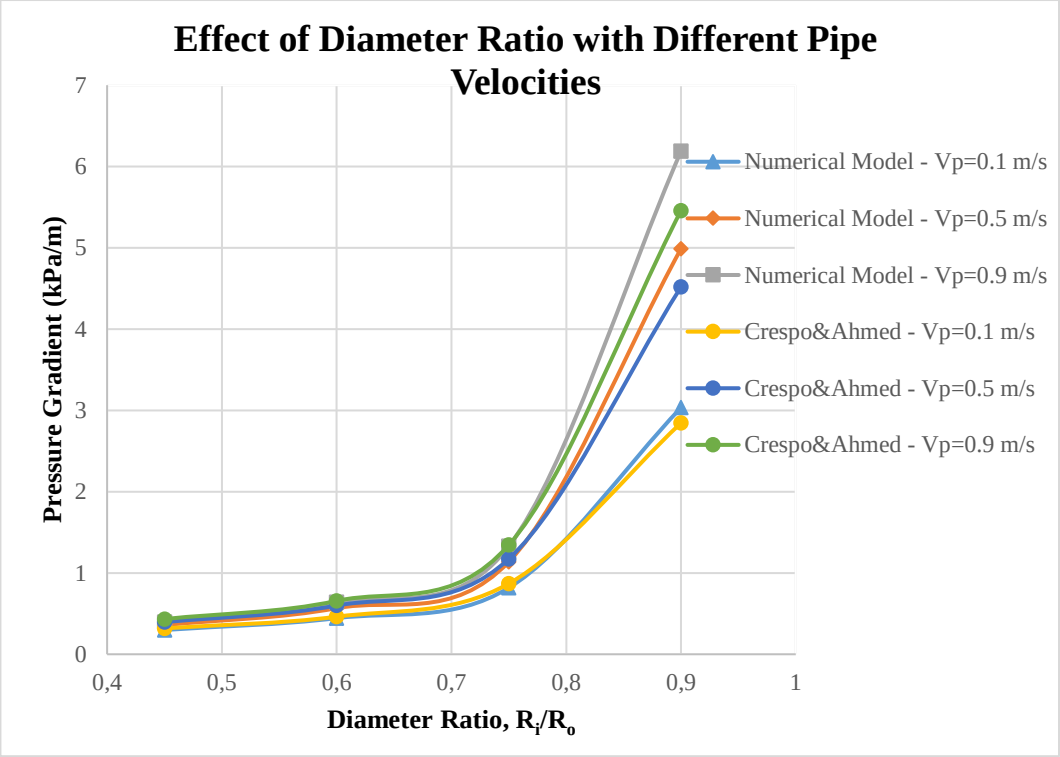

Figure 7.3 Surge and Swab Pressure Gradient Comparison – Model Results with Different Pipe Velocities in Concentric Annulus for Varying Diameter Ratio

As seen from Figures 7.1, 7.2 and 7.3, proposed numerical model is in very good accordance with the experimental study and model presented in Crespo and Ahmed (2013) for the concentric annulus.

Another comparative study for concentric annulus made with the study carried out by He et al. (2016). They have conducted a mathematical study to predict surge and swab pressures of YPL fluids in concentric annulus. The validity of their work was established through the validation process, which involved comparing their results with field data and existing models proposed by Burkhardt (1961) and Crespo et al. (2012). The validation process revealed errors within the range of 0-25%. Additionally, He et al. (2016) conducted a parametric study to examine the influence of various input parameters on the resulting pressure gradient while surge and swab takes place.

The input parameters for their parametric study are listed in Table 7.4. These base inputs were used for comparison unless stated otherwise.

Table 7.4 Input Parameters for Mathematical Model Conducted in He et al. (2016)

$V_p, m/s$	n	$K, Pa.s^n$	τ_y, Pa	R_o, m	R_i, m	ε
1.0	0.5	2.0	10.0	0.108	0.064	0

Figures from Figure 7.4 to 7.8 illustrate the effect of different parameters on the resulting surge and swab pressures; i.e., the effects of flow behavior index of the drilling fluid, radius of pipe, pipe velocity, yield stress of the fluid and consistency index of the drilling fluid.

The comparison between the proposed numerical model and the model presented in He et al. (2016) reveals a high level of agreement, as evident in Figures 7.4 to 7.8.

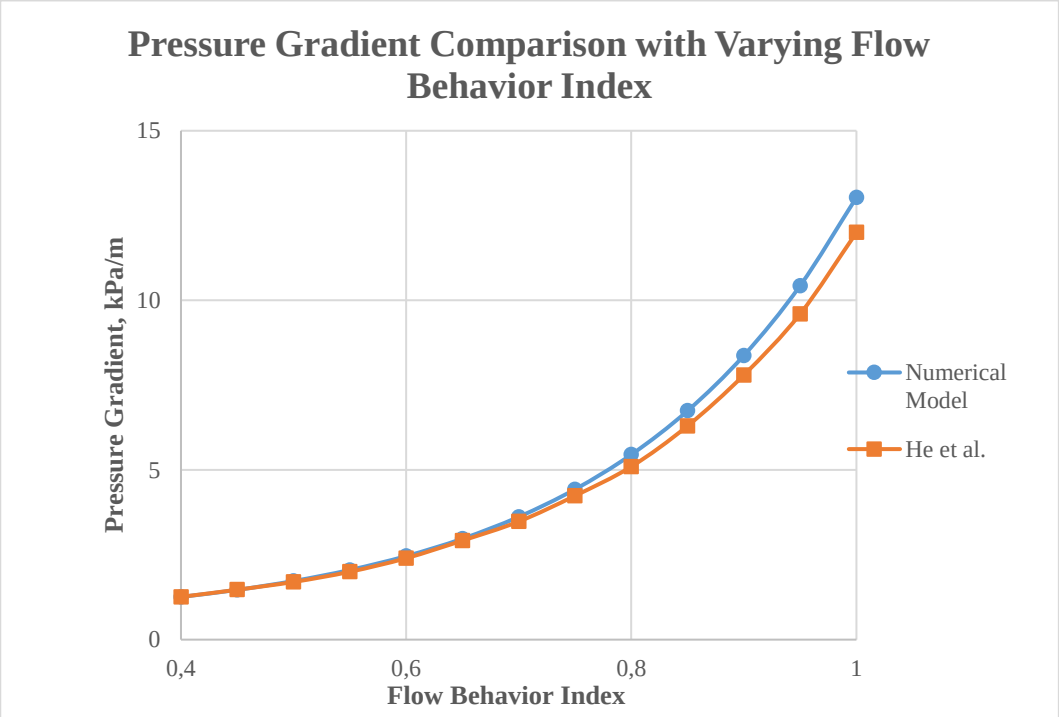

Figure 7.4 Surge and Swab Pressure Gradient Comparison – Model Results for YPL fluid in Concentric Annulus for Varying Flow Behavior Index

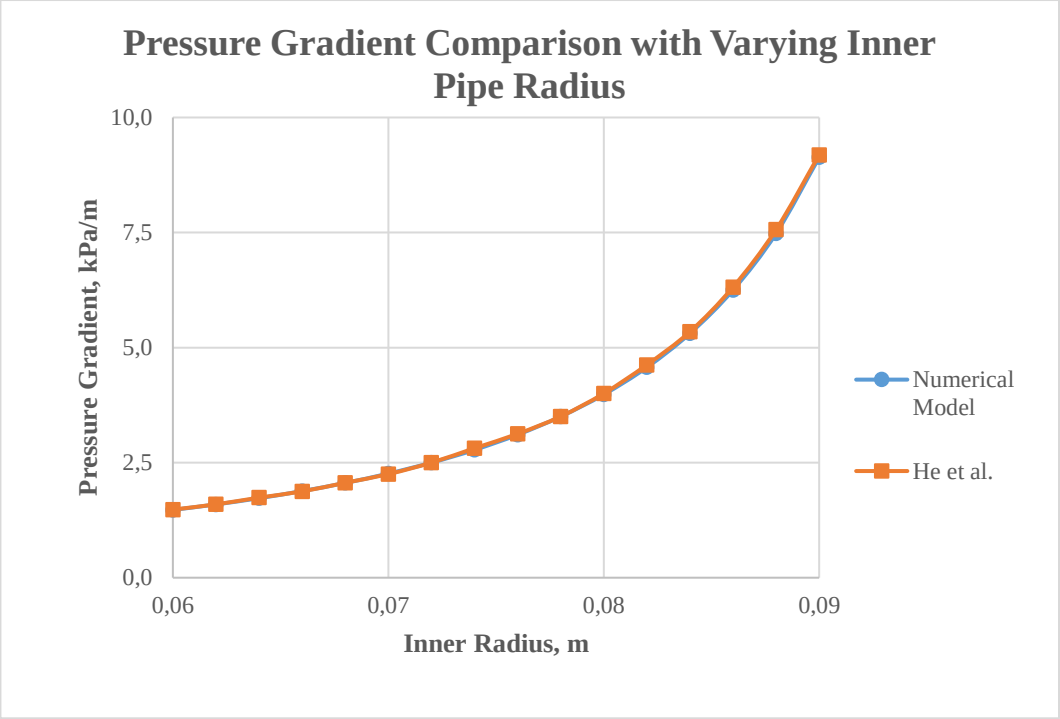

Figure 7.5 Surge and Swab Pressure Gradient Comparison – Model Results for YPL fluid in Concentric Annulus for Varying Inner Pipe Radius

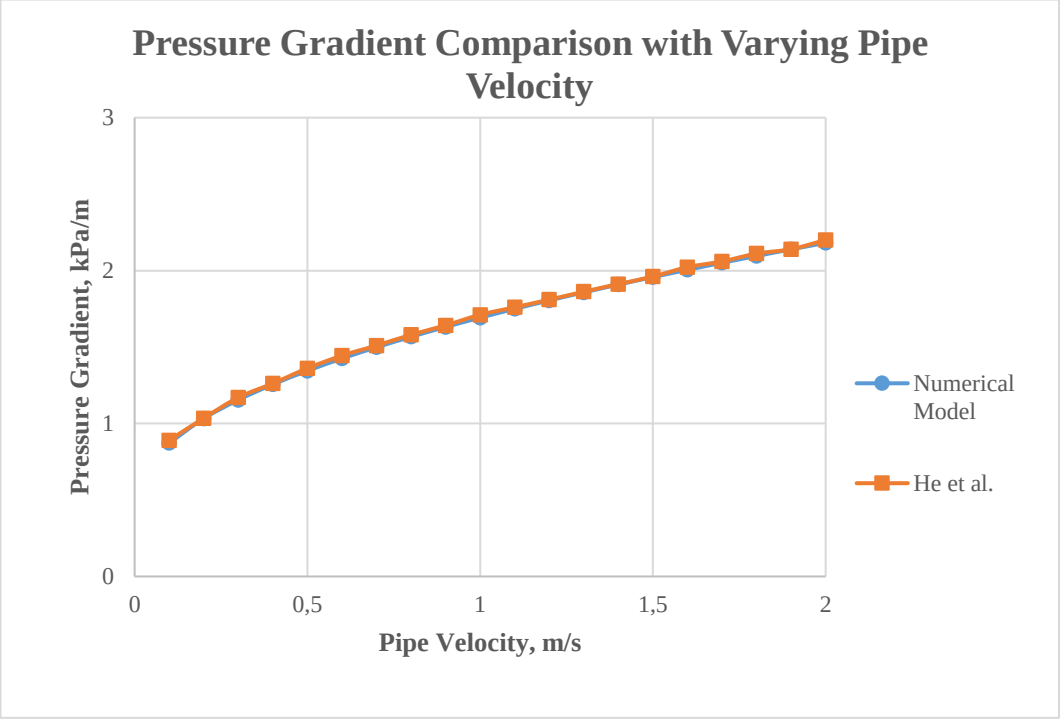

Figure 7.6 Surge and Swab Pressure Gradient Comparison – Model Results for YPL fluid in Concentric Annulus for Varying Pipe Velocity

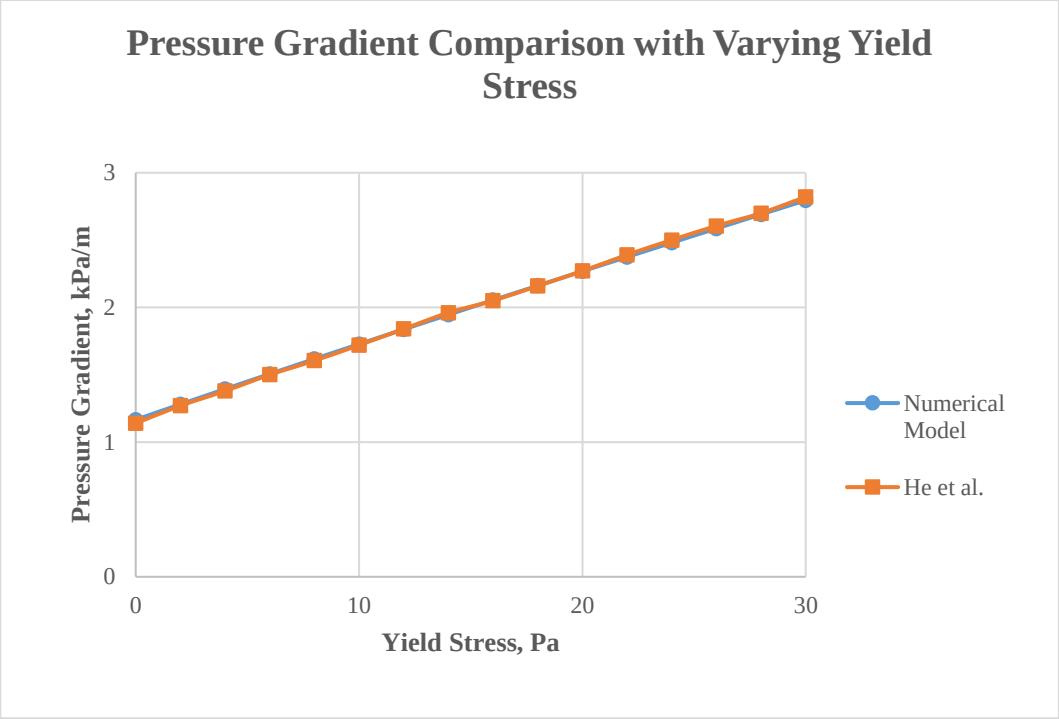

Figure 7.7 Surge and Swab Pressure Gradient Comparison – Model Results for YPL fluid in Concentric Annulus for Varying Fluid Yield Stress

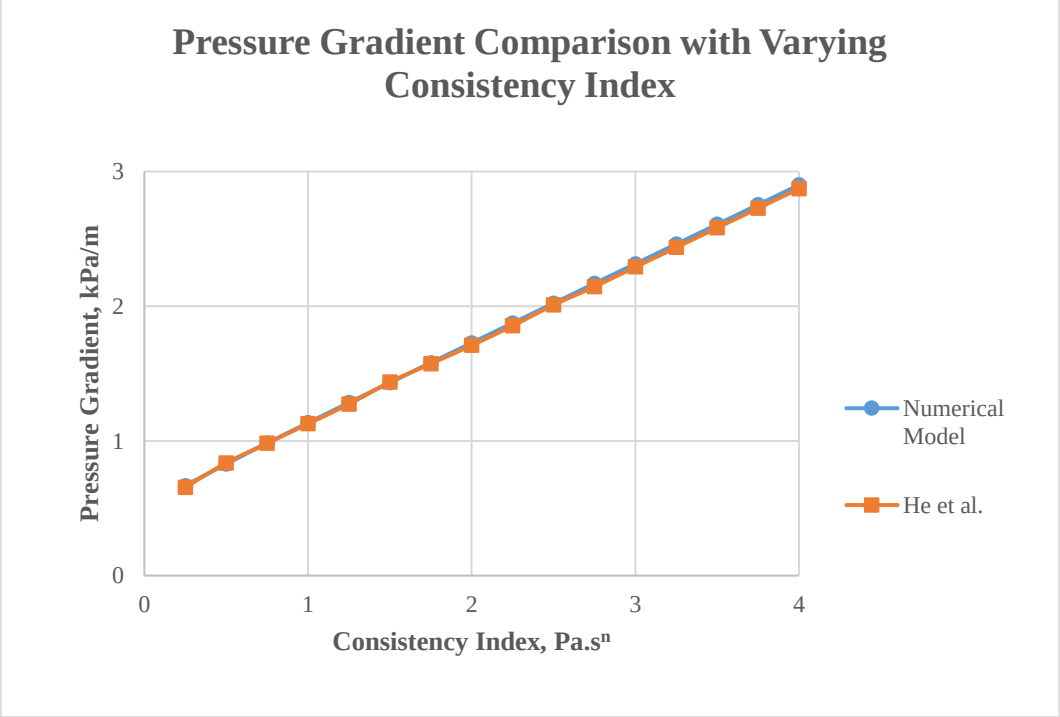

Figure 7.8 Surge and Swab Pressure Gradient Comparison – Model Results for YPL fluid in Concentric Annulus for Varying Fluid Consistency Index

7.2 Comparison and Validation for Eccentric Annulus

Comparative study and validation of the proposed model with experimental studies and other models from existing literature is carried out for eccentric annuli.

Tang et al. (2016) presented a model and conducted an experimental study and CFD study to predict surge pressure of YPL fluids in eccentric annuli. They used a similar experimental set-up that was used in Crespo and Ahmed (2013), with modification of eccentric pipe concept with eccentricity of 0.9. Authors used different fluid types and validated their model with CFD and experimental data. Here, the results with eccentric annuli will be compared with the proposed model.

Figure 7.9 shows comparison between the experiment carried out in Tang et al. (2016) and proposed numerical model. It accounts for the surge pressure gradient with different pipe velocity for three different fluids conducted in eccentricity of 0.9.

Input parameters for this experimental study is given in Table 7.5 below:

Table 7.5 Input Parameters for Experimental Study Conducted in Tang et al. (2016)

	n	$K, Pa.s^n$	τ_y, Pa	R_o, m	R_i, m	ε
Fluid-1 1.0% XG	0.394	1.96	12.895	0.0254	0.016764	0.9
Fluid-2 0.75% XG	0.337	2.105	7.345	0.0254	0.016764	0.9
Fluid-3 0.5% XG	0.373	1.054	3.474	0.0254	0.016764	0.9

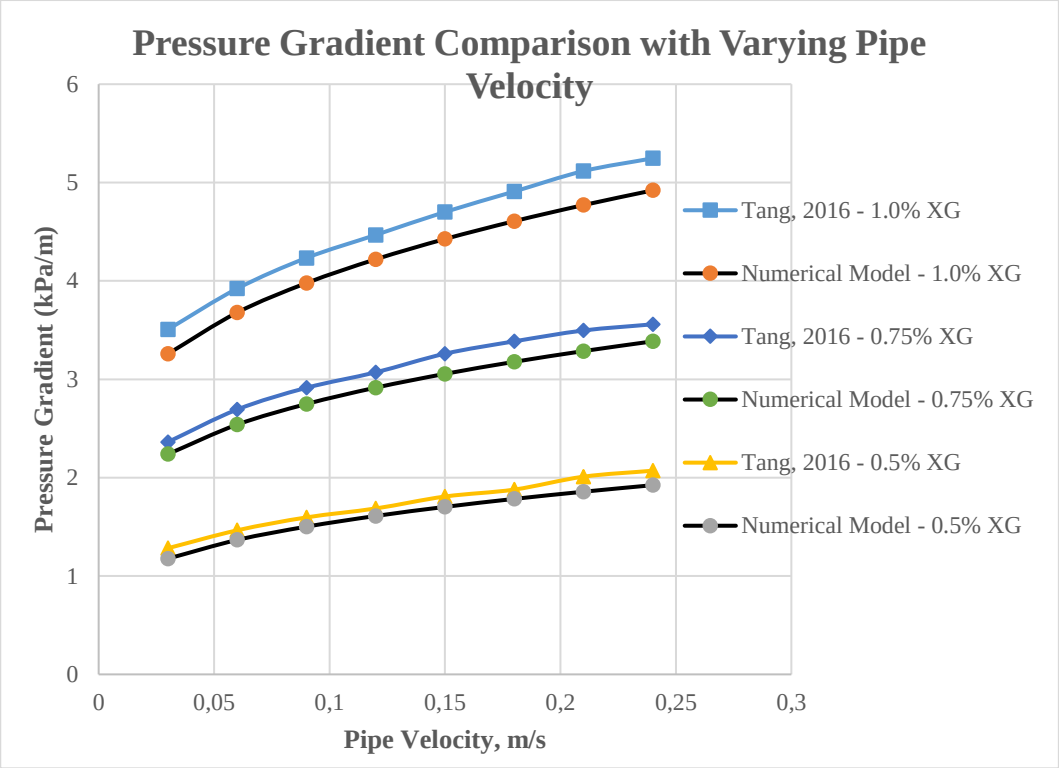

Figure 7.9 Surge and Swab Pressure Gradient Comparison – Experimental Study with Three Different YPL Fluids in Eccentric Annulus for Varying Pipe Velocity

The comparison shows good agreement for almost fully eccentric annulus of $\varepsilon = 0.9$. In order to reveal the accuracy of proposed numerical model; average absolute percent errors, AAPEs, are calcualted and presented, similar to previous comparative studies. Equations for calculation of AAPE is given in Eq. 7-1 and Eq. 7-2 below.

$$Error_{Absolute} = \left| \frac{dp/dl_{Model\ from\ Lit.} - dp/dl_{Proposed\ Model}}{dp/dl_{Proposed\ Model}}\ x\ 100 \right| \tag{7-1}$$

$$Absolute\ Average\ Percent\ Error = \frac{1}{n}\left(\sum_{i=1}^{n}\left(Error_{Absolute,i}\right)\right) \tag{7-2}$$

Calculations reveal that AAPE for the comparison with Fluid-1, 1.0% XG, is 6.2%, AAPE for the comparison with Fluid-2, 0.75% XG, is 5.6%, and the AAPE for comparison with Fluid-3, 0.5% XG, is 6.3%. Mean AAPE stays below 6% when considering all three YPL fluids, with minimum AAPE and maximum AAPE are 5.1% and 8.2%, respectively.

The obtained AAPE values indicated a high level of agreement between the model predictions and the experimental data. With a minimum AAPE of 5.1%, a maximum AAPE of 8.2%, and a mean AAPE of 6.0%, the model demonstrated consistent and accurate performance. The relatively small range between the minimum and maximum AAPE values further reinforces the reliability of the model's predictions. Detailed surge and swab pressure inputs, outputs and AAPEs for this comparative study with experimental work are presented from Table B.1 to Table B.3 in Appendix B.

Another comparative study is conducted with the work of Belimane et al. (2021). Belimane et al. (2021) developed a numerical model for surge pressure prediction of YPL fluids in eccentric annulus. They have validated their model with CFD, experimental data taken from Tang et al. (2016) and Crespo and Ahmed (2013), numerical models from same authors and from Haciislamoglu and Langlinais (1990) and presented a parametric study. Input parameters for this parametric study is given in Table 7.6 below:

Table 7.6 Input Parameters for Parametric Study Conducted in Belimane et al. (2021)

	n	$K, Pa.s^n$	τ_y, Pa	R_o, m	R_i, m	ε
Inputs	0.7	1.7	10	0.1	0.06	0.2-0.4-0.6

Figure 7.10 shows comparison of the results of the parametric study with the proposed numerical model results for different pipe velocities and different eccentricities ranging from 0.2 to 0.6. The comparison with this model yields average absolute percent errors (AAPE) of 13% for ε=0.6, 9% for ε=0.4, and 2% for ε=0.2

when discarding values at very low pipe velocities. Detailed surge and swab pressure inputs, outputs and AAPEs for the comparative study are presented in Table B.4, Table B.5 and Table B.6 in Appendix B.

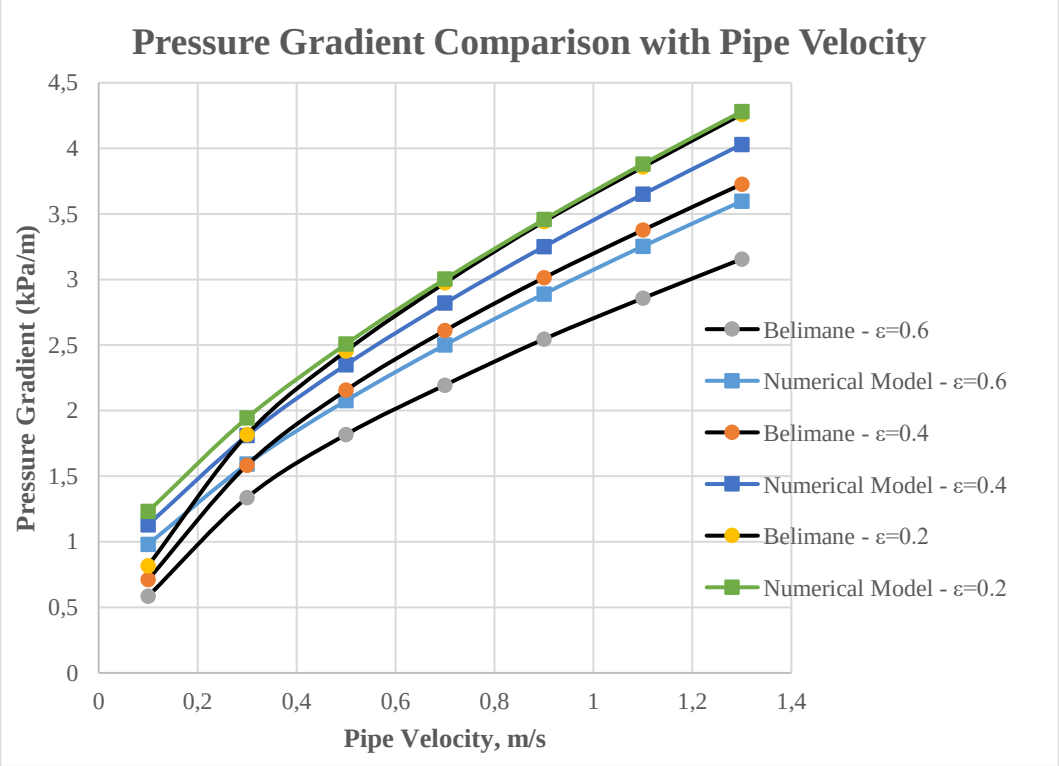

Figure 7.10 Surge and Swab Pressure Gradient Comparison – Model Results for YPL fluid in Eccentric Annulus with Different Eccentricities for Varying Pipe Velocity

Another comparative study is carried out and presented with same authors with previous study, Belimane et al. (2021). They also presented a comparison study with their model, experiments conducted by Tang et al. (2016), numerical model from Haciislamoglu and Langlinais (1990) and numerical model from Tang et al. (2016). They have investigated the resulting surge pressure gradient with varying pipe velocity for three different YPL fluids, namely HB-1, HB-2, and HB-3, for highly eccentric annulus, $\varepsilon = 0.9$. Inputs of this analysis are given in Table 7.7 below:

Table 7.7 Input Parameters for Comparative Study Conducted in Belimane et al. (2021)

	n	$K, Pa.s^n$	τ_y, Pa	R_o, m	R_i, m	ε
Fluid-1 – HB-1	0.38	2.14	11.27	0.0254	0.016764	0.9
Fluid-2 – HB-2	0.35	1.83	7.28	0.0254	0.016764	0.9
Fluid-3 – HB-3	0.39	0.88	3.41	0.0254	0.016764	0.9

Following figures show the comparison among these models and experiments with proposed model for three different fluid types. As can be seen from Figure 7.11, Figure 7.12 and Figure 7.13, the proposed numerical model demonstrates a good level of agreement with other models and experiments.

In order to quantitatively show the level of fitness of proposed numerical model with others from existing literature, AAPEs are calculated similar to previous comparative studies in this chapter. Table 7.8, Table 7.9, and Table 7.10 list the inputs and AAPEs. Detailed input and output dataset are given in Appendix B from Table B.7 to Table B.9.

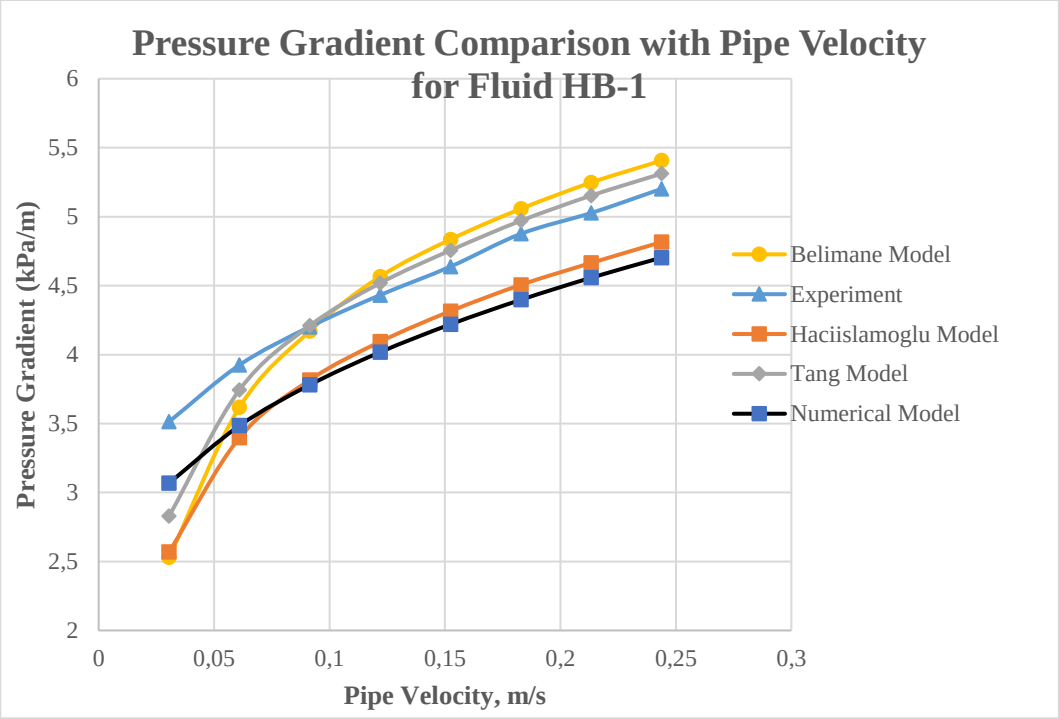

Figure 7.11 Surge and Swab Pressure Gradient Comparison – Model and Experiment Results for HB-1 Fluid in Eccentric Annulus for Varying Pipe Velocity

Table 7.8 AAPEs for Comparative Study for HB-1 Fluid

$V_p, m/s$	AAPE-Experimental Study	AAPE-Model in Belimane	AAPE-Model in Tang	AAPE-Model in Haciislamoglu
0.0304	12.68	21.31	8.47	19.45
0.0609	11.20	3.66	6.91	2.59
0.0914	10.03	9.35	10.20	0.93
0.1219	9.34	12.00	11.08	1.84
0.1523	9.02	12.72	11.28	2.21
0.1828	9.81	13.04	11.53	2.40
0.2133	9.33	13.14	11.55	2.29
0.2438	9.59	13.01	11.46	2.34

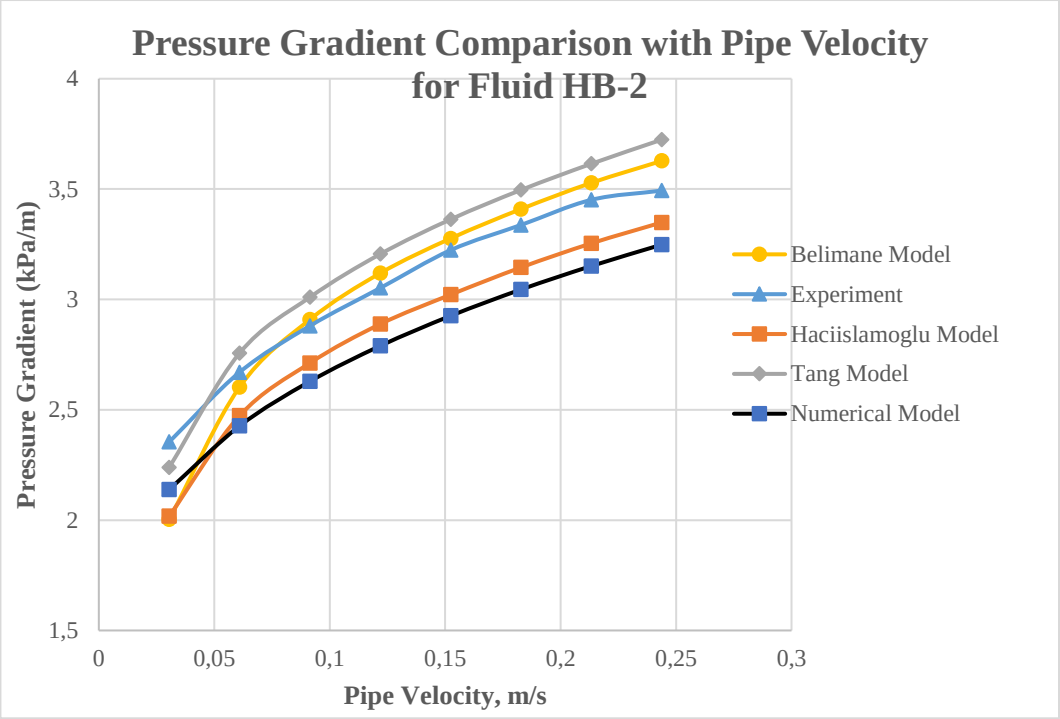

Figure 7.12 Surge and Swab Pressure Gradient Comparison – Model and Experiment Results for HB-2 Fluid in Eccentric Annulus for Varying Pipe Velocity

Table 7.9 AAPEs for Comparative Study for HB-2 Fluid

$V_p, m/s$	AAPE-Experimental Study	AAPE-Model in Belimane	AAPE-Model in Tang	AAPE-Model in Haciislamoglu
0.0304	9.17	6.74	4.49	5.98
0.0609	9.12	6.77	11.97	1.88
0.0914	8.73	9.64	12.67	3.07
0.1219	8.59	10.57	12.98	3.42
0.1523	9.23	10.70	13.00	3.17
0.1828	8.76	10.69	12.90	3.18
0.2133	8.69	10.68	12.82	3.16
0.2438	7.01	10.46	12.77	3.01

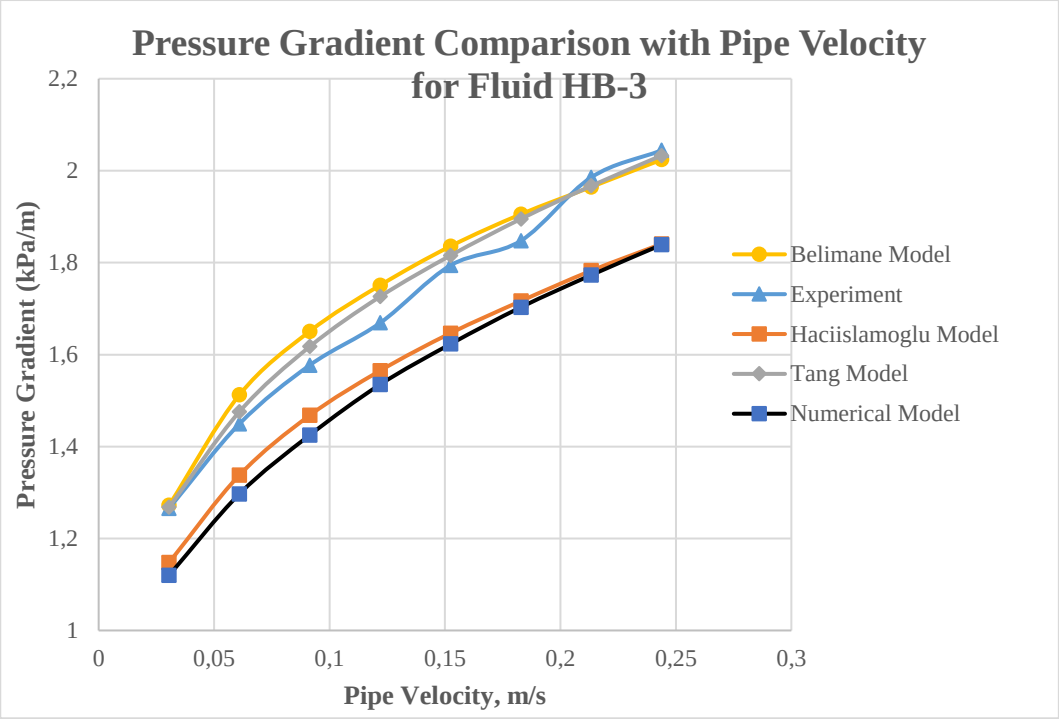

Figure 7.13 Surge and Swab Pressure Gradient Comparison – Model and Experiment Results for HB-3 Fluid in Eccentric Annulus for Varying Pipe Velocity

Table 7.10 AAPEs for Comparative Study for HB-3 Fluid

$V_p, m/s$	AAPE-Experimental Study	AAPE-Model in Belimane	AAPE-Model in Tang	AAPE-Model in Haciislamoglu
0.0304	11.50	11.96	9.49	2.40
0.0609	10.51	14.24	9.34	3.05
0.0914	9.64	13.68	9.24	2.93
0.1219	8.03	12.33	9.34	1.92
0.1523	9.53	11.59	9.30	1.43
0.1828	7.83	10.62	9.43	0.79
0.2133	10.70	9.76	9.38	0.53
0.2438	10.04	9.14	9.46	0.10

The AAPE values indicate the level of agreement between the proposed numerical model and the other models for different pipe velocities. In the analysis with the fluid HB-1, it is observed that the proposed model consistently performs well in terms of accuracy, as the mean AAPE values stays below 12.12% for all the four comparative means, i.e., one experimental study and three different models from existing literature. Minimum AAPE among all is less than 1%, while the maximum is 21.31%, which can be seen only in one occasion. This suggests that the proposed numerical model achieves reasonably close predictions to an experimental study and other models using the experimental data across the considered range of pipe velocities and a highly eccentric annulus. It is also evident that the proposed numerical model shows better agreement with the experimental study and the model developed by Haciislamoglu and Langlinais (1990), i.e., lower AAPEs with HB-1 fluid.

Comparison with HB-2 fluid yields overall lower AAPEs, i.e., better agreement, when comparing with the previous analysis with HB-1 as depicted in Figure 7.12 and in Table 7.8. The mean AAPE is 8.31% when considering all four comparative studies with fluid HB-2. Average AAPEs stay below 10% when analyzing separately, except for the comparison with the model presented in Tang et al. (2016), the average AAPE of which is 11.70%.

Similar trends and findings can be seen in the comparative study for HB-3 fluid. Mean AAPE for all four studies is 8.10%, minimum and maximum are calculated as 0.10%, and 14.24%, respectively. The minimum AAPE belongs to the comparison with the model developed by Haciislamoglu and Langlinais (1990), where the maximum AAPE is found in the comparison with the model developed by Belimane et al. (2021).

Overall, the comparison highlights the strength of the proposed numerical model in predicting surge and swab pressure for various pipe velocities. Its performance is particularly notable when compared to the experimental data and the model developed by Haciislamoglu and Langlinais (1990), with consistently low AAPE

values. While some differences exist when comparing with the other models, the relatively lower AAPE values for the Haciislamoglu and Langlinais (1990) model and the experimental study indicate a closer agreement with the proposed numerical model. This reaffirms the effectiveness of the model and its potential for accurate surge pressure estimation in highly eccentric annuli for yield power law fluids.

In summary, proposed numerical model demonstrates overall good performance in predicting surge pressures for the three different YPL fluids. The mean AAPE values are within an acceptable range, and the minimum and maximum values indicate reasonable deviations. Relatively lower AAPEs are observed in the comparisons of proposed numerical model with the experimental study and the model developed by Haciislamoglu and Langlinais (1990); which is the indication of a closer agreement. These findings suggest the reliability and effectiveness of the proposed numerical model in estimating surge pressures in eccentric annuli for various YPL fluids.

CHAPTER 8

SURROGATE MODELING OF SURGE AND SWAB PRESSURES IN ECCENTRIC ANNULI

Numerically solving the Navier-Stokes equations is complex and requires a significant computational power. In general, complex physics-based models require substantial computational resources and cannot be used as a digital twin for parameter optimization and as a result cannot be applied to real-time operations. In such situations, the surrogate models that are usually computationally-fast statistical methods that correlate the input and output relationship are more appropriate. A surrogate model can be used as a digital twin and capture the physics within the boundary it is constructed for. A representative sample matrix of inputs and outputs have to be presented to construct an accurate surrogate model. This sample matrix may be based on a grid of equal increments in input values. The simulations are typically conducted based on the sample matrix. The surrogate model is then trained on this dataset to capture the input and output relationship.

In this thesis, an Artificial Neural Network (ANN)-based surrogate model is constructed to overcome the drawbacks of physics-based numerical solution of YPL fluid flow in eccentric annuli such as long run time and numerical convergence problems. ANN's are well-known to capture the non-linear complex relationships between input and outputs of a system very well and are a good fit for surrogate modeling (Sun and Wang, 2019). The accuracy of the ANN will then be compared to the results from the numerical solution to assess if the surrogate model is sufficiently trained. Recent publications in literature suggest an increased interest for the applications of machine learning techniques for wellbore hydraulics (Sun and Wang, (2019), Ozbayoglu et al., (2021), Ozbayoglu et al., (2018), Wang and Salehi (2015), Krishna et al., (2020a), Avci (2018), Krishna et al., (2020b), Jondahl and

Viumdal (2018), Rooki et al., (2014), Singh et al., (2018), Mohammad and Davidrajuh (2022), Sorgun et al., (2015), Shirangi et al., (2020), Agwu et al., (2020), Kumar et al., (2020)).

The overall aim is to construct an ANN-based surrogate model that will accurately predict the pressure losses in eccentric annuli while tripping with YPL fluids. The major benefit of the ANN is to significantly lower computational resource consumption in comparison to the numerical model while providing similar accuracy. Using such a surrogate model, the surface parameters can be optimized in real-time for a safe and efficient tripping operation. A sample matrix of inputs is designed as the first step to construct a surrogate model. A dataset is created using actual field values that is common in drilling operations as inputs. With this way, the developed surrogate model will be a representative model and can be directly applied in today's operations. For instance, different WBM and OBM's are taken into consideration while selecting minimum and maximum fluid parameters; common pipe velocity and eccentricity values were used and diameter ratios encompasses a range starting from smaller annular gaps such as 6-in x 4½-in to larger configurations such as 17½-in x 6-in and 12¼-in x 6¼-in. Also, laboratory scale parameters are used; i.e., 1-in x 0.66-in and 1-in x 0.5-in diameters and pipe velocity of 0.03 m/s. The sample matrix and the associated dataset information is presented in Table 8.1:

Table 8.1 Sample Matrix Designed to Populate the Dataset for the Surrogate Model

	Minimum	**Maximum**	**Increment**	**# of data points**
$\boldsymbol{\tau_y}$**-** $\boldsymbol{Pa}$	0.5	9.5	3.0	4
$\boldsymbol{n}$	0.3	0.9	0.3	3
$\boldsymbol{K}$**-** $\boldsymbol{Pa \cdot s^n}$**,**	0.3	1.5	0.3	5
$\boldsymbol{V_p}$**-**$\boldsymbol{m/s}$	0.03	1.5	0.3	6
$\boldsymbol{\varepsilon}$	0	1	0.25	5
$\boldsymbol{R_i/R_o}$	0.34	0.82	Custom	6
			$\sum$	10,800

This dataset is converted into predictor variables (inputs in the order: $\tau_y, K, n, V_p, \varepsilon, R_i, R_o$) which is a matrix of 7x10800 and a single target variable of pressure loss (dp/dl).

8.1 Artificial Neural Networks Surrogate Model

An Artificial Neural Networks (ANN) is constructed in MATLAB (MATLAB, 2019), which provides a practical machine learning interface and proven underlying methods that are commonly used/deployed in industrial applications as favored in Ozbayoglu et al., (2021), Putcha and Ertekin (2017) and in Rooki and Rakhshkhorshid (2017). The following steps are followed to construct the surrogate model:

1- The dataset is imported into MATLAB's workspace and converted into a .mat file. The predictor variables are included as different columns in the same matrix variable.
2- The default two-layer feed-forward neural network is used. A sigmoid activation function is used in the hidden layer and a linear activation function is applied in the output layer. The network consists of 7 inputs ($\tau_0, K, n, V_p, \varepsilon, R_i, R_o$) and 1 output ($dp/dl$). The architecture of the neural network is presented in the Figure 8.1.

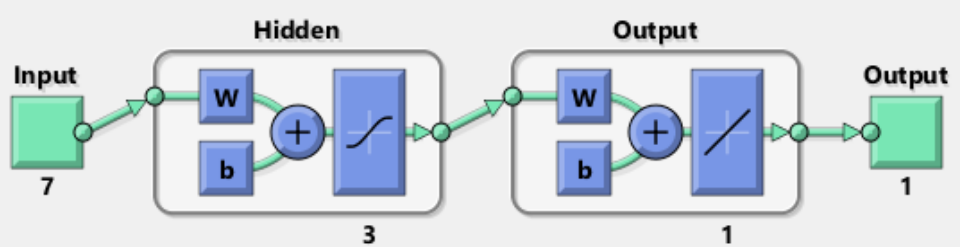

Figure 8.1 Artificial Neural Networks (ANN) Architecture for the Surrogate Model

This architecture is practical and easy to implement. Several other more complex designs are evaluated, however there wasn't a significant improvement in the results. Therefore, the proposed ANN architecture of two-layer feed-forward neural network is used. This networks is also suggested to be a good fit for multi-dimensional mapping problems (MATLAB, 2019). Different neuron sizes are evaluated and three-neuron network is found to be sufficient for this surrogate model. It is possible to increase the neuron amount, however the aim is to construct a generalized model that avoids overfitting the sample matrix and the dataset. Therefore, the hidden layer neuron size is set as 3. This network is trained with Levenberg-Marquardt algorithm (Levenberg (1944), Marquardt (1963)) which is a fast backpropagation algorithm recommended as a first-choice supervised algorithm (Sapna et al., 2012)). It is important to randomly shuffle the dataset before the training to avoid any bias. Therefore, the dataset is randomly shuffled and divided to training and test datasets with a 4:1 ratio, which is a common ratio widely adapted by the researchers in this field as in Ozbayoglu et al., (2021) and Ozbayoglu et al., (2018). After establishing the train to test ratio and the backpropagation method, the network is constructed and trained using the MATLAB's *fitnet* and *trainfunction* functions (MATLAB, 2019). The testing is commenced using the *net*, *gsubtract* and *perform* functions. The *net* function creates a custom shallow neural network, *gsubtract* subtracts the test results and actual values element-wise and perform function calculates a scalar value that is used to measure the network's performance. In this case, the mean squared error function is used for performance assessment during the backpropagation. Training the network took 1000 epochs and a μ of $1x10^{-1}$ is achieved, which is the control parameter for the algorithm that directly affects the error convergence. The summary of the network training algorithms and progress results are presented in Figure 8.2. Further details regarding with the ANN model such as the weight and biases resulted from training are presented in Table 8.2.

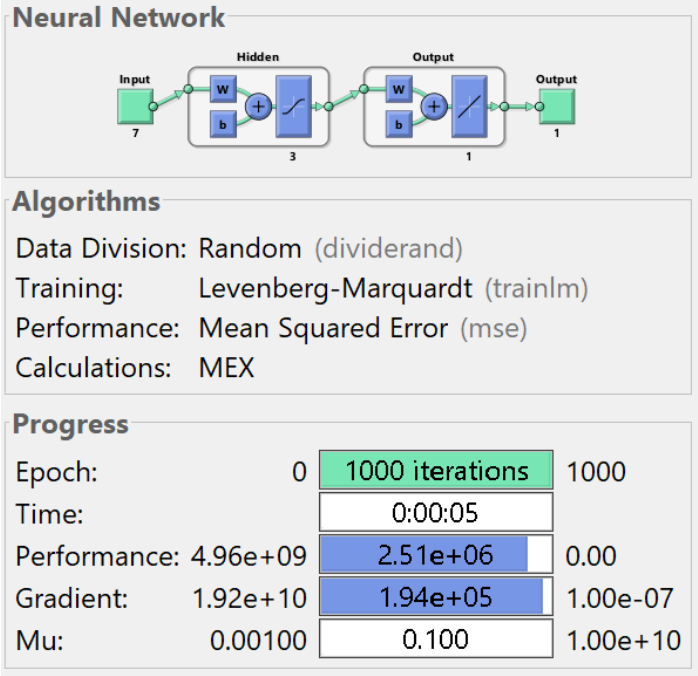

Figure 8.2 ANN Training Algorithms and Progress Results

Table 8.2 Weights and Biases of the Proposed ANN Model

the input-to-hidden layer weights						
-0.01169	-0.77506	-1.25054	0.046502	0.130966	176.194	-81.3316
0.011739	0.774075	1.249146	-0.0419	-0.131	-279.041	129.258
-0.06032	-1.94948	-10.7932	-0.89979	0.153819	8.330346	-3.86933
the hidden-to-output layer weights						
				244.0163	244.5535	-0.05326
the input-to-hidden layer bias						
				100.87	-158.1	14.87
the hidden-to-output layer bias						
						-0.4

In the following figures the metrics of the training and the performance of the neural network is presented. Figure 8.3 shows the evolution of mean square error (MSE)

during training the network across the epochs. The results show that the maximum performance is achieved at 1000th epoch. However, it can also be observed that the network reaches a fair degree of accuracy at about 500th epoch and the training maybe stopped. However, an overall 5 second training time (as presented in Figure 8.2) is fairly low and further optimization will not be needed. The error histogram of the trained ANN is presented in Figure 8.4. The result show that the errors are accumulated around 0 for both the test and training datasets, which is a good indication for accurate prediction. The trained ANN-based surrogate model's training, test and overall performance is presented in the Figure 8.5, which shows that the surrogate model can capture the input and output relationship of the numerical solution for swab and surge pressure prediction of YPL fluids in eccentric annuli. The training, test and all dataset results show a similar distribution and R test for all of them resulted above 0.99, which both show that the surrogate model is accurate and can replicate the underlying physics of the numerical solution. Further statistical metrics are calculated and presented in Table 8.3.

Table 8.3 Statistical Metrics for the ANN Based Surrogate Model

RMSE	**R^2**	**MAE**	**p**
1580	0.99	807	~0

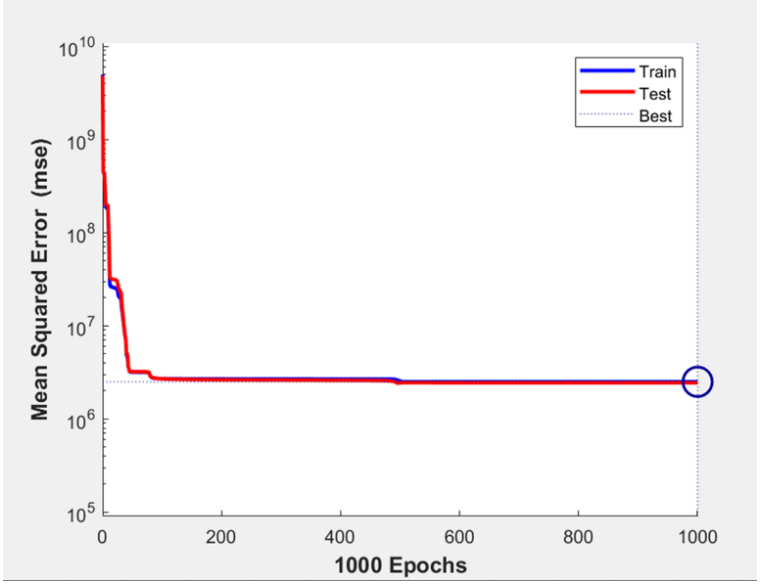

Figure 8.3 MSE vs Training Epochs for ANN

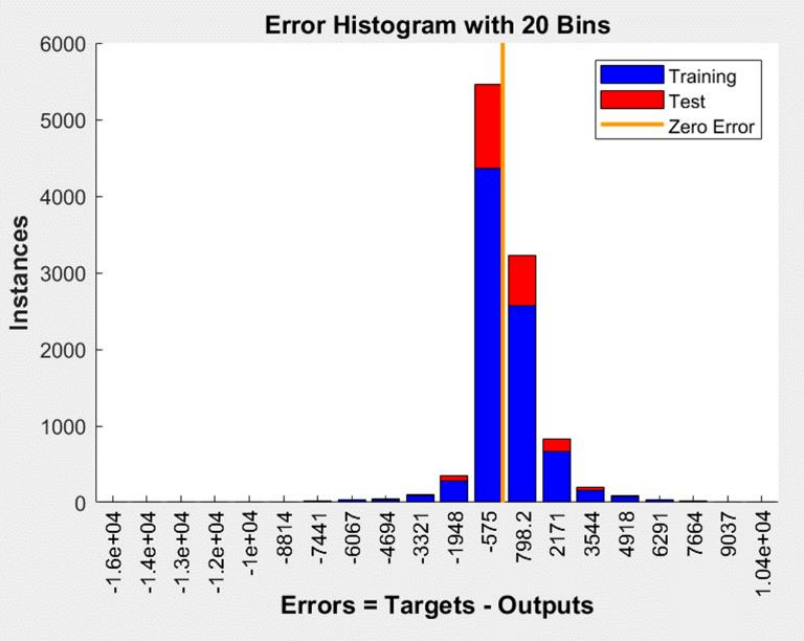

Figure 8.4 Error Histogram of the Trained ANN

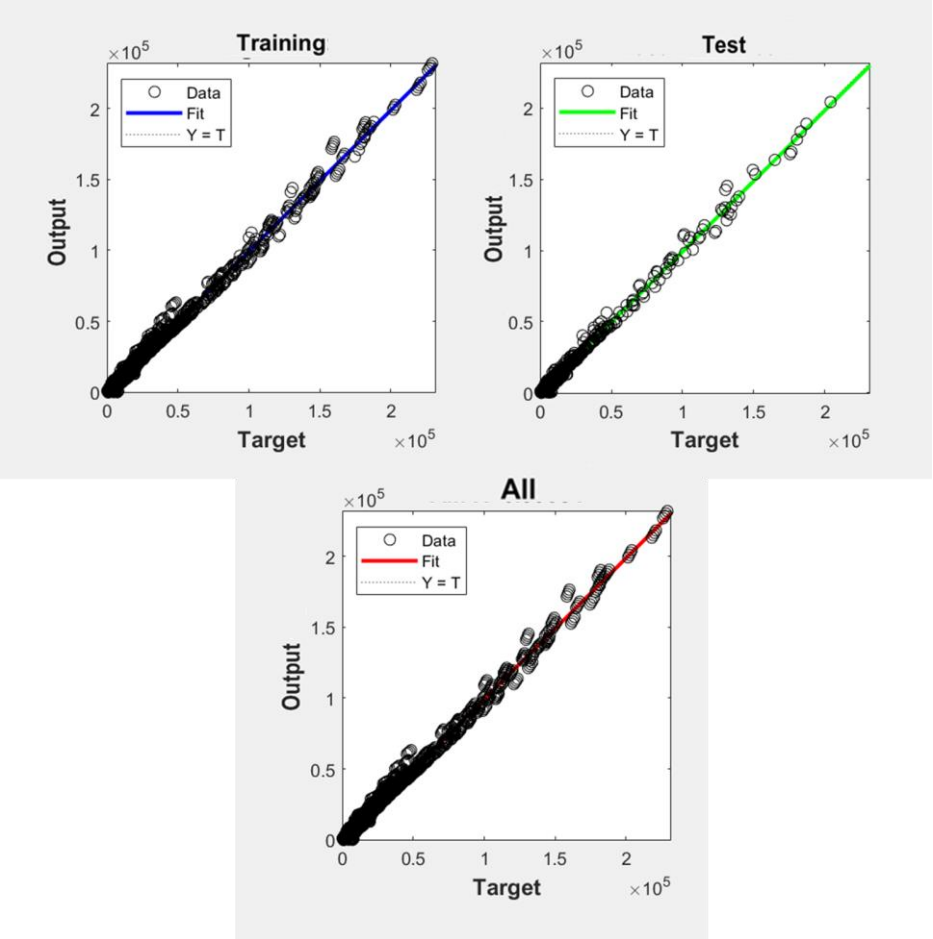

Figure 8.5 ANN - Output vs. Target for the Training, Test and All Dataset Results

Here, RMSE is a measure of how well the model is able to predict the target variable. A value of 1580 might seem relatively high; however, it should be taken into account that the results are presented in the SI unit of Pa/m, which is usually high in magnitude in well construction (such as up to $2 \cdot 10^5$ Pa/m, around 8 psi/ft as shown in Figure 8.5). For that reason, all the statistical metrics should be considered together. The coefficient of determination, R^2 indicates how well the model fits the data and a value of 0.99 shows that the model explains a large portion of variation in the target variable of pressure gradients, which indicates that it is a good fit. Median absolute error, MAE, shows that the prediction error that is less sensitive to outliers. This shows that overall model error is relatively low and at about 807 Pa/m. The

RMSE value is affected by some outliers, but the MAE value is less sensitive to them. Lastly the p value is an indicator of the significance of the results. A p-value of 0 is considered statistically significant, indicating that the results are unlikely to have occurred by chance. This suggests that the observed difference between the prediction and the true values is likely due to the model's ability to capture the underlying patterns in the data, rather than random noise or chance. Overall, when all the statistical metrics are considered together, the predictions are not statistically different from the true values and the model shows a good fit. The proposed model can be used in the field applications within the boundaries of the input parameters presented in Table 8.1.

8.2 Random Forest Surrogate Model

Random Forest (RF) is a versatile algorithm that can capture nonlinear relationships and can capture the input-output relationship fairly well (Breiman, (2001)). An RF model is developed using the MATLAB's *TreeBagger*() function, which is an ensemble of bagged decision trees used for regression. This function uses bootstrap aggregation ensemble method, which reduces overfitting and improves generalization.

The following steps are taken to construct the surrogate model:

1- Various hyperparameters are tested manually to asses the most accurate and practical fit. This included adjusting parameters such as the number of trees, minimum leaf size, maxiumum depth. Ultimately, it was found that 50 trees were sufficient to achieve good results without further restricting the model or increasing the computational time. For the rest of the parameters, the default values are used.

2- An input matrix of 7 variables ($\tau_0, K, n, V_p, \varepsilon, R_i, R_o$) are used in the model and 1 output (dp/dl) is considered as the target variable.

Details of this RF model such as the configuration and properties are presented in Table 8.4.

Table 8.4 Configuration Values of the Random Forest (RF)

DeltaCriterionDecisionSplit						
4444	81064	196222	146510	27255	38762	194863
NumPredictorSplit						
9.97	11.68	2.43	12.45	10.30	1.12	2.06
DefaultYFit						
						7147
weight						
						1.11

where *DeltaCriterionDecisionSplit* is a split criterion and *NumPredictorSplit* defines the number of decision splits for each predictor. *DefaultYFit* is a default prediction value, which controls the predicted value and is the mean of the response for the training data, w represents observation weights, which controls the growth of each decision tree in the ensemble. The results from the training, test and entire dataset using RF is presented in Figure 8.6. The results indicate that the model has a good fit, particularly at lower pressure gradient values. However, it can be observed that the fit is not as good at higher values, as more data points fall on the lower triangle in the figure. This suggests that at higher pressure gradients, the RF surrogate model tends to underestimate the pressure losses. Further statistical metrics are calculated and presented in Table 8.5.

Table 8.5 Statistical Metrics for the RF Based Surrogate Model

RMSE	**R^2**	**MAE**	**p**
2928	0.98	175	0.43

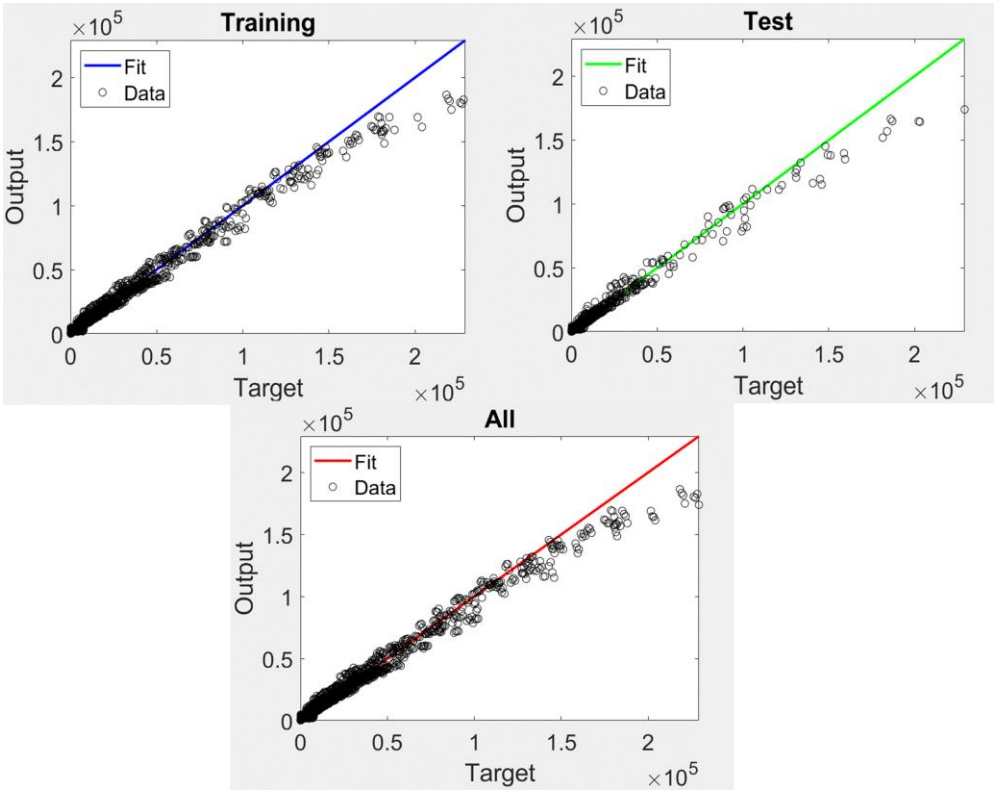

Figure 8.6 RF - Output vs. Target for the Training, Test and All Dataset Results

In comparison to the Artificial Neural Network (ANN) model, the RF regression had a higher RMSE value, indicating lower accuracy. The R-squared value is 0.98, which is also slightly lower than that of the ANN model, which measures how well the model fits the data. However, the Median Absolute Error (MAE) for the RF based model is 175, which is lower than the ANN's 807. This suggests that the RF model can produce more accurate results in the median, ignoring outliers. The *p*-value of 0.43 for the RF model is higher than the ANN model, meaning that the ANN model is a better fit showing that the accuracy is less likely occurred by any chance. The *p*-value of 0.43 suggests that there is some difference between the predictions made by the model and the true values, but this difference is not statistically significant.

In order to show the applicability and reveal the performance of both surrogate models, a comparative study was conducted. Figure 8.7 shows the comparison of

surge and swab pressure gradients among the proposed numerical model results, ANN surrogate model results, RF surrogate model results and the experiments conducted in Tang et al. (2016) with varying pipe velocity for three different YPL fluids for highly eccentric annulus, $\varepsilon = 0.9$. Overall, both surrogate models are seen to have a good fit with the proposed numerical model and the experiments.

While comparing the numerical model with surrogate models; the AAPE (average absolute percent error) values for the ANN model range from 2.65% to 10.92%, with an average of 7.59% for HB-1 fluid. On the other hand, the AAPE values for the RF model range from 0.67% to 14.24%, with an average of 5.14% for the same fluid. For fluid HB-2, it seems that both the ANN and RF models perform well for all the data points, staying below 10% AAPE. It can be observed that the AAPE for fluid HB-2 is generally lower for the RF model than the ANN model. The average AAPE for ANN is 8.49%, while it is 2.49% for RF surrogate model. For fluid HB-3, the AAPE values for the ANN model are higher than the RF model, suggesting that the RF model is performing better than the ANN model at the specified lower flow rates. Average absolute percent errors are ranging from 0.11% to 33.99% with an average of 10.02% for ANN, and from 1.21% to 14.88% with an average of 4.88% for RF. Table 8.6 lists the minimum, maximum and average AAPEs for both ANN and RF analysis.

Table 8.6 Minimum, Maximum and Average Errors for ANN and RF

	Artificial Neural Networks			Random Forest		
	Minimum AAPE	Maximum AAPE	Average AAPE	Minimum AAPE	Maximum AAPE	Average AAPE
HB-1	2.65	10.92	7.59	0.67	14.24	5.14
HB-2	1.01	10.76	8.49	0.37	9.05	2.49
HB-3	0.11	33.99	10.02	1.21	14.88	4.88

As shown in Table 8.6, it is safe to conclude that, on average, the RF model performs better compared to the ANN model in predicting surge and swab pressure gradient, within the boundaries of the properties used in this experimental data.

Detailed surge and swab pressure inputs, outputs and AAPEs for this comparative study with surrogate models and experimental work are presented in Table B.10, Table B.11 and in Table B.12 in Appendix B.

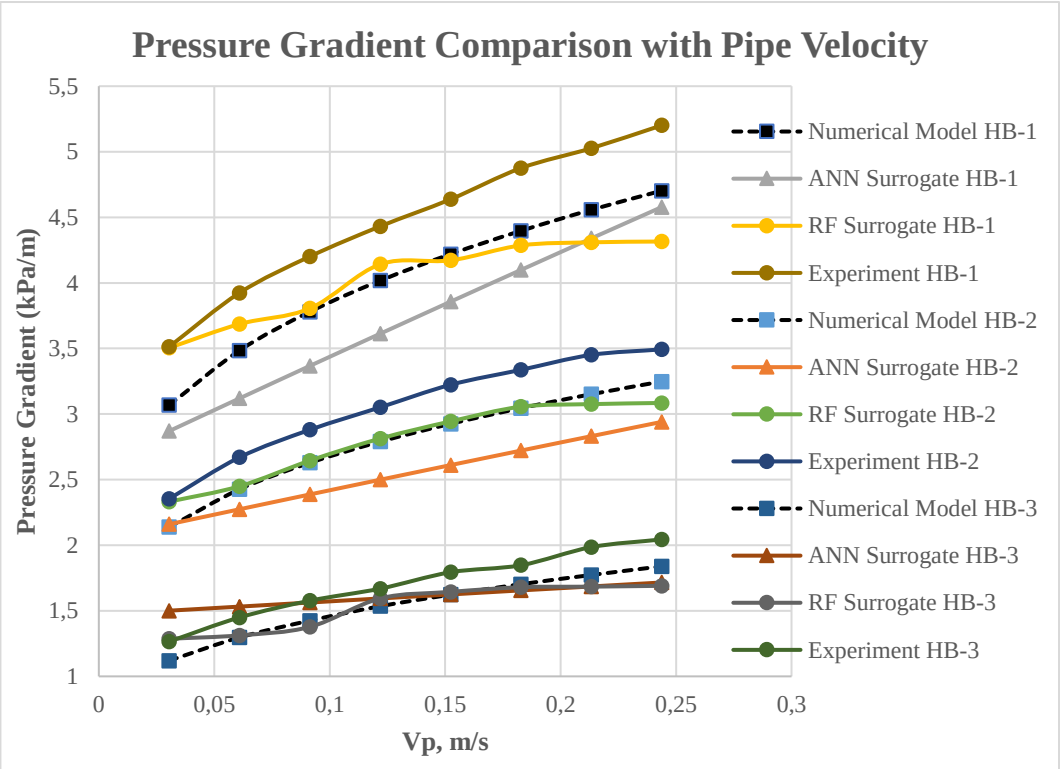

Figure 8.7 Surge and Swab Pressure Gradient Comparison – Numerical Model, Surrogate Models and Experiment Results YPL Fluids in Eccentric Annulus for Varying Pipe Velocity

It is important to highlight that the performance of the models may vary depending on the specific dataset used, and the chosen hyperparameters. Therefore, while the RF model may be performing better than the ANN model; it may not be necessarily the case for every condition. On another note, the pipe velocity input parameters in the comparison study were mostly in the lower values, due to possible constraints in the experimental set-up. However, surrogate models were fed with mostly higher

tripping velocities, because of its better reflection of the actual field conditions, i.e., tripping speed ranging from 0.3 m/s to 1.5 m/s. Therefore, the surrogates are expected to perform better while running with field parameters.

Overall, there are pros and cons to both the ANN and RF models. The ANN model shows an overall better fit with a higher R-squared value, lower RMSE and lower p value but the RF model has a lower MAE value, indicating that it is better at handling outliers. When all the statistical metrics are considered together, the results suggest that the RF model fits well to the data at low pressure loss values but not as well at high pressure loss values. The ANN model, on the other hand, shows an overall good fit to the data that captures the high pressure loss values fairly well.

CHAPTER 9

CONCLUSIONS AND RECOMMENDATIONS

9.1 Conclusions

A numerical model based on physics has been proposed to predict surge and swab pressures in eccentric annuli. This model takes into account the effects of temperature, fluid properties, and geometric properties, and incorporates YPL fluids. Proposed model accounts for steady state, fully developed and laminar flow of an incompressible YPL fluid. The model has been validated using computational fluid dynamics analysis and compared with other models and experimental studies from the literature with differences found between 1-15%. The results indicate that the proposed model accurately predicts pressure losses during surge and swab in eccentric annuli.

Results of the model demonstrate that YPL model fluid parameters; flow behavior index, yield stress, consistency index, as well as diameter ratio and pipe velocity are directly proportional with resulting surge and swab pressures; meaning that an increase in those parameters would lead to an increase in surge and swab pressures. The effects become more pronounced with diameter ratio and flow behavior index due to their exponential nature. On the other hand, eccentricity is inversely proportional with the surge and swab pressures. It is seen that surge and swab pressures decrease significantly when comparing a concentric case to a fully eccentric one.

The proposed model also takes into account the effects of temperature on rheological parameters, using a data-driven approach that has been validated with API's empirical equations. The results show that the data-driven model estimates

rheological values similarly to the API equations, providing a more robust alternative to empirical equations for estimating rheological parameters of drilling fluids.

Two surrogate models have been developed using the proposed physics-based model, using machine learning techniques such as Artificial Neural Network and Random Forest. These surrogate models are computationally cheaper and allow for real-time optimization of drilling parameters without the need for a full physics simulation. Both models have pros and cons, when all the statistical metrics are considered together, the results suggest that the Random Forest model fits well to the data at low pressure loss values but not as well at high pressure loss values. The Artificial Neural Network model, on the other hand, shows an overall good fit to the data that captures the high pressure loss values fairly well.

Overall, this thesis presents various practical modeling approaches for predicting surge and swab pressure in eccentric annuli, which can improve the accuracy of pressure estimation in drilling operations and prevent kick or lost circulation, while maintaining the desired equivalent circulating density.

9.2 Recommendations for Future Work

Numerical model presented in this thesis is based on physics and considers various parameters that affect surge and swab pressures. However, to enhance its practicality, future work should focus on integrating real-time data and drilling conditions into the model. Incorporating downhole sensor data, such as pressure, temperature, and flow rate, could enable continuous updates and adaptability of the model during drilling operations. Implementing an online monitoring system that continuously updates the model with real-time data and dynamically adjusts drilling parameters could lead to more accurate and efficient pressure predictions, ultimately improving drilling safety and performance. Additionally, the model should incorporate the transient nature of fluid flow, considering factors such as flow rate variations and temporal effects. Also, the slightly compressible nature of most drilling fluids may

be considered. This enhanced dynamic flow model will provide a more realistic representation of surge and swab pressures, improving the accuracy and reliability of the predictions.

While the surrogate models based on Artificial Neural Networks (ANN) and Random Forest (RF) have shown promising results, future work could delve into more advanced machine learning techniques. Techniques such as Gradient Boosting Machines, Long Short-Term Memory networks (LSTMs), or Transformer-based models could be investigated to further improve the accuracy and generalization of the surrogate model; as they are known for their ability to handle complex patterns and capture non-linear relationships. These advanced techniques have shown great potential in various domains and may yield even better performance for predicting surge and swab pressures in eccentric annuli. Additionally, considering ensemble methods that combine multiple models could help mitigate the limitations of individual models and provide more robust predictions.

In conclusion, the proposed numerical model and surrogate models have laid a solid foundation for predicting surge and swab pressures in eccentric annuli. Yet again, there is potential for further advancement by exploring more advanced machine learning techniques and incorporating dynamic flow modeling. By leveraging advanced algorithms and incorporating real-time data, the accuracy and applicability of the models can be enhanced, enabling more precise predictions and better decision-making in drilling operations. These advancements will contribute to the safety, efficiency, and optimization of drilling operations in the oil and gas industry.

REFERENCES

Agwu, O. E., Akpabio, J. U., & Dosunmu, A. (2020). Artificial Neural Network Model for Predicting Drill Cuttings Settling Velocity. *Petroleum*, *6*(4), 340–352.

Altun G., Ettehadi, A., Ozyurtkan A. H., (2014) Customization of Sepiolite Based Drilling Fluids at High Temperatures. *Proceedings of 48th US Rock Mechanics / Geomechanics Symposium, 2014-June*.

ANSYS Inc. (2020). ANSYS Fluent User's Guide, Release 2020b. *Theory Guide*.

API, American Petroleum Institute. (2017). *Recommended Practice on the Rheology and Hydraulics of Oil-well Drilling Fluids: Vol. seventh*.

Aspen Sysdrill, "Sysdrill Brochure", aspentech.com, https://www.aspentech.com/en/resources/brochure/aspen-sysdrill, accessed on July 1, 2023

Avci, E. (2018). An Artificial Neural Network approach for the Prediction of Water-Based Drilling Fluid Rheological Behaviour. *International Advanced Researches and Engineering Journal*, *2*(2), 124–131.

Bartlett, L. E. (1967). Effect of temperature on the flow properties of drilling fluids. *Fall Meeting of the Society of Petroleum Engineers of AIME*.

Belimane, Z., Hadjadj, A., Ferroudji, H., Rahman, M. A., & Qureshi, M. F. (2021). Modeling Surge Pressures During Tripping Operations in Eccentric Annuli. *Journal of Natural Gas Science and Engineering*, *96*, 104233.

Bingham, E.C., (1922). Fluidity and Plasticity, McGraw-Hill, New York, 215

Bourgoyne, A. T., & Young, F. S. (1974). A Multiple Regression Approach to Optimal Drilling and Abnormal Pressure Detection. *Society of Petroleum Engineers Journal*, *14*(04), 371–384.

Breiman, L. (2001). Random Forests. *Machine Learning*, *45*(1), 5–32.

Burkhardt, J. (1961). Wellbore Pressure Surges Produced by Pipe Movement. *Journal of Petroleum Technology*, *Volume 13*(Number 6), 595–605. https://doi.org/10.2118/1546-G

Cannon, G. E. (1934). Changes in Hydrostatic Pressure Due to Withdrawing Drill Pipe from the Hole. *API Drilling and Production Practices*, *April*, 42–47.

Cardwell Jr., W. T. (1934). Pressure Changes in Drilling Wells caused by Pipe Movement. *API Drilling and Production Practices*, *June*, 97–112.

Carrasco-Teja, M., & Frigaard, I. A. (2010). Non-Newtonian Fluid Displacements in Horizontal Narrow Eccentric Annuli: Effects of Slow Motion of the Inner Cylinder. *Journal of Fluid Mechanics*, *653*, 137–173. https://doi.org/10.1017/S0022112010000212

Crespo, F., & Ahmed, R. (2013). A simplified Surge and Swab Pressure Model for Yield Power Law Fluids. *Journal of Petroleum Science and Engineering*, 101, 12–20.

Crespo, F., Ahmed, R., Saasen, A. et al. (2012). Surge and Swab Pressure Predictions for Yield Power Law Drilling Fluids. *SPE Drill & Compl*, 27 (4): 574-585

Epelle, E. I., & Gerogiorgis, D. I. (2020). A Review of Technological Advances and Open Challenges for Oil and Gas Drilling Systems Engineering. AIChE Journal, 66(4), e16842.

Erge, O. (2016). Modeling of Surge and Swab Pressure of Yield Power Law Fluids. *Master's thesis*, Middle East Technical University.

Erge, O., Akin, S., & Gucuyener, I. H. (2018). Accurate Modeling of Surge and Swab Pressures of Yield Power Law Fluids in Concentric Annuli. *Proceedings of the SPE/IADC Middle East Drilling Technology Conference and Exhibition*, *2018-January*.

Erge, O., Ozbayoglu, E. M., Miska, S. Z., Yu, M., Takach, N., Saasen, A., & May, R. (2016). Equivalent Circulating Density Modeling of Yield Power Law Fluids Validated with CFD Approach. *Journal of Petroleum Science and Engineering*, *140*. https://doi.org/10.1016/j.petrol.2015.12.027

Erge, O., Sakaoglu, K., Sonmez, A., Bagatir, G., Dogan, H. A., Ay, A., & Gucuyener, I. H. (2020). Overview and Design Principles of Drilling Fluids Systems for Geothermal Wells in Turkey. *Geothermics*, *88*. https://doi.org/10.1016/j.geothermics.2020.101897

Erge, O., Sakaoglu, K., Sonmez, A., & Dogan, H. A. (2022). Investigation of HT Drilling Fluids Performance-A Review of Over 90 Field Cases in 3000m+ Deep Geothermal Wells in Turkey. *Proceedings of the European Geothermal Congress, 2022-October*

Erge, O., Vajargah, A. K., Ozbayoglu, E. M., Oort, E. V. (2015). Frictional Pressure Loss of Drilling Fluids in a Fully Eccentric Annulus. *Journal of Natural Gas Science and Engineering*, *26*. https://dx.doi.org/10.1016/j.jngse.2015.07.030

Ettehadi, A., Altun, G. (2018). In-Situ Thermal Rheological Properties of Drilling Muds. *Proceedings of the SPE/IADC Middle East Drilling Technology Conference and Exhibition*, *2018-January*.

Fontenot, J. E., & Clark, R. K. (1974). An Improved Method for Calculating Swab and Surge Pressures and Circulating Pressures in a Drilling Well. *Society of Petroleum Engineers Journal*, *14*(05), 451–462.

Forsythe, G. E. (1977). Computer Methods for Mathematical Computations. *Prentice-Hall Series in Automatic Computation*, *259*.

Haciislamoglu, M., & Langlinais, J. (1990). Non-Newtonian Flow in Eccentric Annuli. *Journal of Energy Resources Technology*, *112*(3), 163–169. https://doi.org/10.1115/1.2905753

He, Shimming., Tang, Ming., Xiong, Jiyou. et al. (2016). A Numerical Model to Predict Surge and Swab Pressures for Yield Power Law Fluid in Concentric Annuli with Open-ended Pipe. *Journal of Petroleum Science and Engineering*, (145) 464-472. http://dx.doi.org/10.1016/j.petrol.2016.05.039

Heyda, J. F. (1959). A Green's Function Solution for the Case of Laminar Incompressible Flow Between non-Concentric Circular Cylinders. *Journal of the Franklin Institute*, *267*(1), 25–34.

Herschel, W.H., Bulkley, R., (1926). Measurement of consistency as applied to rubber–benzene solutions. *Proceedings of the American Society of Testing Materials*, 26, 621.

Iyoho, A. W., & Azar, J. J. (1981). An Accurate Slot-Flow Model for Non-Newtonian Fluid Flow Through Eccentric Annuli. *Society of Petroleum Engineers Journal*, *21*(05), 565–572.

Jondahl, M. H., & Viumdal, H. (2018). Estimating Rheological Properties of non-Newtonian Drilling Fluids Using Ultrasonic-Through-Transmission Combined with Machine Learning Methods. *2018 IEEE International Ultrasonics Symposium (IUS)*, 1–4.

Krishna, S. (2020). *OTC-30311-MS* New Analytical Approach for Predicting Surge/Swab Pressure Gradient Using Mud Clinging Effect and Frictional Pressure Losses: for Yield Power Law Fluid. *Proceedings of Offshore Technology Conference, 2020-November.*

Krishna, S., Ridha, S., & Vasant, P. (2020a). Prediction of Bottom-Hole Pressure Differential During Tripping Operations Using Artificial Neural Networks (ANN). In *Intelligent Computing and Innovation on Data Science* (pp. 379–388). Springer.

Krishna, S., Ridha, S., Vasant, P., Ilyas, S. U., Irawan, S., & Gholami, R. (2020b). Explicit Flow Velocity Modelling of Yield Power-Law Fluid in Concentric

Annulus to Predict Surge and Swab Pressure Gradient for Petroleum Drilling Applications. *Journal of Petroleum Science and Engineering*, *195*, 107743.

Kumar, A., Ridha, S., Ganet, T., Vasant, P., & Ilyas, S. U. (2020). Machine Learning Methods for Herschel–Bulkley Fluids in Annulus: Pressure Drop Predictions and Algorithm Performance Evaluation. *Applied Sciences*, *10*(7), 2588.

Lal, M. (1983). Surge and Swab Modeling for Dynamic Pressures and Safe Trip Velocities. *IADC/SPE Drilling Conference*. (11412), 427. doi:10.2118/11412-MS

Levenberg, K. (1944). A Method for the Solution of Certain non-Linear Problems in Least Squares. *Quarterly of Applied Mathematics*, *2*(2), 164–168.

Lubinski, A., Hsu, F. H., & Nolte, K. G. (1977). Transient Pressure Surges Due to Pipe Movement in an Oil Well. *Revue de l'Inst. Franc. Du Pet.*, 307–347.

Luo, Y., & Peden, J. M. (1990). Flow of non-Newtonian Fluids Through Eccentric Annuli. *SPE Production Engineering*, *5*(01), 91–96. https://doi.org/10.2118/16692-pa

Mangani, L., & Bianchini, C. (2007). Heat Transfer Applications in Turbomachinery. *Proceedings of the OpenFOAM International Conference*.

Marquardt, D. W. (1963). An Algorithm for Least-Squares Estimation of Nonlinear Parameters. *Journal of the Society for Industrial and Applied Mathematics*, *11*(2), 431–441.

MATLAB. (2019). *9.7.0.1190202 (R2019b)*. The MathWorks Inc.

Mitchell, R. F. (1988). Dynamic Surge/Swab Pressure Predictions. *SPE Drilling Engineering*, *3*(03), 325–333. doi:10.2118/16156-PA

Mohammad, A., & Davidrajuh, R. (2022). Modeling of Swab and Surge Pressures: A Survey. *Applied Sciences*, *12*(7), 3526.

Ozbayoglu, E. M., Erge, O., & Ozbayoglu, M. A. (2018). Predicting the Pressure Losses While the Drillstring is Buckled and Rotating Using Artificial Intelligence Methods. *Journal of Natural Gas Science and Engineering*, *56*, 72–80.

Ozbayoglu, E., Ozbayoglu, M., Ozdilli, B. G., & Erge, O. (2021). Optimization of Flow Rate and Pipe Rotation Speed Considering Effective Cuttings Transport Using Data-Driven Models. *Energies*, *14*(5), 1484.

Putcha, V. B., & Ertekin, T. (2017). A Fast and Robust Compositional, Multi-Phase, Non-Isothermal Wellbore Hydraulics Model for Vertical Wells. *SPE Annual Technical Conference and Exhibition*.

PVI Software, "SurgeMOD", pvisoftware.com, https://www.pvisoftware.com/surgemod-surge-pressure-prediction.html, accessed on July 1, 2023

Rommetveit, R., & Bjørkevoll, K. S. (1997, November). Temperature and Pressure Effects on Drilling Fluid Rheology and ECD in Very Deep Wells. *All Days*. https://doi.org/10.2118/39282-MS

Rooki, R., Ardejani, F. D., & Moradzadeh, A. (2014). Hole Cleaning Prediction in Foam Drilling Using Artificial Neural Network and Multiple Linear Regression. *Geomaterials, 2014*.

Rooki, R., & Rakhshkhorshid, M. (2017). Cuttings Transport Modeling in Underbalanced Oil Drilling Operation Using Radial Basis Neural Network. *Egyptian Journal of Petroleum*, *26*(2), 541–546.

Samuel, G. R., Sunthankar, A., McColpin, G., Bern, P., & Flynn, T. (2003). Field Validation of Transient Swab-Surge Response with Real-Time Downhole Pressure Data. *SPE Drilling & Completion*, *18*(04), 280–283.

Sapna, S. (2012). *Backpropagation Learning Algorithm Based on Levenberg Marquardt Algorithm*. 393–398. https://doi.org/10.5121/csit.2012.2438

Sayindla, S., Lund, B., Ytrehus, J. D., & Saasen, A. (2019). CFd modeling of hydraulic behavior of oil- A nd water-based drilling fluids in laminar flow. *SPE Drilling and Completion*, *34*(3), 207–215. https://doi.org/10.2118/184660-PA

Schuh, F. J. (1964). Computer Makes Surge-Pressure Calculations Useful. *The Oil and Gas Journal*, 96.

Shirangi, M. G., Ettehadi, R., Aragall, R., Furlong, E., May, R., Dahl, T., Samnejad, M., & Thompson, C. (2020). Digital Twins for Drilling Fluids: Advances and Opportunities. *IADC/SPE International Drilling Conference and Exhibition*.

Singh, K., Miska, S., Ozbayoglu, E., & Alp Aydin, B. (2018). Using Supervised Machine Learning Algorithms to Predict Pressure Drop in Narrow Annulus. *SPE/AAPG Eastern Regional Meeting*.

Sorgun, M. (2011) Computational Fluid Dynamics Modeling of Pipe Eccentricity Effect on Flow Characteristics of Newtonian and Non-Newtonian Fluids, Energy Sources, Part A: Recovery, Utilization, and Environmental Effects, 33:12, 1196-1208, DOI: 10.1080/15567036.2010.492381

Sorgun, M., Ozbayoglu, M. A., & Ozbayoglu, E. M. (2015). Support Vector Regression and Computational Fluid Dynamics Modeling of Newtonian and Non-Newtonian Fluids in Annulus with Pipe Rotation. *Journal of Energy Resources Technology*, *137*(3), 32901.

Sun, G., & Wang, S. (2019). A Review of the Artificial Neural Network Surrogate Modeling in Aerodynamic Design. *Proceedings of the Institution of Mechanical Engineers, Part G: Journal of Aerospace Engineering*, *233*(16), 5863–5872.

Tang, M., Ahmed, R., Srivastav, R., & He, S. (2016). Simplified Surge Pressure Model for Yield Power Law Fluid in Eccentric Annuli. *Journal of Petroleum Science and Engineering*, *145*, 346–356.

Tao, L. N., & Donovan, W. F. (1955). Through-Flow in Concentric and Eccentric Annuli of Fine Clearance with and without Relative Motion of the Boundaries. *Transactions of the American Society of Mechanical Engineers*, *77*(8), 1291–1299.

Uner, D., Ozgen, C., & Tosun, I. (1988). An Approximate Solution for non-Newtonian Flow in Eccentric Annuli. *Industrial & Engineering Chemistry Research*, *27*(4), 698–701.

Vaughn, R. D. (1965). Axial Laminar Flow of non-Newtonian Fluids in Narrow Eccentric Annuli. *Society of Petroleum Engineers Journal*, *5*(04), 277–280.

Wang, Y., & Salehi, S. (2015). Application of Real-Time Field Data to Optimize Drilling Hydraulics Using Neural Network Approach. *Journal of Energy Resources Technology*, *137*(6).

APPENDICES

A. Sensitivity Analysis Input and Output Dataset

A parametric study was conducted to display sensitivity of each key parameters on surge and swab pressures and presented in Chapter 4.2. A number of inputs were run into developed numerical model and resultant surge and swab pressure gradient is collected. This appendix includes the full dataset of input and outputs for the sensitivity analysis.

Table A.1 Inputs and Outputs for Sensitivity Analysis Shown in Figure 4.7, Effect of Consistency Index on Surge and Swab Pressures of YPL Fluids with Different Eccentricities

τ_y, Pa	$K, Pa.s^n$	n	$V_p, m/s$	ε	R_o, m	R_i, m	R_i $/R_o$	$\frac{dp}{dl}, kPa/m$
9.5	0.3	0.3	1.2	0	0.222	0.0762	0.342	0.1571
9.5	0.6	0.3	1.2	0	0.222	0.0762	0.342	0.1685
9.5	0.9	0.3	1.2	0	0.222	0.0762	0.342	0.1804
9.5	1.2	0.3	1.2	0	0.222	0.0762	0.342	0.1925
9.5	1.5	0.3	1.2	0	0.222	0.0762	0.342	0.2046
9.5	0.3	0.3	1.2	0.25	0.222	0.0762	0.342	0.1297
9.5	0.6	0.3	1.2	0.25	0.222	0.0762	0.342	0.1415
9.5	0.9	0.3	1.2	0.25	0.222	0.0762	0.342	0.1534
9.5	1.2	0.3	1.2	0.25	0.222	0.0762	0.342	0.1652
9.5	1.5	0.3	1.2	0.25	0.222	0.0762	0.342	0.1768
9.5	0.3	0.3	1.2	0.5	0.222	0.0762	0.342	0.1081
9.5	0.6	0.3	1.2	0.5	0.222	0.0762	0.342	0.1181
9.5	0.9	0.3	1.2	0.5	0.222	0.0762	0.342	0.1282
9.5	1.2	0.3	1.2	0.5	0.222	0.0762	0.342	0.1382
9.5	1.5	0.3	1.2	0.5	0.222	0.0762	0.342	0.1480
9.5	0.3	0.3	1.2	0.75	0.222	0.0762	0.342	0.0925
9.5	0.6	0.3	1.2	0.75	0.222	0.0762	0.342	0.1012
9.5	0.9	0.3	1.2	0.75	0.222	0.0762	0.342	0.1100
9.5	1.2	0.3	1.2	0.75	0.222	0.0762	0.342	0.1186
9.5	1.5	0.3	1.2	0.75	0.222	0.0762	0.342	0.1272
9.5	0.3	0.3	1.2	0.99	0.222	0.0762	0.342	0.0816
9.5	0.6	0.3	1.2	0.99	0.222	0.0762	0.342	0.0914
9.5	0.9	0.3	1.2	0.99	0.222	0.0762	0.342	0.0998
9.5	1.2	0.3	1.2	0.99	0.222	0.0762	0.342	0.1080
9.5	1.5	0.3	1.2	0.99	0.222	0.0762	0.342	0.1162

Table A.2 Inputs and Outputs for Sensitivity Analysis Shown in Figure 4.8, Effect of Yield Stress on Surge and Swab Pressures of YPL Fluids with Different Eccentricities

τ_y, Pa	$K, Pa.s^n$	n	$V_p, m/s$	ε	R_o, m	R_i, m	R_i /R_o	$\frac{dp}{dl}, kPa/m$
0.5	1.2	0.9	0.6	0	0.0762	0.0572	0.75	24.619
3.5	1.2	0.9	0.6	0	0.0762	0.0572	0.75	25.079
6.5	1.2	0.9	0.6	0	0.0762	0.0572	0.75	25.539
9.5	1.2	0.9	0.6	0	0.0762	0.0572	0.75	25.999
12.5	1.2	0.9	0.6	0	0.0762	0.0572	0.75	26.458
0.5	1.2	0.9	0.6	0.25	0.0762	0.0572	0.75	23.709
3.5	1.2	0.9	0.6	0.25	0.0762	0.0572	0.75	24.151
6.5	1.2	0.9	0.6	0.25	0.0762	0.0572	0.75	24.593
9.5	1.2	0.9	0.6	0.25	0.0762	0.0572	0.75	25.035
12.5	1.2	0.9	0.6	0.25	0.0762	0.0572	0.75	25.476
0.5	1.2	0.9	0.6	0.5	0.0762	0.0572	0.75	21.785
3.5	1.2	0.9	0.6	0.5	0.0762	0.0572	0.75	22.181
6.5	1.2	0.9	0.6	0.5	0.0762	0.0572	0.75	22.576
9.5	1.2	0.9	0.6	0.5	0.0762	0.0572	0.75	22.970
12.5	1.2	0.9	0.6	0.5	0.0762	0.0572	0.75	23.364
0.5	1.2	0.9	0.6	0.75	0.0762	0.0572	0.75	19.319
3.5	1.2	0.9	0.6	0.75	0.0762	0.0572	0.75	19.645
6.5	1.2	0.9	0.6	0.75	0.0762	0.0572	0.75	19.970
9.5	1.2	0.9	0.6	0.75	0.0762	0.0572	0.75	20.294
12.5	1.2	0.9	0.6	0.75	0.0762	0.0572	0.75	20.617
0.5	1.2	0.9	0.6	0.99	0.0762	0.0572	0.75	16.822
3.5	1.2	0.9	0.6	0.99	0.0762	0.0572	0.75	17.107
6.5	1.2	0.9	0.6	0.99	0.0762	0.0572	0.75	17.392
9.5	1.2	0.9	0.6	0.99	0.0762	0.0572	0.75	17.675
12.5	1.2	0.9	0.6	0.99	0.0762	0.0572	0.75	17.958

Table A.3 Inputs and Outputs for Sensitivity Analysis Shown in Figure 4.9, Effect of Flow Behavior Index on Surge and Swab Pressures of YPL Fluids with Different Eccentricities

τ_y, Pa	$K, Pa.s^n$	n	$V_p, m/s$	ε	R_o, m	R_i, m	R_i /R_o	$\frac{dp}{dl}, kPa/m$
6.5	0.3	0.3	1.2	0	0.0254	0.0127	0.5	1.491
6.5	0.3	0.45	1.2	0	0.0254	0.0127	0.5	2.041
6.5	0.3	0.6	1.2	0	0.0254	0.0127	0.5	3.278
6.5	0.3	0.75	1.2	0	0.0254	0.0127	0.5	6.133
6.5	0.3	0.9	1.2	0	0.0254	0.0127	0.5	12.912
6.5	0.3	0.3	1.2	0.25	0.0254	0.0127	0.5	1.281
6.5	0.3	0.45	1.2	0.25	0.0254	0.0127	0.5	1.846
6.5	0.3	0.6	1.2	0.25	0.0254	0.0127	0.5	3.082
6.5	0.3	0.75	1.2	0.25	0.0254	0.0127	0.5	5.873
6.5	0.3	0.9	1.2	0.25	0.0254	0.0127	0.5	12.478
6.5	0.3	0.3	1.2	0.5	0.0254	0.0127	0.5	1.071
6.5	0.3	0.45	1.2	0.5	0.0254	0.0127	0.5	1.560
6.5	0.3	0.6	1.2	0.5	0.0254	0.0127	0.5	2.665
6.5	0.3	0.75	1.2	0.5	0.0254	0.0127	0.5	5.258
6.5	0.3	0.9	1.2	0.5	0.0254	0.0127	0.5	11.502
6.5	0.3	0.3	1.2	0.75	0.0254	0.0127	0.5	0.917
6.5	0.3	0.45	1.2	0.75	0.0254	0.0127	0.5	1.345
6.5	0.3	0.6	1.2	0.75	0.0254	0.0127	0.5	2.332
6.5	0.3	0.75	1.2	0.75	0.0254	0.0127	0.5	4.676
6.5	0.3	0.9	1.2	0.75	0.0254	0.0127	0.5	10.384
6.5	0.3	0.3	1.2	0.99	0.0254	0.0127	0.5	0.811
6.5	0.3	0.45	1.2	0.99	0.0254	0.0127	0.5	1.199
6.5	0.3	0.6	1.2	0.99	0.0254	0.0127	0.5	2.086
6.5	0.3	0.75	1.2	0.99	0.0254	0.0127	0.5	4.188
6.5	0.3	0.9	1.2	0.99	0.0254	0.0127	0.5	9.311

Table A.4 Inputs and Outputs for Sensitivity Analysis Shown in Figure 4.10, Effect of Pipe Velocity on Surge and Swab Pressures of YPL Fluids with Different Eccentricities

τ_y, Pa	$K, Pa.s^n$	n	$V_p, m/s$	ε	R_o, m	R_i, m	R_i /R_o	$\frac{dp}{dl}, kPa/m$
3.5	1.5	0.3	0.3	0	0.0254	0.0168	0.66	3.118
3.5	1.5	0.3	0.6	0	0.0254	0.0168	0.66	3.618
3.5	1.5	0.3	0.9	0	0.0254	0.0168	0.66	3.962
3.5	1.5	0.3	1.2	0	0.0254	0.0168	0.66	4.232
3.5	1.5	0.3	1.5	0	0.0254	0.0168	0.66	4.458
3.5	1.5	0.3	0.3	0.25	0.0254	0.0168	0.66	2.855
3.5	1.5	0.3	0.6	0.25	0.0254	0.0168	0.66	3.322
3.5	1.5	0.3	0.9	0.25	0.0254	0.0168	0.66	3.643
3.5	1.5	0.3	1.2	0.25	0.0254	0.0168	0.66	3.895
3.5	1.5	0.3	1.5	0.25	0.0254	0.0168	0.66	4.106
3.5	1.5	0.6	0.3	0.5	0.0254	0.0168	0.66	2.424
3.5	1.5	0.6	0.6	0.5	0.0254	0.0168	0.66	2.825
3.5	1.5	0.6	0.9	0.5	0.0254	0.0168	0.66	3.101
3.5	1.5	0.6	1.2	0.5	0.0254	0.0168	0.66	3.319
3.5	1.5	0.6	1.5	0.5	0.0254	0.0168	0.66	3.500
3.5	1.5	0.3	0.3	0.75	0.0254	0.0168	0.66	2.082
3.5	1.5	0.3	0.6	0.75	0.0254	0.0168	0.66	2.429
3.5	1.5	0.3	0.9	0.75	0.0254	0.0168	0.66	2.667
3.5	1.5	0.3	1.2	0.75	0.0254	0.0168	0.66	2.854
3.5	1.5	0.3	1.5	0.75	0.0254	0.0168	0.66	3.011
3.5	1.5	0.3	0.3	0.99	0.0254	0.0168	0.66	1.829
3.5	1.5	0.3	0.6	0.99	0.0254	0.0168	0.66	2.134
3.5	1.5	0.3	0.9	0.99	0.0254	0.0168	0.66	2.343
3.5	1.5	0.3	1.2	0.99	0.0254	0.0168	0.66	2.508
3.5	1.5	0.3	1.5	0.99	0.0254	0.0168	0.66	2.645

Table A.5 Inputs and Outputs for Sensitivity Analysis Shown in Figure 4.11, Effect of Yield Stress on Surge and Swab Pressures of YPL Fluids with Different Eccentricities

τ_y, Pa	$K, Pa.s^n$	n	$V_p, m/s$	ε	R_o, m	R_i, m	R_i /R_o	$\frac{dp}{dl}, kPa/m$
0.5	0.9	0.3	0.9	0	0.1556	0.0794	0.51	0.105
3.5	0.9	0.3	0.9	0	0.1556	0.0794	0.51	0.196
6.5	0.9	0.3	0.9	0	0.1556	0.0794	0.51	0.285
9.5	0.9	0.3	0.9	0	0.1556	0.0794	0.51	0.373
12.5	0.9	0.3	0.9	0	0.1556	0.0794	0.51	0.460
0.5	0.9	0.3	0.9	0.25	0.1556	0.0794	0.51	0.097
3.5	0.9	0.3	0.9	0.25	0.1556	0.0794	0.51	0.175
6.5	0.9	0.3	0.9	0.25	0.1556	0.0794	0.51	0.249
9.5	0.9	0.3	0.9	0.25	0.1556	0.0794	0.51	0.322
12.5	0.9	0.3	0.9	0.25	0.1556	0.0794	0.51	0.394
0.5	0.9	0.3	0.9	0.5	0.1556	0.0794	0.51	0.083
3.5	0.9	0.3	0.9	0.5	0.1556	0.0794	0.51	0.147
6.5	0.9	0.3	0.9	0.5	0.1556	0.0794	0.51	0.209
9.5	0.9	0.3	0.9	0.5	0.1556	0.0794	0.51	0.269
12.5	0.9	0.3	0.9	0.5	0.1556	0.0794	0.51	0.329
0.5	0.9	0.3	0.9	0.75	0.1556	0.0794	0.51	0.072
3.5	0.9	0.3	0.9	0.75	0.1556	0.0794	0.51	0.126
6.5	0.9	0.3	0.9	0.75	0.1556	0.0794	0.51	0.179
9.5	0.9	0.3	0.9	0.75	0.1556	0.0794	0.51	0.231
12.5	0.9	0.3	0.9	0.75	0.1556	0.0794	0.51	0.282
0.5	0.9	0.3	0.9	0.99	0.1556	0.0794	0.51	0.064
3.5	0.9	0.3	0.9	0.99	0.1556	0.0794	0.51	0.112
6.5	0.9	0.3	0.9	0.99	0.1556	0.0794	0.51	0.158
9.5	0.9	0.3	0.9	0.99	0.1556	0.0794	0.51	0.204
12.5	0.9	0.3	0.9	0.99	0.1556	0.0794	0.51	0.249

Table A.6 Inputs and Outputs for Sensitivity Analysis Shown in Figure 4.12, Effect of Diameter Ratio on Surge and Swab Pressures of YPL Fluids with Different Eccentricities

τ_y, Pa	$K, Pa.s^n$	n	$V_p, m/s$	ε	R_o, m	R_i, m	R_i /R_o	$\frac{dp}{dl}, kPa/m$
9.5	0.6	0.3	0.3	0	0.10795	0.0381	0.35	0.344
9.5	0.6	0.3	0.3	0	0.10795	0.0508	0.47	0.433
9.5	0.6	0.3	0.3	0	0.10795	0.0635	0.59	0.576
9.5	0.6	0.3	0.3	0	0.10795	0.0762	0.71	0.846
9.5	0.6	0.3	0.3	0	0.10795	0.0889	0.82	1.528
9.5	0.6	0.3	0.3	0.25	0.10795	0.0381	0.35	0.288
9.5	0.6	0.3	0.3	0.25	0.10795	0.0508	0.47	0.365
9.5	0.6	0.3	0.3	0.25	0.10795	0.0635	0.59	0.491
9.5	0.6	0.3	0.3	0.25	0.10795	0.0762	0.71	0.729
9.5	0.6	0.3	0.3	0.25	0.10795	0.0889	0.82	1.339
9.5	0.6	0.3	0.3	0.5	0.10795	0.0381	0.35	0.240
9.5	0.6	0.3	0.3	0.5	0.10795	0.0508	0.47	0.305
9.5	0.6	0.3	0.3	0.5	0.10795	0.0635	0.59	0.410
9.5	0.6	0.3	0.3	0.5	0.10795	0.0762	0.71	0.611
9.5	0.6	0.3	0.3	0.5	0.10795	0.0889	0.82	1.123
9.5	0.6	0.3	0.3	0.75	0.10795	0.0381	0.35	0.205
9.5	0.6	0.3	0.3	0.75	0.10795	0.0508	0.47	0.261
9.5	0.6	0.3	0.3	0.75	0.10795	0.0635	0.59	0.351
9.5	0.6	0.3	0.3	0.75	0.10795	0.0762	0.71	0.523
9.5	0.6	0.3	0.3	0.75	0.10795	0.0889	0.82	0.961
9.5	0.6	0.3	0.3	0.99	0.10795	0.0381	0.35	0.182
9.5	0.6	0.3	0.3	0.99	0.10795	0.0508	0.47	0.230
9.5	0.6	0.3	0.3	0.99	0.10795	0.0635	0.59	0.309
9.5	0.6	0.3	0.3	0.99	0.10795	0.0762	0.71	0.458
9.5	0.6	0.3	0.3	0.99	0.10795	0.0889	0.82	0.839

Table A.7 Inputs and Outputs for Sensitivity Analysis Shown in Figure 4.13, Effect of Diameter Ratio on Surge and Swab Pressures of YPL Fluids with Different Eccentricities

τ_y, Pa	$K, Pa.s^n$	n	$V_p, m/s$	ε	R_o, m	R_i, m	R_i /R_o	$\frac{dp}{dl}, kPa/m$
9.5	0.6	0.3	0.3	0	0.10795	0.0381	0.35	0.344
9.5	0.6	0.3	0.3	0	0.10795	0.0508	0.47	0.433
9.5	0.6	0.3	0.3	0	0.10795	0.0635	0.59	0.576
9.5	0.6	0.3	0.3	0	0.10795	0.0762	0.71	0.846
9.5	0.6	0.3	0.3	0	0.10795	0.0889	0.82	1.528
9.5	0.6	0.3	0.3	0.25	0.10795	0.0381	0.35	0.288
9.5	0.6	0.3	0.3	0.25	0.10795	0.0508	0.47	0.365
9.5	0.6	0.3	0.3	0.25	0.10795	0.0635	0.59	0.491
9.5	0.6	0.3	0.3	0.25	0.10795	0.0762	0.71	0.729
9.5	0.6	0.3	0.3	0.25	0.10795	0.0889	0.82	1.339
9.5	0.6	0.3	0.3	0.5	0.10795	0.0381	0.35	0.240
9.5	0.6	0.3	0.3	0.5	0.10795	0.0508	0.47	0.305
9.5	0.6	0.3	0.3	0.5	0.10795	0.0635	0.59	0.410
9.5	0.6	0.3	0.3	0.5	0.10795	0.0762	0.71	0.611
9.5	0.6	0.3	0.3	0.5	0.10795	0.0889	0.82	1.123
9.5	0.6	0.3	0.3	0.75	0.10795	0.0381	0.35	0.205
9.5	0.6	0.3	0.3	0.75	0.10795	0.0508	0.47	0.261
9.5	0.6	0.3	0.3	0.75	0.10795	0.0635	0.59	0.351
9.5	0.6	0.3	0.3	0.75	0.10795	0.0762	0.71	0.523
9.5	0.6	0.3	0.3	0.75	0.10795	0.0889	0.82	0.961
9.5	0.6	0.3	0.3	0.99	0.10795	0.0381	0.35	0.182
9.5	0.6	0.3	0.3	0.99	0.10795	0.0508	0.47	0.230
9.5	0.6	0.3	0.3	0.99	0.10795	0.0635	0.59	0.309
9.5	0.6	0.3	0.3	0.99	0.10795	0.0762	0.71	0.458
9.5	0.6	0.3	0.3	0.99	0.10795	0.0889	0.82	0.839

Table A.8 Inputs and Outputs for Sensitivity Analysis Shown in Figure 4.14, Effect of Yield Stress on Surge and Swab Pressures of YPL Fluids with Different Eccentricities

τ_y, Pa	$K, Pa.s^n$	n	$V_p, m/s$	ε	R_o, m	R_i, m	R_i /R_o	$\frac{dp}{dl}, kPa/m$
0.5	0.6	0.3	0.3	0	0.10795	0.0762	0.71	0.205
3.5	0.6	0.3	0.3	0	0.10795	0.0762	0.71	0.424
6.5	0.6	0.3	0.3	0	0.10795	0.0762	0.71	0.636
9.5	0.6	0.3	0.3	0	0.10795	0.0762	0.71	0.847
12.5	0.6	0.3	0.3	0	0.10795	0.0762	0.71	1.059
0.5	0.6	0.3	0.3	0.25	0.10795	0.0762	0.71	0.190
3.5	0.6	0.3	0.3	0.25	0.10795	0.0762	0.71	0.378
6.5	0.6	0.3	0.3	0.25	0.10795	0.0762	0.71	0.556
9.5	0.6	0.3	0.3	0.25	0.10795	0.0762	0.71	0.730
12.5	0.6	0.3	0.3	0.25	0.10795	0.0762	0.71	0.904
0.5	0.6	0.3	0.3	0.5	0.10795	0.0762	0.71	0.162
3.5	0.6	0.3	0.3	0.5	0.10795	0.0762	0.71	0.318
6.5	0.6	0.3	0.3	0.5	0.10795	0.0762	0.71	0.466
9.5	0.6	0.3	0.3	0.5	0.10795	0.0762	0.71	0.611
12.5	0.6	0.3	0.3	0.5	0.10795	0.0762	0.71	0.755
0.5	0.6	0.3	0.3	0.75	0.10795	0.0762	0.71	0.139
3.5	0.6	0.3	0.3	0.75	0.10795	0.0762	0.71	0.272
6.5	0.6	0.3	0.3	0.75	0.10795	0.0762	0.71	0.399
9.5	0.6	0.3	0.3	0.75	0.10795	0.0762	0.71	0.523
12.5	0.6	0.3	0.3	0.75	0.10795	0.0762	0.71	0.646
0.5	0.6	0.3	0.3	0.99	0.10795	0.0762	0.71	0.122
3.5	0.6	0.3	0.3	0.99	0.10795	0.0762	0.71	0.238
6.5	0.6	0.3	0.3	0.99	0.10795	0.0762	0.71	0.349
9.5	0.6	0.3	0.3	0.99	0.10795	0.0762	0.71	0.458
12.5	0.6	0.3	0.3	0.99	0.10795	0.0762	0.71	0.566

Table A.9 Inputs and Outputs for Sensitivity Analysis Shown in Figure 4.15, Effect of Pipe Velocity on Surge and Swab Pressures of YPL Fluids with Different Eccentricities

τ_y, Pa	$K, Pa.s^n$	n	$V_p, m/s$	ε	R_o, m	R_i, m	R_i /R_o	$\frac{dp}{dl}, kPa/m$
9.5	0.6	0.3	0.3	0	0.10795	0.0762	0.71	0.847
9.5	0.6	0.3	0.6	0	0.10795	0.0762	0.71	0.889
9.5	0.6	0.3	0.9	0	0.10795	0.0762	0.71	0.917
9.5	0.6	0.3	1.2	0	0.10795	0.0762	0.71	0.940
9.5	0.6	0.3	1.5	0	0.10795	0.0762	0.71	0.958
9.5	0.6	0.3	0.3	0.25	0.10795	0.0762	0.71	0.730
9.5	0.6	0.3	0.6	0.25	0.10795	0.0762	0.71	0.772
9.5	0.6	0.3	0.9	0.25	0.10795	0.0762	0.71	0.800
9.5	0.6	0.3	1.2	0.25	0.10795	0.0762	0.71	0.822
9.5	0.6	0.3	1.5	0.25	0.10795	0.0762	0.71	0.840
9.5	0.6	0.3	0.3	0.5	0.10795	0.0762	0.71	0.611
9.5	0.6	0.3	0.6	0.5	0.10795	0.0762	0.71	0.646
9.5	0.6	0.3	0.9	0.5	0.10795	0.0762	0.71	0.670
9.5	0.6	0.3	1.2	0.5	0.10795	0.0762	0.71	0.689
9.5	0.6	0.3	1.5	0.5	0.10795	0.0762	0.71	0.704
9.5	0.6	0.3	0.3	0.75	0.10795	0.0762	0.71	0.523
9.5	0.6	0.3	0.6	0.75	0.10795	0.0762	0.71	0.553
9.5	0.6	0.3	0.9	0.75	0.10795	0.0762	0.71	0.573
9.5	0.6	0.3	1.2	0.75	0.10795	0.0762	0.71	0.589
9.5	0.6	0.3	1.5	0.75	0.10795	0.0762	0.71	0.603
9.5	0.6	0.3	0.3	0.99	0.10795	0.0762	0.71	0.458
9.5	0.6	0.3	0.6	0.99	0.10795	0.0762	0.71	0.484
9.5	0.6	0.3	0.9	0.99	0.10795	0.0762	0.71	0.502
9.5	0.6	0.3	1.2	0.99	0.10795	0.0762	0.71	0.516
9.5	0.6	0.3	1.5	0.99	0.10795	0.0762	0.71	0.528

Table A.10 Inputs and Outputs for Sensitivity Analysis Shown in Figure 4.16, Effect of Flow Behavior Index on Surge and Swab Pressures of YPL Fluids with Different Eccentricities

τ_y, Pa	$K, Pa.s^n$	n	$V_p, m/s$	ε	R_o, m	R_i, m	R_i /R_o	$\frac{dp}{dl}, kPa/m$
9.5	0.6	0.3	0.3	0	0.10795	0.0762	0.71	0.847
9.5	0.6	0.45	0.3	0	0.10795	0.0762	0.71	1.038
9.5	0.6	0.6	0.3	0	0.10795	0.0762	0.71	1.369
9.5	0.6	0.75	0.3	0	0.10795	0.0762	0.71	1.940
9.5	0.6	0.9	0.3	0	0.10795	0.0762	0.71	2.947
9.5	0.6	0.3	0.3	0.25	0.10795	0.0762	0.71	0.730
9.5	0.6	0.45	0.3	0.25	0.10795	0.0762	0.71	0.939
9.5	0.6	0.6	0.3	0.25	0.10795	0.0762	0.71	1.284
9.5	0.6	0.75	0.3	0.25	0.10795	0.0762	0.71	1.851
9.5	0.6	0.9	0.3	0.25	0.10795	0.0762	0.71	2.835
9.5	0.6	0.3	0.3	0.5	0.10795	0.0762	0.71	0.611
9.5	0.6	0.45	0.3	0.5	0.10795	0.0762	0.71	0.792
9.5	0.6	0.6	0.3	0.5	0.10795	0.0762	0.71	1.100
9.5	0.6	0.75	0.3	0.5	0.10795	0.0762	0.71	1.631
9.5	0.6	0.9	0.3	0.5	0.10795	0.0762	0.71	2.568
9.5	0.6	0.3	0.3	0.75	0.10795	0.0762	0.71	0.523
9.5	0.6	0.45	0.3	0.75	0.10795	0.0762	0.71	0.678
9.5	0.6	0.6	0.3	0.75	0.10795	0.0762	0.71	0.945
9.5	0.6	0.75	0.3	0.75	0.10795	0.0762	0.71	1.409
9.5	0.6	0.9	0.3	0.75	0.10795	0.0762	0.71	2.239
9.5	0.6	0.3	0.3	0.99	0.10795	0.0762	0.71	0.458
9.5	0.6	0.45	0.3	0.99	0.10795	0.0762	0.71	0.594
9.5	0.6	0.6	0.3	0.99	0.10795	0.0762	0.71	0.828
9.5	0.6	0.75	0.3	0.99	0.10795	0.0762	0.71	1.235
9.5	0.6	0.9	0.3	0.99	0.10795	0.0762	0.71	1.961

Table A.11 Inputs and Outputs for Sensitivity Analysis Shown in Figure 4.17, Effect of Consistency Index on Surge and Swab Pressures of YPL Fluids with Different Eccentricities

τ_y, Pa	$K, Pa.s^n$	n	$V_p, m/s$	ε	R_o, m	R_i, m	R_i /R_o	$\frac{dp}{dl}, kPa/m$
9.5	0.3	0.3	0.3	0	0.10795	0.0762	0.71	0.759
9.5	0.6	0.3	0.3	0	0.10795	0.0762	0.71	0.847
9.5	0.9	0.3	0.3	0	0.10795	0.0762	0.71	0.937
9.5	1.2	0.3	0.3	0	0.10795	0.0762	0.71	1.026
9.5	1.5	0.3	0.3	0	0.10795	0.0762	0.71	1.114
9.5	0.3	0.3	0.3	0.25	0.10795	0.0762	0.71	0.639
9.5	0.6	0.3	0.3	0.25	0.10795	0.0762	0.71	0.730
9.5	0.9	0.3	0.3	0.25	0.10795	0.0762	0.71	0.819
9.5	1.2	0.3	0.3	0.25	0.10795	0.0762	0.71	0.905
9.5	1.5	0.3	0.3	0.25	0.10795	0.0762	0.71	0.990
9.5	0.3	0.3	0.3	0.5	0.10795	0.0762	0.71	0.534
9.5	0.6	0.3	0.3	0.5	0.10795	0.0762	0.71	0.611
9.5	0.9	0.3	0.3	0.5	0.10795	0.0762	0.71	0.686
9.5	1.2	0.3	0.3	0.5	0.10795	0.0762	0.71	0.760
9.5	1.5	0.3	0.3	0.5	0.10795	0.0762	0.71	0.832
9.5	0.3	0.3	0.3	0.75	0.10795	0.0762	0.71	0.457
9.5	0.6	0.3	0.3	0.75	0.10795	0.0762	0.71	0.523
9.5	0.9	0.3	0.3	0.75	0.10795	0.0762	0.71	0.587
9.5	1.2	0.3	0.3	0.75	0.10795	0.0762	0.71	0.650
9.5	1.5	0.3	0.3	0.75	0.10795	0.0762	0.71	0.712
9.5	0.3	0.3	0.3	0.99	0.10795	0.0762	0.71	0.400
9.5	0.6	0.3	0.3	0.99	0.10795	0.0762	0.71	0.458
9.5	0.9	0.3	0.3	0.99	0.10795	0.0762	0.71	0.514
9.5	1.2	0.3	0.3	0.99	0.10795	0.0762	0.71	0.570
9.5	1.5	0.3	0.3	0.99	0.10795	0.0762	0.71	0.624

B. Comparative Study Input and Output Dataset

A thorough comparative study between the proposed numerical model with experiments and well-known models taken from literature was conducted and presented in Chapter 7. Additionally, another comparison was made among the proposed numerical model, developed surrogate models and an experimental work and presented in Chapter 8. In this appendix, input and output dataset for the comparative studies are presented through following tables.

First, the comparison dataset with experimental study conducted in Tang et al. (2016) is presented. In this comparison, surge and swab pressure gradients were compared for three different YPL fluids using the input parameters listed in Table 7.4 and average absolute percent errors (AAPE) are calculated using equations Eq. 7-1 and Eq. 7-2. Tables from Table B-1 to Table B-3 show the input and output dataset for the comparison made with Fluid-1, Fluid-2 and Fluid-3, respectively.

Table B.1 Pressure Gradients and AAPEs for Comparative Study Shown in Figure 7.9, HB-1 Fluid

$V_p, m/s$	$\frac{dp}{dl}, kPa/m$ Numerical Model	$\frac{dp}{dl}, kPa/m$ Expr. in Tang	AAPE-Expr. in Tang
0.03	3.259	3.506	7.072
0.06	3.679	3.922	6.210
0.09	3.978	4.234	6.032
0.12	4.220	4.468	5.541
0.15	4.426	4.701	5.854
0.18	4.608	4.909	6.139
0.21	4.771	5.117	6.756
0.24	4.921	5.247	6.212

Table B.2 Pressure Gradients and AAPEs for Comparative Study Shown in Figure 7.9, HB-2 Fluid

$V_p, m/s$	$\frac{dp}{dl}, kPa/m$ Numerical Model	$\frac{dp}{dl}, kPa/m$ Expr. in Tang	AAPE-Expr. in Tang
0.03	2.239	2.362	5.216
0.06	2.539	2.693	5.701
0.09	2.749	2.913	5.649
0.12	2.915	3.071	5.072
0.15	3.055	3.260	6.281
0.18	3.177	3.386	6.156
0.21	3.287	3.496	5.989
0.24	3.386	3.559	4.865

Table B.3 Pressure Gradients and AAPEs for Comparative Study Shown in Figure 7.9, HB-3 Fluid

$V_p, m/s$	$\frac{dp}{dl}, kPa/m$ Numerical Model	$\frac{dp}{dl}, kPa/m$ Expr. in Tang	AAPE-Expr. in Tang
0.03	1.177	1.283	8.265
0.06	1.367	1.465	6.681
0.09	1.502	1.596	5.894
0.12	1.610	1.687	4.533
0.15	1.703	1.808	5.823
0.18	1.784	1.879	5.045
0.21	1.857	2.010	7.617
0.24	1.924	2.071	7.099

Other comparative study consists of comparison with models taken from literature. Figure 7.10 shows the pressure gradient comparison for varying tripping velocities with different eccentricity values using the input shown in Table 7.5. In this appendix

Table B.4, Table B.5 and Table B.6 list the input and output dataset for this particular comparison for the eccentricities of $\varepsilon = 0.2$, $\varepsilon = 0.4$ and $\varepsilon = 0.6$, respectively.

Table B.4 Pressure Gradients and AAPEs for Comparative Study Shown in Figure 7.10, ε = 0.2

$V_p, m/s$	$\frac{dp}{dl}, kPa/m$ Numerical Model	$\frac{dp}{dl}, kPa/m$ Model in Belimane	AAPE-Model in Belimane
0.1	1.231	0.818	50.456
0.3	1.945	1.818	6.959
0.5	2.508	2.455	2.166
0.7	3.003	2.974	0.984
0.9	3.457	3.442	0.443
1.1	3.880	3.857	0.603
1.3	4.281	4.260	0.501

Table B.5 Pressure Gradients and AAPEs for Comparative Study Shown in Figure 7.10, ε = 0.4

$V_p, m/s$	$\frac{dp}{dl}, kPa/m$ Numerical Model	$\frac{dp}{dl}, kPa/m$ Model in Belimane	AAPE-Model in Belimane
0.1	1.130	0.712	58.665
0.3	1.810	1.584	14.238
0.5	2.350	2.156	9.006
0.7	2.820	2.610	8.030
0.9	3.250	3.013	7.866
1.1	3.650	3.377	8.096
1.3	4.030	3.727	8.122

Table B.6 Pressure Gradients and AAPEs for Comparative Study Shown in Figure 7.10, ε = 0.6

$V_p, m/s$	$\frac{dp}{dl}, kPa/m$ Numerical Model	$\frac{dp}{dl}, kPa/m$ Model in Belimane	AAPE-Model in Belimane
0.1	0.981	0.584	67.860
0.3	1.593	1.338	19.088
0.5	2.076	1.818	14.186
0.7	2.501	2.195	13.955
0.9	2.890	2.545	13.536
1.1	3.253	2.857	13.862
1.3	3.597	3.156	13.970

Next comparative study includes three different models and one experimental work with the inputs listed in Table 7.6. Figure 7.11, Figure 7.12 and Figure 7.13 shows the pressure gradient comparison for varying tripping speeds in a highly eccentric

annulus, $\varepsilon = 0.9$ for three different YPL fluids, namely HB-1, HB-2, and HB-3. Tables from Table B.7 to Table B.9 lists the numerical values of pressure gradient results.

Table B.7 Pressure Gradients for Comparative Study Shown in Figure 7.11, HB-1 Fluid

$V_p, m/s$	$\frac{dp}{dl}, kPa/m$ Experiment	$\frac{dp}{dl}, kPa/m$ Model in Belimane	$\frac{dp}{dl}, kPa/m$ Model in Haciislamoglu	$\frac{dp}{dl}, kPa/m$ Model in Tang	$\frac{dp}{dl}, kPa/m$ Numerical Model
0.0304	3.513	2.529	2.568	2.828	3.068
0.0609	3.924	3.617	3.397	3.743	3.485
0.0914	4.202	4.170	3.816	4.210	3.780
0.1219	4.432	4.565	4.093	4.518	4.018
0.1523	4.638	4.835	4.315	4.756	4.220
0.1828	4.876	5.057	4.506	4.970	4.397
0.2133	5.027	5.247	4.665	5.153	4.558
0.2438	5.202	5.407	4.816	5.312	4.703

Table B.8 Pressure Gradients for Comparative Study Shown in Figure 7.12, HB-2 Fluid

$V_p, m/s$	$\frac{dp}{dl}, kPa/m$ Experiment	$\frac{dp}{dl}, kPa/m$ Model in Belimane	$\frac{dp}{dl}, kPa/m$ Model in Haciislamoglu	$\frac{dp}{dl}, kPa/m$ Model in Tang	$\frac{dp}{dl}, kPa/m$ Numerical Model
0.0304	2.354	2.003	2.018	2.239	2.138
0.0609	2.670	2.603	2.473	2.757	2.427
0.0914	2.880	2.909	2.712	3.010	2.629
0.1219	3.052	3.119	2.888	3.206	2.790
0.1523	3.223	3.276	3.022	3.363	2.926
0.1828	3.337	3.410	3.145	3.496	3.045
0.2133	3.451	3.528	3.254	3.615	3.152
0.2438	3.493	3.628	3.349	3.724	3.248

Table B.9 Pressure Gradients for Comparative Study Shown in Figure 7.13, HB-3 Fluid

$V_p, m/s$	$\frac{dp}{dl}, kPa/m$ Experiment	$\frac{dp}{dl}, kPa/m$ Model in Belimane	$\frac{dp}{dl}, kPa/m$ Model in Haciislamoglu	$\frac{dp}{dl}, kPa/m$ Model in Tang	$\frac{dp}{dl}, kPa/m$ Numerical Model
0.0304	1.266	1.272	1.148	1.268	1.120
0.0609	1.449	1.512	1.338	1.476	1.297
0.0914	1.577	1.651	1.468	1.617	1.425
0.1219	1.669	1.751	1.565	1.726	1.535
0.1523	1.794	1.836	1.647	1.816	1.623
0.1828	1.848	1.905	1.717	1.895	1.703
0.2133	1.986	1.965	1.783	1.967	1.773
0.2438	2.044	2.024	1.841	2.033	1.839

The performance of surrogate models was further validated via a comparative study in Chapter 8; where results from ANN, RF, experimental study and proposed numerical model were compared and presented in Figure 8.11. The errors for this analysis were listed in Table 8.6. In this appendix, resultant pressure gradients are in a highly eccentric annulus of $\varepsilon = 0.9$ for three YPL fluids, namely HB-1, HB-2 and HB-3 are given in Table B.10, Table B.11 and Table B.12, respectively.

Table B.10 Pressure Gradients for Comparative Study Shown in Figure 8.6, HB-1 Fluid

$V_p, m/s$	$\frac{dp}{dl}, kPa/m$ Experiment	$\frac{dp}{dl}, kPa/m$ Result from ANN	$\frac{dp}{dl}, kPa/m$ Result from RF	$\frac{dp}{dl}, kPa/m$ Numerical Model
0.0304	3.513	2.870	3.505	3.068
0.0609	3.924	3.120	3.686	3.485
0.0914	4.202	3.367	3.806	3.780
0.1219	4.432	3.613	4.142	4.018
0.1523	4.638	3.857	4.172	4.220
0.1828	4.876	4.099	4.286	4.397
0.2133	5.027	4.340	4.309	4.558
0.2438	5.202	4.579	4.315	4.703

Table B.11 Pressure Gradients for Comparative Study Shown in Figure 8.6, HB-2 Fluid

$V_p, m/s$	$\frac{dp}{dl}, kPa/m$ Experiment	$\frac{dp}{dl}, kPa/m$ Result from ANN	$\frac{dp}{dl}, kPa/m$ Result from RF	$\frac{dp}{dl}, kPa/m$ Numerical Model
0.0304	2.354	2.160	2.332	2.138
0.0609	2.670	2.274	2.450	2.427
0.0914	2.880	2.387	2.645	2.629
0.1219	3.052	2.500	2.813	2.790
0.1523	3.223	2.611	2.944	2.926
0.1828	3.337	2.722	3.056	3.045
0.2133	3.451	2.831	3.076	3.152
0.2438	3.493	2.940	3.085	3.248

Table B.12 Pressure Gradients for Comparative Study Shown in Figure 8.6, HB-3 Fluid

$V_p, m/s$	$\frac{dp}{dl}, kPa/m$ Experiment	$\frac{dp}{dl}, kPa/m$ Result from ANN	$\frac{dp}{dl}, kPa/m$ Result from RF	$\frac{dp}{dl}, kPa/m$ Numerical Model
0.0304	1.266	1.501	1.287	1.120
0.0609	1.449	1.532	1.313	1.297
0.0914	1.577	1.563	1.377	1.425
0.1219	1.669	1.594	1.595	1.535
0.1523	1.794	1.625	1.644	1.623
0.1828	1.848	1.656	1.680	1.703
0.2133	1.986	1.686	1.684	1.773
0.2438	2.044	1.716	1.690	1.839

C. MATLAB Code for Implicit Numerical Model

In the spirit of transparency, reproducibility, and fostering collaboration within the academic community, this appendix provides access to the MATLAB codes developed for the implementation of the implicit numerical model presented in Chapter 4 of this thesis. These codes serve as a valuable resource for researchers interested in replicating the analysis, verifying the results, or building upon this work in related studies.

MATLAB R2018b is used to obtain the surge and swab pressure gradient output in eccentric annulus. It is done using three different array of codes. Main code includes the input values such as eccentricity, fluid properties, wellbore geometry and tripping speed, and serves as the caller of the functions. Two functional code are also presented. First one is related to the geometric transformation from concentric to eccentric annulus by the approach taken by Luo and Peden (1990). Second function corresponds to the implicit numerical model to solve for surge and swab pressures of YPL fluids in concentric annulus. It includes preparing matrices considering the discretized equation, Eq. 4-8, applying boundary conditions, matrix division to obtain velocity profile, updateing shear rate and viscosity profile, then an iterative approach to obtain final velocity profile and surge and swab pressure gradient.

Caller code, geometric transformation function, and implicit model function are given below, respectively:

```
Ro = 0.2159;
Ri = 0.1016;
Tau0 = 8;
Mu = 0.3;
n = 0.7;
density = 1000;
Vp = 0.5;
epsilon=0.8;
E=epsilon*(Ro-Ri);
N=300;
K=Mu;
tol = 0.01;
```

```
dPdl1=100;
dPdl2=4000;
initialInterval = [dPdl1 dPdl2];
crossSecAreaOfInnerPipe=pi*Ri^2;
volumeChangeOfTheMovingPipeAtBottom=crossSecAreaOfInnerPipe*Vp;
crossSecAreaOfAnnulus = pi*(Ro^2-Ri^2);
[dPdl1_final, b, exitflag, output] = fzero(@(dPdl1)
abs(mean(mean(FN_LuoPeden(Ro,Ri,tol,Mu,dPdl1,N,Tau0,K,n,density,Vp,E))))...
*crossSecAreaOfAnnulus-volumeChangeOfTheMovingPipeAtBottom,
initialInterval)
[Total_Vprofile,X,Y,Total_r] =
FN_LuoPeden(Ro,Ri,tol,Mu,dPdl1_final,N,Tau0,K,n,density,Vp,E);

function
[Total_Vprofile,X,Y,Total_r]=FN_LuoPeden(Ro,Ri,tol,Mu,dPdl,N,Tau0,K,n,densi
ty,Vp,E)
number_adjustment=0;
j=0;
Roinitial=Ro;
for i=1:N+1
Ro (i)= Roinitial;
teta(i)=2*(i-1)*pi()/N;
Ro(i)=E*cos(teta(i))+sqrt(Ro(i)^2-(E*sin(teta(i)))^2);
Ro(i)=real(Ro(i));
j=j+1;
[u2,r]=FN_SwabSurge(Ro(i),Ri,tol,Mu,dPdl,N,Tau0,K,n,density,Vp);
X(i,:)=r*cos(teta(i));
Y(i,:)=r*sin(teta(i));
X=real(X);
Y=real(Y);
Total_Vprofile(i,:)=u2;
Total_Vprofile=real(Total_Vprofile);
if j==1
number_adjustment=numel(u2);
end
Total_r(i,:)=r;
OuterRadius(i)=Ro(i);
end

function
[u2,r,Mu2,Tau]=FN_SwabSurge(Ro,Ri,tol,Mu,dPdl,N,Tau0,K,n,density,Vp)
N=100;
dr = (Ro - Ri)/(N);
rH=Ro-Ri;
K=Mu;
```

```
for i=1:N+1
r(i) = Ri + dr*(i-1);
u1(i) = Ri + dr*(i-1);
Mu1(i)=0.1;
end
for i=1:(N/2+1)
u1(i) = Ri + dr*(i-1);
end
for i=(N/2+1):(N+1)
u1(i) = Ro- dr*(i-1);
end
u1=u1';
change = 1;
iter=0;
shear_rate=zeros(N+1,1);
for i=1:N
if i==1
shear_rate(1)=(u1(2)-u1(1))/(dr);
elseif i==N+1
shear_rate(N+1)=(u1(N+1)-u1(N))/(dr);
else
shear_rate(i)=(u1(i+1)-u1(i-1))/(2*dr);
end
end
while abs(change)>tol
sum=0;
iter=iter+1;
for i=1:N+1
al(i) = Mu1(i);
end
f=zeros(N+1,1);
for i=1:N+1
f(i) = 0;
for j=1:N+1
aa(i,j) = 0.;
end
end
for i=2:N
aa(i,i) = -(al(i+1)+2*al(i)+al(i-1));
aa(i,i-1) = al(i)+al(i-1)- dr*al(i)/r(i);
aa(i,i+1) = al(i)+al(i+1)+ dr*al(i)/r(i);
f(i) = 2*dr*dr*dPdl;
end
f(1) = Vp;
f(N+1) = 0;
```

```
aa(1,1) = 1;
aa(1,2) = 0;
aa(N+1,N) = 0;
aa(N+1,N+1) = 1;
u2 = aa\f;
shear_rate=zeros(N+1,1);
Mu2=zeros(N+1,1);
for i=1:N+1
if i==1
shear_rate(1)=((u2(2)-u2(1))/(dr));
elseif i==N+1
shear_rate(N+1)=(u2(N+1)-u2(N))/(dr);
else
shear_rate(i)=(u2(i+1)-u2(i-1))/(2*dr);
end
end
shear_rate=abs(shear_rate);
for i=1:N+1
Mu2(i) = Tau0/shear_rate(i) + K * shear_rate(i).^(n - 1);
Tau(i)=Mu2(i)*shear_rate(i);
if  Mu2(i)>1e5;
Mu2(i)=1e5;
end
end
for i=1:N+1
sum = sum + abs(Mu1(i) - Mu2(i));
Mu1(i) = Mu2(i);
end
change = sum;
end
end
```

CURRICULUM VITAE

Surname, Name: Erge, Öner

EDUCATION

Degree	Institution	Year of Graduation
MS	METU Petroleum and Natural Gas Engineering	2016
BS	METU Petroleum and Natural Gas Engineering	2012
High School	Yıldırım Beyazıt Anadolu High School, Ankara	2007

WORK EXPERIENCE

Year	Company	Position
2023-Present	GEOS Drilling Fluids Co.	Drilling Fluids Manager
2017-2023	GEOS Drilling Fluids Co.	Project Engineer
2014-2017	GEOS Drilling Fluids Co.	Drilling Fluids Engineer
2012-2014	Karkim Drilling Fluids Co.	Drilling Fluids Engineer

FOREIGN LANGUAGES

Advanced English

PUBLICATIONS

1. Oner Erge. Kudret Sakaoglu. Ahmet Sonmez. Gokhan Bagatir. H. Ali Dogan. Ahmet Ay. Hakki Gucuyener. “Overview and Design Principles of Drilling Fluid Systems for Geothermal Wells in Turkey” Geothermics. Volume 88. 2020. doi.org/10.1016/j.geothermics.2020.101897

HOBBIES

Music, Sports, Travelling